Global climate and Indonesian Throughflow during the Middle Miocene Climate Transition: a modeling approach

Dissertation

zur Erlangung des Doktorgrades der Naturwissenschaften

im Fachbereich Geowissenschaften

der Universität Bremen

vorgelegt von

Amanda Frigola Boix

Bremen, April 2019

Universität Bremen

Gutachter

Prof. Dr. Michael Schulz

“Am grauen Strand, am grauen Meer,
und seitab liegt die Stadt;
der Nebel drückt die Dächer schwer,
und durch die Stille braust das Meer
eintönig um die Stadt.

Es rauscht kein Wald, es schlägt im Mai
kein Vogel ohn' Unterlaß;
die Wandergans mit hartem Schrei
nur fliegt in Herbstesnacht vorbei,
am Strande weht das Gras.

Doch hängt mein ganzes Herz an dir,
du graue Stadt am Meer;
der Jugend Zauber für und für
ruht lächelnd doch auf dir, auf dir,
du graue Stadt am Meer.”

Theodor Storm

To Martín and Montserrat

Contents

Abstract

The current study focuses on the Middle Miocene Climate Transition (MMCT), a main global cooling step during the Cenozoic (66–0 Ma). This transition, likely triggered by changes in the Earth's orbital configuration and a decrease in atmospheric CO_2 concentration, entailed major expansion of the Antarctic ice sheet, cooling of the surface and deep ocean, and global eustatic sea level fall during the interval ~15–13 Ma.

A central aim of this study is to assess, by means of the global coupled model Community Climate System Model version 3 (CCSM3), the ocean response to atmospheric CO_2 dropdown and Antarctic ice sheet expansion during the MMCT. In particular, it is investigated whether the combined effects of the CO_2 decrease and Antarctic ice sheet expansion could explain the cooling of surface and deep waters across the MMCT inferred from proxy data, the separate effects of these two forcings on surface and deep water temperatures, and the mechanisms these forcings were triggering that explain their modeled effects on ocean temperatures.

Ocean gateways are relatively narrow channels of water separating two main ocean basins. Changes in the bathymetry of ocean gateways alter the water properties of the basins they connect and this can have regional to global scale climate effects. An example of ocean gateway is the Indonesian gateway, the tropical passage connecting the Pacific and Indian oceans, which has a significant influence on the climatic states of those oceans. The origin of the West Pacific Warm Pool, for example, the most extensive warm surface water mass on Earth, has been suggested to be linked to narrowing of the Indonesian gateway.

A further aim of this study is that of modeling the characteristics of the Indonesian Throughflow during the MMCT by means of CCSM3, providing estimates of volume transport, analyzing the vertical structure of the waterflow, the direction of waterpaths, the relative contributions of North and South Pacific water to the Indonesian Throughflow, the control mechanisms of its seasonal

variability, and examining whether a similar structure to the present-day West Pacific Warm Pool existed during the MMCT in the Indonesian Throughflow area.

The model boundary conditions employed in our experiments include Middle Miocene global vegetation, topography, and bathymetry – comprising a geographic reconstruction of Southeast Asia for 15 Ma – as well as Antarctic ice sheet configurations, sea levels, and atmospheric CO_2 concentrations characterizing the periods before (Middle Miocene Climatic Optimum) and after the transition (Middle Miocene Glaciation).

In the CCSM3 experiments, global mean sea surface temperatures decrease by 1.6 °C across the transition due to an increase in the heat flux from the ocean to the atmosphere linked to the CO_2 dropdown. The Antarctic ice sheet expansion, instead, causes slight warming of the ocean surface. This warming is associated with a decrease in the upwelling longwave flux at the top of the atmosphere over Antarctica as a consequence of the increased Antarctic topography. Our sea surface cooling estimates for the Southern Ocean are in good agreement with local proxy evidence, suggesting that the combined effects of CO_2 decrease and Antarctic ice sheet expansion are sufficient to explain cooling of surface waters across the MMCT.

Ocean temperatures decrease between 1.5–2 °C at depth in most regions, explaining a larger part of the cooling of deep waters inferred from Mg/Ca studies (2–3 °C). The decrease in CO_2 cools down the ocean at all depths, while the Antarctic ice sheet expansion causes cooling below ~ 1400 m depth and warming above ~ 1400 m depth (and at deeper levels in the Arctic).

In the Southern Ocean, cooling at depth is triggered by both the CO_2 and Antarctic ice sheet forcings. These two forcings induce cooling of waters in the upper ocean, which is transmitted to the ocean bottom through water convection and spread to the north as Antarctic Bottom Water. Although water convection in the Southern Ocean occurs already during the Middle Miocene Climatic Optimum, the potential density field suggests an intensification in Antarctic Bottom Water formation across the MMCT caused by increases in salinity (induced by sea ice formation and by

changes in the precipitation/evaporation balance) around the Antarctic coast linked to the CO_2 forcing.

In the North Atlantic, cooling at depth is related to the CO_2 decrease. The CO_2 dropdown induces upper ocean cooling which is transmitted to the deep ocean through deep water convection. Deep water convection in the North Atlantic occurs already during the Middle Miocene Climatic Optimum and is caused by the high salinities and the relatively cold upper ocean temperatures in that area. However, it intensifies across the transition due to a decrease in upper ocean temperatures. A volume transport of -13.3 Sverdrups across the Indonesian gateway from the Pacific to the Indian Oceans during the Middle Miocene Climatic Optimum is simulated, with no evidence of any significant eastward flow. Although the total Indonesian Throughflow volume transport remains practically constant across the transition, changes in the water-transport pathways are simulated related to global eustatic sea level fall affecting the shallowest paths and to a weakening of the South Pacific Gyre. During the MMCT, the Indonesian Throughflow has a stronger South Pacific component than during the pre-industrial. The model results suggest the existence of a proto West Pacific Warm Pool during the MMCT, with a similar extension to that of pre-industrial. The sub-annual variability of the Indonesian Throughflow during the MMCT is strongly controlled by northwest and southeast seasonal winds, as during the pre-industrial.

The study of the MMCT provides a potential reversed analogy of present-day climate change in terms of atmospheric CO_2 concentration, since one of the main triggers of the MMCT was a decrease in atmospheric CO_2 from values similar to present-day to values slightly lower than those during the pre-industrial. In this sense, the study of the MMCT can improve our understanding of the potential consequences of present-day climate change.

Zusammenfassung

Die vorliegende Studie behandelt den Kälteumschwung des Mittleren Miozäns (Middle Miocene Climate Transition; MMCT), eine weltweite Temperatursenkung während des Känozoikums (66-0 Ma). Dieser Umschwung, der wahrscheinlich durch Änderungen der orbitalen Konfiguration der Erde und Verminderung der atmosphärischen CO_2-Konzentration verursacht wurde, ging mit einer deutlichen Ausweitung des antarktischen Eisschildes, der Abkühlung der Oberflächen- und Tiefenwässer des Ozeans, und einer globalen eustatischen Absenkung des Meeresspiegels im Intervall ~15–13 Ma einher.

Ein Hauptziel dieser Studie ist die Bewertung der Reaktion des Ozeans auf die atmosphärische CO_2-Konzentrationsminderung und die Ausweitung des antarktischen Eisschildes während des MMCT anhand des globalen Klimamodells Community Climate System Model Version 3 (CCSM3). Dabei wird ein Hauptaugenmerk daraufgelegt, ob die Abkühlung der Oberfläche und des tiefen Ozeans während des MMCT in den Proxydaten durch die zusammenhängenden Effekte der CO_2-Senkung und der Ausweitung der antarktischen Eisschicht erklärbar sind. Ebenso wird untersucht, wie sich die verschiedenen Effekte dieser beiden Auslösekräfte auf die Oberflächen- und Tiefentemperatur des Ozeans auswirken und welche Mechanismen diese Kräfte ausgelöst haben, die ihre modellierten Effekte auf die Meerestemperatur erklären.

Meeresengen sind relativ enge Wasserkanäle, die zwei Hauptozeanbecken voneinander trennen. Veränderungen in der Bathymetrie der Meeresengen verändern die Wassereigenschaften der Becken, die sie verbinden. Dies kann Auswirkungen auf das Klima von regionaler bis globaler Ebene haben. Ein Beispiel ist die Indonesische Meeresenge, die tropische Passage, die den Pazifik mit dem Indischen Ozean verbindet und die einen bedeutenden Einfluss auf den klimatischen Status dieser Ozeane hat. Zum Beispiel könnte die Entstehung des Westpazifischen Wärmepools, die größte warme Oberflächenwassermasse der Erde, auf eine Verengung der Indonesischen

Meeresenge rückführbar sein.

Ein weiteres Ziel dieser Studie ist die Modellierung der Charakteristika des Indonesischen Durchstroms während des MMCT anhand von CCSM3. Dabei werden Transportvolumen geschätzt, und die vertikale Struktur des Wasserflusses, die Richtung der Wasserwege, die relativen Anteile des Wassers aus dem Nord- und Südpazifik am Indonesischen Durchstrom und die Kontrollmechanismen ihrer jahreszeitenbedingten Variabilität analysiert. Außerdem wird untersucht, ob eine ähnliche Struktur zum heutigen Westpazifischen Wärmepool während des MMCT im Gebiet des Indonesischen Durchstroms existierte.

Die Randbedingungen des Modells, die in unserem Experiment verwendet wurden, beinhalten die globale Vegetation, Topographie und Bathymetrie im Mittelmiozän - inklusive einer geographischen Rekonstruktion von Südostasien für 15 Ma - sowie antarktische Eisschildkonfigurationen, Meeresspiegel und atmosphärischen CO_2-Konzentrationen, die die Perioden vor (Mittelmiozänes Klimaoptimum; MMCO) und nach dem Umschwung (Mittelmiozänes Glazial; MMG) charakterisieren.

In den CCSM3-Experimenten verringerten sich während des Umschwunges die globalen, durchschnittlichen Meeresoberflächentemperaturen um 1,6°C aufgrund eines Anstiegs des Wärmeflusses vom Ozean zur Atmosphäre, der mit der Verringerung der CO_2-Konzentration zusammenhängt. Die Ausweitung des antarktischen Eisschildes verursachte hingegen eine leichte Erwärmung der Meeresoberfläche. Diese Erwärmung wird mit einer Verminderung der langwelligen Ausstrahlung in den oberen Schichten der Atmosphäre über der Antarktis assoziiert, als Konsequenz der vergrößerten antarktischen Topographie. Unsere Schätzungen für die Meeresoberflächentemperatursenkung des Südlichen Ozeans stimmen mit den lokalen Proxydaten überein und weisen darauf hin, dass die kombinierten Effekte der Verringerung der CO_2-Konzentration und die Ausweitung des antarktischen Eisschildes ausreichen, um die Abkühlung des Oberflächenwassers während des MMCT zu erklären.

Die Temperatur der Ozeane verringert sich zwischen 1,5-2,0°C in der Tiefe in den meisten Regionen und erklärt zum großen Teil die Abkühlung der Tiefengewässer, die in Mg/Ca-Studien angenommen wird (2-3°C). Die Verringerung der CO_2-Konzentration kühlt Ozeane in allen Tiefen ab, während die Ausweitung des antarktischen Eisschildes eine Abkühlung unter ~ 1400m Tiefe und eine Erwärmung über ~ 1400m Tiefe (und in tieferen Ebenen in der Arktis) verursacht.

Im Südlichen Ozean wird die Temperatursenkung in der Tiefe durch die beiden Kräfte des CO_2 und des antarktischen Eisschildes ausgelöst. Diese beiden Kräfte induzieren die Wasserabkühlung im oberen Ozean, welche durch Wasserkonvektion bis an den Meeresboden vordringt und sich in den Norden als Antarktisches Bodenwasser ausbreitet. Obwohl die Wasserkonvektion im Südlichen Ozean bereits während des Mittelmiozänen Klimaoptimums stattfindet, weist der potentielle Dichtebereich auf eine Intensivierung in der Formierung des Antarktischen Bodenwassers während des MMCT hin, die durch Erhöhungen der Salinität (induziert durch Meereseisformationen und Veränderungen der Niederschlag/Verdunstungs-Balance) an der antarktischen Küste in Verbindung mit CO_2-Kräften hervorgerufen wird.

Im Nordatlantik hängt die Abkühlung des Tiefenwassers mit der Verringerung der CO_2-Konzentration zusammen. Der CO_2-Abfall erzeugt die Abkühlung des oberen Ozeans, welche durch Tiefenwasserkonvektion an den tiefen Ozean weitergegeben wird. Tiefenwasserkonvektion findet im Nordatlantik bereits während des Mittelmiozänen Klimaoptimums statt und wird in diesem Gebiet durch hohe Salinität und relativ kalte obere Ozeantemperaturen verursacht. Sie verstärkt sich jedoch während des Umschwungs aufgrund einer Verringerung der oberen Ozeantemperaturen.

In dieser Studie wird ein Volumentransport von -13.3 Sverdrup vom Pazifik zum Indischen Ozean durch den Indonesischen gateway während des Mittelmiozänen Klimaoptimums simuliert, ohne dass eine signifikante ostwärts gerichtete Strömung nachgewiesen werden kann. Obwohl die gesamten Volumenströme des Indonesischen Durchstroms während des Übergangs praktisch konstant bleiben, werden Änderungen in den Wassertransportwegen simuliert, relativ zum globalen

eustatischen Meeresspiegelabfall, der die flachsten Ebenen betrifft, und relativ zu einer Abschwächung des Südpazifikwirbels. Während des MMCT hat der Indonesische Durchstrom eine stärkere Südpazifikkomponente als in der vorindustriellen. Die Modellergebnisse suggerieren die Existenz eines proto Westpazifischen Wärmepools während des MMCT mit einem ähnlichen Ausmaß wie in der vorindustriellen. Die unterjährige Variabilität des Indonesischen Durchstroms während des MMCT wird stark durch jahreszeitenbedingte nordwestliche und südöstliche Winde kontrolliert, so wie auch in der vorindustriellen Zeit.

Die Untersuchung des MMCT bietet eine potenziell umgekehrte Analogie zum heutigen Klimawandel hinsichtlich der atmosphärischen CO_2-Konzentration, da eine der Hauptursachen des MMCT die Verringerung der atmosphärischen CO_2-Konzentration war, von Werten, die den heutigen ähneln zu Werten leicht unterhalb denen aus der vorindustriellen Zeit. In diesem Sinne kann die Untersuchung des MMCT unser Verständnis der potenziellen Konsequenzen des heutigen Klimawandels verbessern.

List of figures

List of tables

1. Introduction

1.1. The Middle Miocene Climate Transition within a context of Cenozoic history

A global cooling trend characterizes the history of the Cenozoic era (66–0 Ma) (Flower and Kennett, 1994; Zachos et al., 2001) (Fig. 1.1.). The first major cooling step of the Cenozoic took place at the Eocene–Oligocene boundary (~ 34 Ma) and entailed the expansion of stable continental ice sheets on Antarctica and the onset of a global Meridional Overturning Circulation (MOC). Continental-scale ice sheets on Antarctica endured until ~ 27 Ma in the Late Oligocene, when they switched back to a partial/ephemeral regime, but global climate stayed colder than at the Early and early Middle Eocene for the remaining of the Cenozoic. Warming was highest at ~ 17–15 Ma, at the so called Middle Miocene Climatic Optimum (MMCO), but a second rapid major cooling phase came next, involving expansion of continental Antarctic ice sheets, cooling of the surface and deep ocean, and important global eustatic sea level fall at ~15–13 Ma (Holbourn et al., 2005; John et al., 2011; Lear et al., 2010, 2000; Shevenell et al., 2008, 2004) (Fig. 1.1.). This cooling transition is known as Middle Miocene Climate Transition (MMCT) and is the focus of this thesis. The cooling trend initiated during the MMCT continued at a lower scale during the Late Miocene and Early Pliocene, with some fluctuations, and at ~ 3.2 Ma, in the Late Pliocene, the last major cooling step took place, which supposed the onset of Northern Hemisphere ice sheets (Flower and Kennett, 1994; Zachos et al., 2001).

One of the suggested main triggers for the MMCT is a decrease in atmospheric CO_2 concentrations (see sect. 1.3.) from values comparable to present-day levels to slightly lower than pre-industrial levels. The study of the MMCT provides thus an interesting potential "reversed" analogy of present-day global climate change. In particular, it can bring knowledge on how global temperatures and ocean circulation might respond to changes in greenhouse gases concentrations in the range of

those experienced since the pre-industrial era. Besides, the study of the Middle Miocene, as example of warm period (Pound et al., 2012; Zachos et al. 2001; Flower and Kennett, 1994), can help us characterizing the dynamics of the ocean and the atmosphere under warm conditions.

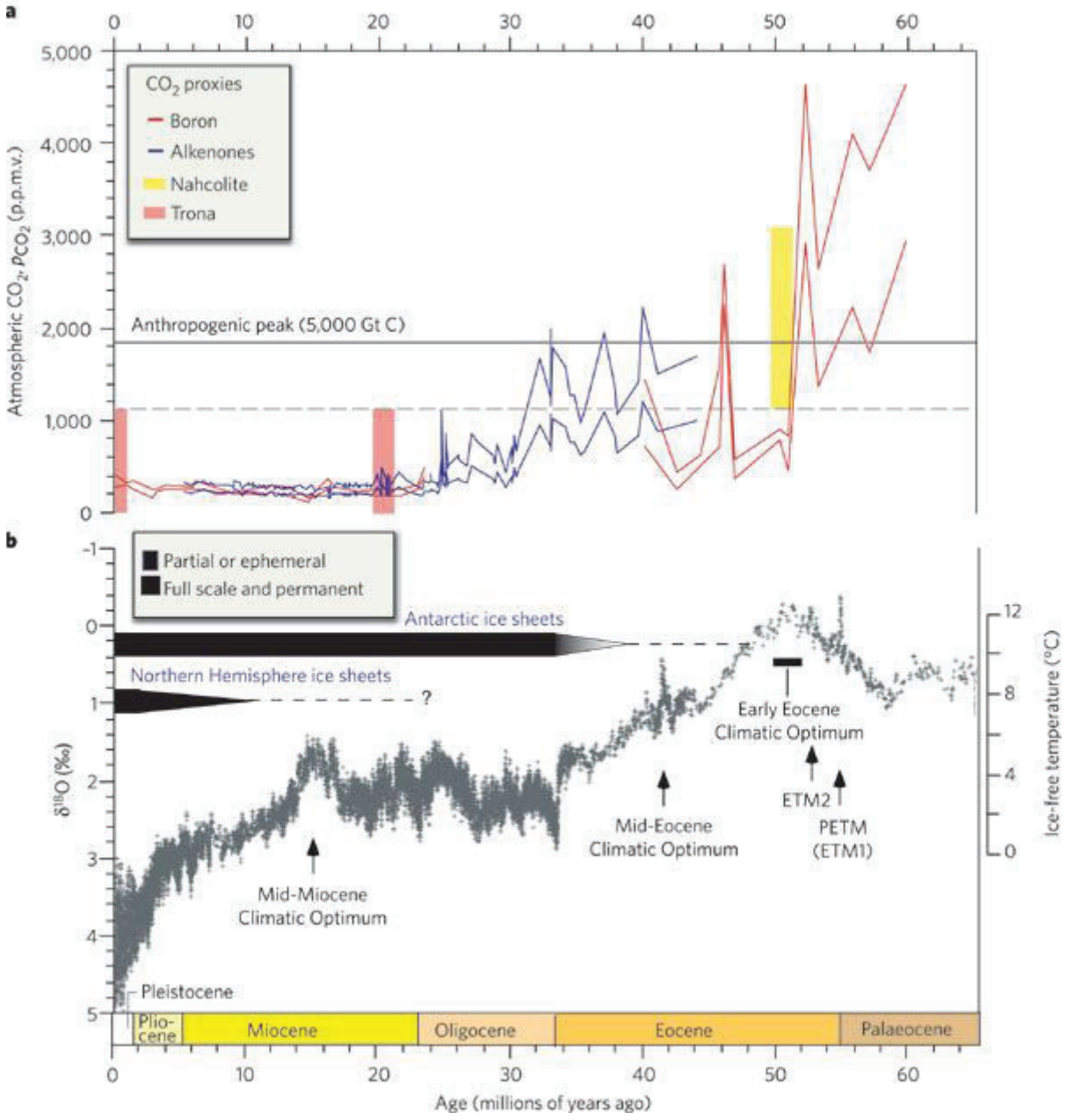

Figure 1.1. *Cenozoic (a) atmospheric CO_2 and (b) deep benthic foraminiferal $\delta^{18}O$ (a proxy for deep water temperature and global ice volume) curves. Extracted from Zachos et al. (2008).*

1.2. Evidence for climatic and oceanographic changes during the Middle Miocene Climate Transition

The major evidence for the MMCT is the increase of ~ 0.8–1.2 per mil in $\delta^{18}O$ shown in benthic foraminiferal records (e.g., Holbourn et al., 2005; Lear et al., 2010; Shevenell et al., 2008), with the main part in the $\delta^{18}O$ signal (65–85%) representing expansion of the Antarctic ice sheet (Lear et al., 2010, 2000; Shevenell et al., 2008). Further evidence for Antarctic ice sheet expansion at the MMCT is provided by the study by Levy et al. (2016), which analyzes data from the ANDRILL–2A (AND–2A) drill site, situated in the western Ross Sea, 30 km off the coast of Southern Victoria Land. Levy et al. (2016) interpreted the two unconformities found in the AND–2A record spanning the intervals 15.8 to 14.6 and 14.4 Ma to Late Miocene as local episodes of grounded ice advance eroding material at the site at different times within those two intervals. Additional evidence is derived from glacial deposits in Southern Victoria Land (East Antarctica), suggesting local ice sheet expansion at different time intervals between 13.85 and ~12.44 Ma (Lewis et al., 2007). Lewis et al. (2007) state that the ice expansion was preceded by significant atmospheric cooling, with glacial deposits showing evidence of a permanent shift from wet to cold at 13.94 Ma, suggesting that the ice expansion could be triggered by atmospheric cooling.

The Antarctic ice sheet expansion is also reflected in the sea level record. The studies by Kominz et al. (2008) and Haq et al. (1987), based on backstripping techniques, and John et al. (2011), combining backstripping techniques with benthic foraminiferal $\delta^{18}O$, indicate an important eustatic sea level fall across the MMCT.

Different studies based on Mg/Ca foraminiferal ratios report cooling of surface (Shevenell et al., 2004) and bottom waters (Lear et al., 2010, 2000; Shevenell et al., 2008; Billups and Schrag, 2002, 2003) across the MMCT within a range of ~0.5 to ~3 °C.

Atmospheric CO_2 dropdown across the transition has been reported in the literature (Foster et al.,

2012; Pearson and Palmer, 2000; Tripati et al., 2009; Retallack, 2009; Kürschner et al., 2008). Although the range of published estimates is rather wide, a decrease from ~ 400 to 200 ppmv is within the range of published estimates (sect. 2.2.3.)

1.3. Proposed causes for the Middle Miocene Climate Transition

The study by Holbourn et al. (2005), based on $\delta^{18}O$ and $\delta^{13}C$ data from ODP Sites 1146 and 1237, points at changes in the Earth's orbital configuration and atmospheric CO_2 concentrations as the main triggers of this climate transition. The AND–2A record indicates a correlation between CO_2 variations and local expansion of the Antarctic ice sheet at the MMCT (Levy et al., 2016). Langebroek et al. (2010), using an isotope enabled ice sheet–climate model forced with a decrease in CO_2 and varying time-dependent orbital parameters, simulate an increase in $\delta^{18}O$ of seawater in good agreement with published MMCT estimates. Gasson et al. (2016) show that, together, changes in atmospheric CO_2 within the range reported for the MMCT and variations in the Earth's orbital configuration, can explain the Antarctic ice sheet volume variability during the MMCT inferred from $\delta^{18}O$ and sea level studies. Holbourn et al. (2007) propose changes in atmospheric CO_2 and orbital configuration as the causes of this transition. Additionally, Holbourn et al. (2007) suggest that the CO_2 dropdown could be a consequence of the orbital variations since a clear eccentricity signal is identified in the different positive $\delta^{13}C$ excursions of the “Monterey Excursion“ spanning the interval between 16.9 to ~ 13.5 Ma.

An alternative suggested triggering mechanism for the MMCT is that closure of the Tethys gateway during the Middle Miocene would have reduced the flow of warm Tethys waters to the Southern Ocean and thus induced expansion of the Antarctic ice sheet (Flower and Kennett, 1994). Hamon et al. (2013), though, conclude that closure of the Tethys gateway alone does not explain the Middle Miocene glaciation. Similarly, Butzin et al. (2011) suggest that closure of the Tethys would not have

triggered the MMCT.

1.4. Outline of the thesis

In this thesis, the effects on surface and deep waters of the decrease in atmospheric CO_2 and the Antarctic ice sheet expansion across the MMCT are investigated by means of the global coupled General Circulation Model (GCM) Community Climate System Model version 3 (CCSM3) (sect. 2.1.). The current literature for MMCT global coupled GCM simulations is limited to one study (Knorr and Lohmann, 2014). This fact is partly due to the lack of adequate boundary conditions representing the MMCT. Knorr and Lohmann (2014) model the ocean response to Antarctic ice sheet growth and atmospheric CO_2 decrease across the transition.

Ocean gateways are relatively narrow channels of water separating two main ocean basins (e.g. the Indonesian gateway, Drake passage, or the former Central American and Tethys seaways). Ocean passages are subject to bathymetry transformations through time obeying plate tectonic changes (Kuhnt et al., 2004; Montes et al., 2012; Rögl, 1999; Eagles and Jokat, 2014). Opening and closure of ocean passages affects the pathways of ocean currents, altering the water properties (e.g. temperature and salinity) of the basins they are connecting and this might have regional to global scale climate effects (England et al., 2017; Cane and Molnar, 2001). Changes in the bathymetry of ocean gateways, for example, might affect heat and salinity transport from low to high latitudes and thus alter mechanisms of deep water formation at high latitudes (Flower and Kennett, 1994; Hamon et al., 2013; von der Heydt and Dijkstra, 2006).

In this thesis, we aim attention at the Indonesian gateway, the tropical gateway connecting the Pacific and the Indian oceans. The present-day Indonesian Throughflow (ITF) (the water flowing through the Indonesian gateway) cools and freshens the Indian Ocean (Gordon, 2005) and its subannual transport variability is mainly controlled by seasonal monsoon wind regimes and Kelvin

waves (Sprintall et al., 2009). The ITF has been proved to have a significant influence on the circulation and climatic states of the Indian and Pacific oceans both in the present and the past (Kennett et al., 1985; Gallagher et al., 2009; Gordon et al., 2003b; Sprintall and Révelard, 2014).

Due to the complex tectonic evolution of the ITF region in the last 30 Ma, including convergence and rotation processes, and formation of new ocean basins at the boundaries between the Sundaland-Eurasian and Indian-Australian plates (Kuhnt et al., 2004) the ITF has undergone significant transformations, some of which involving important changes in global climate.

An example is provided by the study by Cane and Molnar (2001), which suggests that the northward movement of New Guinea at ~ 5 Ma caused aridification in eastern Africa, by blocking the entrance of the warmer South Pacific waters into the passage. Within this context, in this thesis, the relative contributions of North and South Pacific waters to the ITF before and after the MMCT are investigated.

The origin of the West Pacific Warm Pool (WPWP) (Yan et al., 1992), the most extensive warm surface water mass on Earth and a very important source for global latent heat and water moisture (Lo et al., 2014), is suggested to be linked to narrowing of the ITF gateway during the Middle Miocene (Gallagher et al., 2009). In our study we investigate whether a similar structure to the present-day WPWP existed during the Middle Miocene and whether it underwent important transformations across the MMCT.

Finally, the study by Gourlan et al. (2008) hypothesizes the existence of an eastward flow through the Indonesian archipelago from the Indian to the Pacific oceans (in addition to the westward flow), prior to ~ 14 Ma. That study suggests that tectonic constriction of the ITF at ~ 14 Ma would have had some cooling effect at a global scale. In our study, the existence of an eastward flow through the ITF gateway before the onset of the MMCT is tested.

Since the ITF region is part of the coral triangle, a marine biodiversity hotspot since at least the late Oligocene (Santodomingo et al., 2016), a characterization of the ITF during the MMCT can also be

useful for paleontological studies aimed at understanding the past evolution of the ocean fauna of the coral triangle, as conceived by the project network which framed this work.

1.5. Scientific aims of the thesis

The application of GCMs to study the MMCT is currently hampered by the lack of appropriate boundary conditions. Oriented towards filling this gap, our **first aim** (chapter two) was the review of Antarctic ice volume and geometry, sea level, and atmospheric CO_2 concentration estimates for the periods before (Middle Miocene Climatic Optimum, MMCO) and after (Middle Miocene Glaciation, MMG) the MMCT, and the assemblage of global topography, bathymetry, and vegetation data representing those periods.

Previous studies point at the atmospheric CO_2 dropdown across the MMCT as one of the main triggers of this climate transition (Holbourn et al., 2005, 2007; Levy et al., 2016; Gasson et al., 2016; Langebroek et al., 2010). The **second aim** (chapter 3) of this thesis was that of assessing, by means of CCSM3 (see sect. 2.1.), the effects of the atmospheric CO_2 dropdown and Antarctic ice sheet expansion on the global ocean. More specifically, the following scientific questions were addressed: 1) could the combined effects of the CO_2 decrease and Antarctic ice sheet expansion explain the cooling of surface and deep waters across the MMCT inferred from proxy data? (Lear et al., 2000, 2010; Shevenell et al., 2004, 2008; Billups and Schrag, 2002, 2003) 2) what were the separate effects of these two forcings on surface and deep water temperatures? 3) what were the mechanisms triggered by these forcings that explain their modeled effects on ocean temperatures?

The **third aim** (chapter 4) was oriented towards the Southeast Asian gateway. We aimed at modeling the ITF during the MMCT. More specifically, we provided estimates of volume transport, analyzed the vertical structure of the waterflow, the direction of waterpaths, determined the relative contributions of North and South Pacific water in the ITF, and investigated the role of winds in the

seasonal variability of the ITF at the MMCT. Besides, we examined whether a similar structure to the WPWP existed during the MMCT in the ITF area.

This thesis is structured as follows:

- **Chapter 2: Methodology**

  This chapter contains a description of the numerical model employed to perform the experiments (CCSM3), together with the experimental design and a detailed review of the model boundary conditions used in the experiments.

- **Chapter 3: Modeling the Middle Miocene Climate Transition – a global approach**

  This chapter aims at investigating the mechanisms behind global ocean cooling during the MMCT. For this, a series of experiments using different Antarctic ice sheet configurations, sea levels, and atmospheric CO_2 concentrations are carried out.

- **Chapter 4: Modeling the Indonesian Throughflow during the MMCT**

  This chapter points at characterizing the Indonesian Throughflow during the MMCT. For this, the same model experiments as in chapter 3 are employed.

1.6. Author's contributions

- **Chapter 2: Methodology**

  Amanda Frigola:

  i. gathered the model boundary conditions
  ii. performed the CCSM3 model setup
  iii. ran the CCSM3 experiments
  iv. processed and analyzed the CCSM3 model output data

v. wrote the chapter

Matthias Prange:

i. devised the project

ii. improved the data analyses and the chapter

Michael Schulz:

i. devised the project

ii. improved the chapter

- **Chapter 3: Modeling the Middle Miocene Climate Transition – a global approach**

Amanda Frigola:

i. ran the CCSM3 experiments

ii. processed and analyzed the CCSM3 model output data

iii. wrote the chapter

Matthias Prange:

i. devised the project

ii. improved the data analyses and the chapter

Michael Schulz:

i. devised the project

ii. improved the chapter

- **Chapter 4: Modeling the Indonesian Throughflow during the MMCT**

Amanda Frigola:

i. processed and analyzed the CCSM3 model output data

ii. wrote the chapter

Matthias Prange:

i. devised the project

ii. improved the data analyses and the chapter

Michael Schulz:

i. devised the project

ii. improved the chapter

2. Methodology

2.1. The Community Climate System Model version 3: configuration

A key tool in this study was the Community Climate System Model version 3 (CCSM3) (Collins et al., 2006), the numerical model employed in our simulations. CCSM3 is a fully coupled GCM developed at the National Center for Atmospheric Research (NCAR) in Boulder, Colorado, constituted of four different geophysical components for atmosphere (Community Atmosphere Model, Collins et al., 2004), ocean (CCSM Parallel Ocean Program, Smith and Gent, 2004), land (Community Land Model, Oleson et al., 2004), and sea ice (Community Sea Ice Model, Briegleb et al., 2004), which exchange information at run time through a fifth component, the coupler.

To accomplish aims two and three described in sect. 1.5., a series of Middle Miocene simulations and a pre-industrial (PI) control simulation (see sect. 2.2.) were performed. The atmosphere horizontal grid employed in the PI simulation, T42, is a Gaussian grid with 64 points in latitude and 128 points in longitude (~ 2.8° resolution). The notation T42 refers to the spectral truncation level. The land and atmosphere models share the same horizontal grid. The ocean horizontal grid, x1, is a dipole grid with 384 points in latitude and 320 points in longitude. The zonal resolution of the ocean horizontal grid is ~ 1°, the mean meridional resolution is ~ 0.5°, refined around the equator (~ 0.3°). The notation x1 refers to the nominal zonal resolution. The ocean and sea–ice components share the same horizontal grid. The atmosphere and ocean vertical grids have 26 and 40 vertical levels, respectively. This model grid configuration is known as T42x1. For the Miocene simulations the same grids as for PI were used, except for the horizontal ocean (and sea–ice) grid, for which a customized grid was used. This grid is also a dipole grid with 384 points in latitude and 320 points in longitude, although extended to ~87° S (instead of ~79° S) in order to accommodate changes in the bathymetry off West Antarctica. In the Miocene topography/bathymetry datasets, West

Antarctica is mostly below sea level, with ocean reaching down to ~85° S. If the standard CCSM3 grid had been used for the Miocene experiments, the ocean region between ~79° and 85° S would not have been taken into account in the ocean circulation simulations.

The model setup for the Miocene experiments required substantial adjustments, since deep time simulations employ boundary conditions that differ significantly from those of the present-day default model configuration. This series of adjustments were performed according to the NCAR CCSM3 setup manual for paleoruns (Rosenbloom et al., 2011) and include the creation of a kmt file (or global bathymetry file) representing the Middle Miocene, a land surface model biome map reproducing Middle Miocene global vegetation distribution and land ice cover, and a river routing dataset based on Middle Miocene topography (see Appendix A for further details on the Middle Miocene model setup procedure).

2.2. Experimental design and boundary conditions

Four Middle Miocene experiments named MMCO, MMG, MMCO200, and MMG400, plus a PI control experiment, named PI, were performed with CCSM3.

In the PI experiment, well-mixed greenhouse gases, ozone distribution, aerosols, solar constant and orbital configuration were set to PI following Otto-Bliesner et al. (2006) (Table 2.1.). In the Miocene experiments, the same values as in PI were used, except for the atmospheric CO_2 levels (Table 2.1.).

All Miocene experiments used Middle Miocene global topography, bathymetry (sect. 2.2.4.) and vegetation (sect. 2.2.5.). The experimental designs of the four Miocene experiments differ from each other in terms of Antarctic ice sheet geometry, sea level, and atmospheric CO_2 levels (sect. 2.2.1.–2.2.3.). The MMCO and MMG experiments represent the periods before (Middle Miocene

Experiment	PI	MMCO	MMG	MMCO200	MMG400
CO_2	280 ppmv	400 ppmv	200 ppmv	200 ppmv	400 ppmv
CH_4	760 ppbv	same as PI			
N_2O	270 ppbv				
CFC's	0				
O_3	1870 A.D.				
Sulfate aerosols	1870 A.D.				
Dust and sea salt	PD				
Carbonaceous aerosols	30% of PD				
Solar constant	1365 W m^{-2}				
Eccentricity	0.016724				
Obliquity	23.446 °				
Precession	102.04 °				

Table 2.1. *Summary of atmospheric composition, solar constant, and orbital configuration for the CCSM3 experiments. PI values are according to Otto-Bliesner et al. (2006). The orbital configuration represents 1950 AD values. PD is present-day.*

Climatic Optimum) and after (Middle Miocene glaciation) the MMCT, respectively (Table 2.2.). The other two Miocene experiments, MMCO200 and MMG400, are sensitivity experiments aimed at disentangling the effect of the Antarctic ice sheet expansion from that of the CO_2 decrease. In the MMCO200 experiment, all boundary conditions are kept the same as in MMCO, except for CO_2,

	MMCO	MMG	MMCO200	MMG400
Atmospheric CO_2 concentration	400 ppmv	200 ppmv	200 ppmv	400 ppmv
Antarctic ice sheet volume	6 million km³	23 million km³	same as MMCO	same as MMG
Sea level	48 m higher than at present-day	5 m higher than at present-day		
Global topography/bathymetry	mainly Herold et al. (2008) with modifications for tropical seaways (Hall, 2012; Montes et al., 2012) and the Antarctic ice sheet	same as MMCO, but with global sea level reduced by 43 m and an expanded Antarctic ice sheet		
Global vegetation	mainly Pound et al. (2012) with gaps filled according to Wolfe (1985) and Morley (2011); ice and tundra in Antarctica	same as MMCO, but with tundra removed in Antarctica		

Table 2.2. *Summary of Antarctic ice sheet volume, sea level, CO_2 topography/bathymetry, and vegetation for the Middle Miocene experiments.*

which is lowered to 200 ppmv (same value as in MMG). The MMG400 experiment has a design identical to that of MMG, except for CO_2, which is set to 400 ppmv (as in MMCO).

The PI experiment was branched from the NCAR CCSM3 1870 CE control run and integrated another 150 years (850 years in total). The Miocene experiments were integrated for a total of 1500 years. The last 100 years of each of the 5 simulations were used for the analyses. The temperature trends in the deep ocean (at 4–5 km depth) are < 0.14, 0.15, 0.17, 0.185, and 0.13° C/100 years in the PI, MMCO, MMG, MMCO200, and MMG400 cases, respectively. At that same depth range, the salinity trends are < 0.01, 0.007, 0.01, 0.014, and 0.025 g/kg/100 years for PI, MMCO, MMG, MMCO200, and MMG400, respectively. Although only a quasi-equilibrium state was reached, tendencies are clear and allow for a robust interpretation of the model results.

The global topography and bathymetry datasets employed in our Middle Miocene experiments are mainly based on the Middle Miocene reconstruction by Herold et al. (2008), which has been used in previous modeling studies (e.g., Herold et al., 2012, 2011; Krapp and Jungclaus, 2011). However, we implement some important modifications with regard to configuration of the Southeast Asian and Panama seaways taking into account recent reconstructions (sect. 2.2.4.). Besides, in our topography/bathymetry datasets, we distinguish between the MMCO and MMG periods, according to the different Antarctic ice sheet geometries and sea level.

Vegetation cover used in most previous Middle Miocene modeling studies with prescribed vegetation was mainly based on Wolfe's (1985) Early Miocene reconstruction (e.g., Herold et al., 2011; Tong et al., 2009; You et al., 2009). Here, Middle Miocene data (Pound et al., 2012; Morley, 2011) were also used. Land ice/tundra distribution on Antarctica for the MMCO and MMG periods in our global vegetation datasets is coherent with the respective Antarctic ice sheet geometries of those periods (sect. 2.2.5.).

At the end of this chapter, in order to provide evidence of the suitability of our boundary conditions for global climate modeling, some general CCSM3 results employing them are presented (sect.

2.2.6.).

2.2.1. Antarctic ice sheet geometry

Giving quantitative Antarctic ice volume estimates for the MMCT is at best challenging. Most sediment core studies present ice volume estimates in units of seawater $\delta^{18}O$. Backstripping methods provide sea level rather than ice volume estimates. More direct Antarctic ice volume estimates can be derived from modeling studies (Gasson et al., 2016; Langebroek et al., 2009; Oerlemans 2004).

Gasson et al. (2016) performed a series of simulations with an ice sheet model asynchronously coupled to a regional climate model and an isotope-enabled GCM using Middle Miocene paleogeography and a range of atmospheric CO_2 concentrations and extreme astronomical configurations. The study tested two different Antarctic bedrock topography scenarios: one scenario with present-day bedrock topography and the other one with an approximate Middle Miocene bedrock topography. For a range of CO_2 concentrations between 500 and 280 ppmv and changing orbital parameters ("warm astronomical configuration" versus "cold astronomical configuration") an increase in Antarctic ice volume from 11.5 (17.2) million km³ in the warmer climate to 26.7 (35.5) million km³ in the colder climate was simulated using modern (Middle Miocene) bedrock topography.

Langebroek et al. (2009) used a coupled ice sheet–climate model forced by atmospheric CO_2 and insolation changes to reconstruct Antarctic ice volume across the MMCT. The experiment with the best fit to $\delta^{18}O$ data was forced by a CO_2 drop from 640 ppmv to 590 ppmv at around ~ 13.9 Ma and simulates an increase in Antarctic ice volume from ~ 6 million to ~ 24 million km³ across the MMCT.

Oerlemans (2004) derived Cenozoic Antarctic ice volume variations by means of a simple quasi-analytical ice sheet model and two different $\delta^{18}O$ benthic foraminiferal records. The ice sheet model

approximates Antarctic ice volume as a function of deep sea temperature. Using the Zachos et al. (2001) benthic foraminiferal $\delta^{18}O$ data, an ice volume increase from ~ 5 million to ~ 23 million km³ for the MMCT was obtained, while for the $\delta^{18}O$ curve by Miller et al. (1987) the increase was only from ~ 15 million to ~ 23 million km³.

Mainly based on the studies by Oerlemans (2004) and Langebroek et al. (2009), we set a total Antarctic ice sheet volume of 23 million km³ for the MMG (Table 2.2.; Fig. 2.1.). This value is within the range of published estimates, although smaller than the values estimated by Gasson et al. (2016) in their "cold climate" experiments with extreme astronomical configuration. For the MMCO we assume a total Antarctic ice sheet volume of 6 million km³. This volume estimate is in good agreement with the values given by Langebroek et al. (2009) and Oerlemans (2004), although significantly lower than Gasson et al. (2016) (see above).

In this study, we opted for using ice sheet model-derived Antarctic topography estimates from an earlier Cenozoic time period with similar Antarctic ice volume. These data were kindly provided by David Pollard (Pennsylvania State University) and correspond to the Oligocene Oi-1 glaciation event. They were obtained with a model version close to that described in Pollard and DeConto (2012), but with no marine ice physics, so that any floating ice is immediately removed. The bedrock-elevation boundary conditions used in that run are from the modern ALBMAPv1 dataset (Le Brocq et al., 2010). Climate forcing is obtained from a matrix of GCM climates for various orbits, CO_2 levels and ice sizes (Pollard, 2010). Insolation is based on Laskar et al. (2004). The run is 12 Myr long, nominally from "37 Ma to 25 Ma". The configuration we used to represent MMCO conditions corresponds to 34.8 Ma; the one representing MMG conditions, to 33 Ma.

In the MMG configuration the whole East Antarctica is covered with a single ice sheet meanwhile the islands of West Antarctica contain only some small ice caps, with no marine-based ice sheets. In the MMCO configuration Antarctica is only partially glaciated, with an ice cap covering the

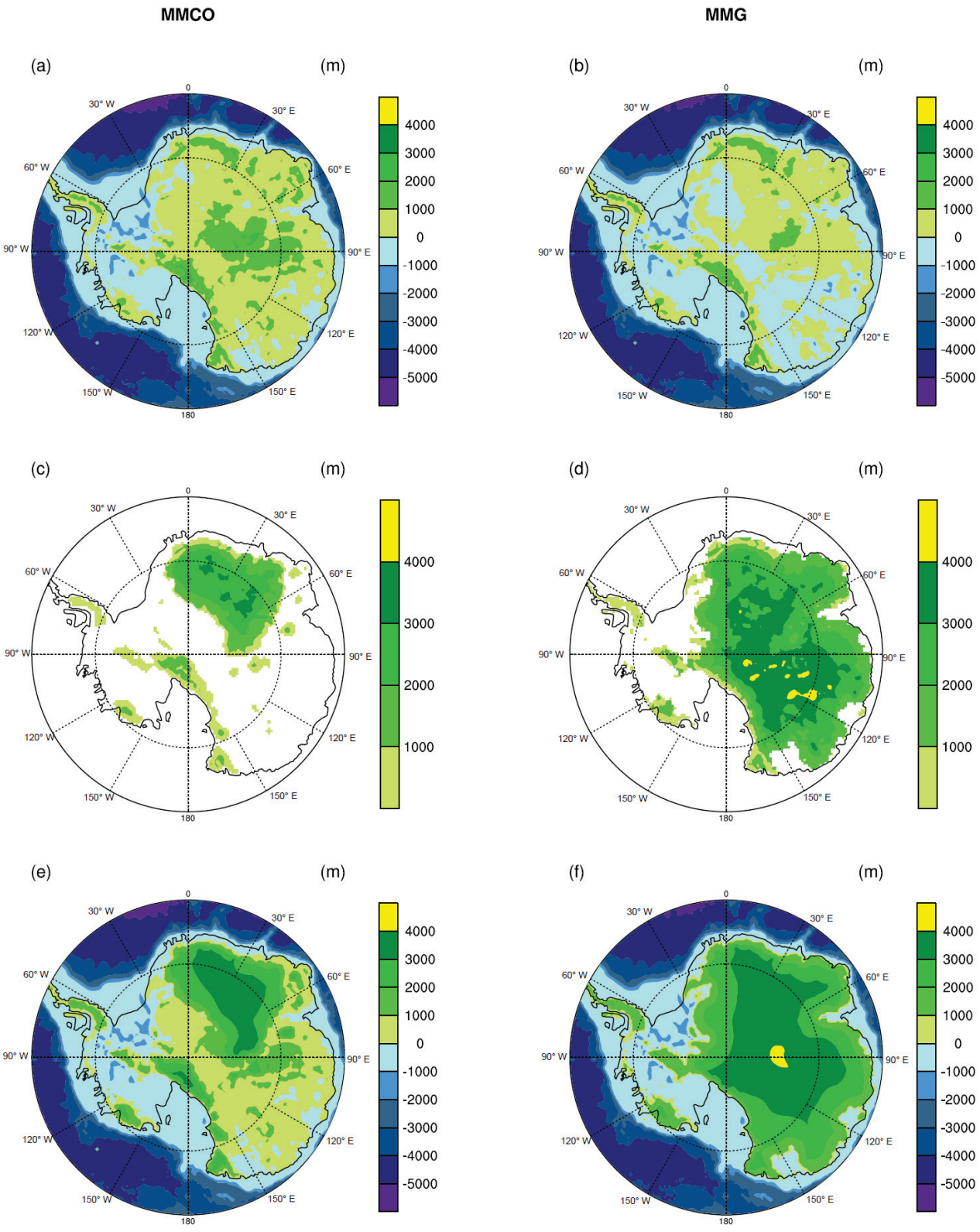

Figure 2.1. *Reconstruction of Antarctica for the Middle Miocene Climatic Optimum (MMCO) and the Middle Miocene Glaciation (MMG): (a), (b) bedrock elevation; (c), (d) ice thickness; (e), (f) surface elevation (bedrock elevation + ice thickness), in meters. Black lines represent the present-day coastline. Data from David Pollard.*

Transantarctic Mountains and another one over eastern East Antarctica. Again, West Antarctica contains only some ice caps, with no marine-based ice sheets (Fig. 2.1.). We deem the ice configurations from the Oi-1 glaciation run appropriate for the MMCT as they match total ice volumes of 23 million km³ for the MMG and of 6 million km³ for the MMCO, values that are within the range of published ice volume estimates for the MMG and MMCO, respectively. Besides, there is little to link Pollard's run to a specific time period (except for the Laskar orbits). The configurations of Oerlemans (2004) and Langebroek et al. (2009) were discarded in our study because they are rather simple (no two-dimensional representation of the Antarctic ice sheet is available from those studies). The configuration of Gasson et al. (2016) could be considered in future sensitivity studies, since uncertainties in ice volume estimates are high. Nevertheless, the distribution of ice in our study is comparable to that in Gasson et al. (2016): for the MMG, a continental-scale ice sheet exists in East Antarctica with ice thicknesses of ~ 3000–4000 m, although in West Antarctica there is less ice in Pollard's data; for the MMCO, the ice sheets occupy similar positions, although they are less extensive in Pollard's data.

The ice volume values of 6 million and 23 million km³ for the MMCO and the MMG, respectively, imply an increase of 17 million km³ across the MMCT. This value is within the range of published estimates and in reasonable agreement with the values by Langebroek et al. (2009), Oerlemans (2004) as well as Gasson et al. (2016) (see above).

Although some studies suggest ice would have been present in the Northern Hemisphere during the Middle Miocene (Thiede et al., 2011; DeConto et al., 2008), little is known about its temporal and spatial distribution. In view of the lack of concrete data, Northern Hemisphere ice was neglected in the current study.

2.2.2. Sea level change across the MMCT

For the sake of coherency within the current set of Middle Miocene boundary conditions, we opted

for a sea level change across the MMCT that is consistent with our ice sheet volume estimates for the MMCO and MMG (see sect. 2.2.1.), presuming that global sea level change across the MMCT time interval was dominated by glacio-eustasy. The ice sheet volume estimates were converted into sea level equivalents according to the following equation (Langebroek et al., 2009):

$S_{eq} = (\rho_{ice} * V_{ice}) / (\rho_{water} * A_0)$ (1)

where S_{eq} represents sea level equivalent, V_{ice} ice sheet volume, ρ_{ice} density of ice, ρ_{water} density of water, and A_0 ocean surface area. With ρ_{ice} = 910 kg/m³, ρ_{water} = 1000 kg/m³ and A_0 = 360.5 million km² (present-day approx.), values of 16 and 59 m for the MMCO and the MMG respectively were obtained (as in Langebroek et al., 2009), and thus a sea level fall across the MMCT of 43 m (Table 2.2.).

Lear et al. (2010) combine Mg/Ca and Li/Ca ratios to estimate bottom water temperature (BWT) at ODP Site 761 across the MMCT. Seawater $\delta^{18}O$ is then derived by extracting the BWT signal from the $\delta^{18}O$ signal from the same site. The data suggest an increase in seawater $\delta^{18}O$ of 0.6 per mil between 15.3 and 12.5 Ma. This value is converted into a sea level fall equivalent using the Pleistocene calibration of 0.08–0.11 per mil per 10 m sea level (Fairbanks and Matthews, 1978), obtaining an eustatic sea level drop of ~ 55–75 m between 15.3 and 12.5 Ma.

De Boer et al. (2010) used one-dimensional ice sheet models and benthic foraminiferal $\delta^{18}O$ data (Zachos et al., 2008) to derive eustatic sea level and BWT changes over the last 35 Ma. In their approach, surface air temperature has been derived through an inverse procedure from the benthic $\delta^{18}O$ record. The study suggests a sea level drop of ~ 40 m between 15 and 12 Ma, i.e., from ~ 55 to ~ 15 m above present-day.

Kominz et al. (2008) combine data from different boreholes collected from the New Jersey and Delaware Coastal Plains to derive sea level for the last 108 Ma through backstripping. They register a ~ 20 m sea level fall between ~ 14.2 and ~ 12.8 Ma, i.e., from ~ 25 to ~ 5 m above present-day. These data contain some unconformities however, implying that the actual amplitude of the MMCT

sea level drop could have been indeed higher than proposed there.

John et al. (2011) estimate Middle Miocene sea level changes based on backstripping and benthic foraminiferal oxygen isotope data. Backstripping is applied to sediment core data from the Marion Plateau, offshore Northeastern Australia, obtaining a range of sea level variations which is then further constrained using benthic foraminiferal $\delta^{18}O$ data from Zachos et al. (2001). John et al. (2011) suggest a 53–69 m sea level fall between 16.5 and 13.9 Ma. Unfortunately, their analyses are limited to this time interval.

Our sea level fall estimate of 43 m across the MMCT is consistent with Langebroek et al. (2009) (~ 43 m) and in good agreement with the study by De Boer et al. (2010) (~ 40 m), although somewhat larger than the values by Gasson et al. (2016) (~ 30–36 m) and considerably higher than Kominz et al. (2008) estimate (~ 20 m of sea level fall). By contrast, John et al. (2011) suggest a higher amplitude of sea level drop (~ 53–69 m), similar to the ~ 55–75 m by Lear et al. (2010). As such, our assumption of 43 m sea level fall lies well within the range of published estimates.

2.2.3. Atmospheric CO_2 concentration

Numerous studies based on both marine (Foster et al., 2012; Pearson and Palmer, 2000; Tripati et al., 2009; Pagani et al., 2005) and terrestrial (Retallack, 2009; Kürschner et al., 2008) proxies reconstructing Middle Miocene atmospheric CO_2 levels are present in the literature. However, the range of published estimates is rather wide. The difference in the CO_2 estimates between the various studies arises most likely from method-related uncertainties and/or the relatively coarse temporal resolution of some of the datasets. Based on planktonic foraminiferal boron isotopic data, Foster et al. (2012) suggest atmospheric pCO_2 values reaching a maximum of ~ 390 ppmv at ~ 15.8 Ma and decreasing to ~ 200 ppmv by ~ 12 Ma. Pearson and Palmer (2000), using the same method, obtain a maximum value of ~ 300 ppmv at ~ 16.2 Ma followed by a decline to ~ 140 ppmv by ~ 14.7 Ma and an increase to ~ 225 ppmv by ~ 11.4 Ma. Tripati et al. (2009), by means of surface-dwelling

foraminiferal boron/calcium ratios, obtain a maximum value of ~ 430 ppmv at ~ 15.1 Ma followed by a decrease to ~ 340 ppmv by ~ 12 Ma and down to ~ 230 ppmv by ~ 9.9 Ma. Retallack (2009), based on carbon isotopes of pedogenic carbonate, suggests atmospheric pCO_2 levels reaching a maximum of ~ 850 ppmv at ~ 15.6 Ma, dropping down to ~ 115 ppmv by ~ 14.6 Ma and increasing to ~ 430 ppmv by ~ 12.8 Ma. Kürschner et al. (2008) use stomatal-density data from fossil leaves to support pCO_2 values reaching a maximum over ~ 400–500 ppmv at ~15.5 Ma, decreasing to ~ 280 ppmv by ~ 14 Ma and increasing to ~ 340 ppmv by ~ 12 Ma. By contrast, Pagani et al. (2005), using a method based on alkenone carbon isotopes, obtain pCO_2 values oscillating between ~ 200 ppmv and ~ 300 ppmv across the Middle Miocene.

We chose atmospheric CO_2 concentrations of 400 ppmv and 200 ppmv to represent the MMCO and the MMG respectively (Table 2.2.). Although somewhat arbitrary, these values are within the range of published estimates. The 400 ppmv MMCO value is in favorable agreement with Foster et al. (2012) (~ 392 ppmv at ~ 15.8 Ma) and Tripati et al. (2009) (~ 430 ppmv at ~ 15.1 Ma), although higher than Pearson and Palmer (2000) (~ 300 ppmv at ~ 16.2 Ma) and Pagani et al. (2005) (~ 300 ppmv at ~ 15 Ma), and lower than Kürschner et al. (2008) (> ~ 400-500 ppmv at ~ 15.5 Ma) and Retallack (2009) (~ 852 ppmv at ~ 15.6 Ma) maxima. The 400 ppmv estimate is also in good agreement with the most recent alkenone- and boron isotope-based pCO_2 reconstructions for the MMCO by Zhang et al. (2013) and Greenop et al. (2014). The 200 ppmv MMG estimate is in good agreement with Foster et al. (2012) (~ 200 ppmv at ~ 12 Ma) and Pagani et al. (2005) (~ 200 ppmv at ~ 13 Ma), although higher than Pearson et al. (2000) (~ 140 ppmv at ~ 14.7 Ma) and Retallack (2009) (~ 116 ppmv at ~ 14.6 Ma), and lower than Tripati et al. (2009) (~ 340 ppmv at ~ 12 Ma) and Kürschner et al. (2008) (~ 280 ppmv at ~ 14 Ma) minima.

2.2.4. Global topography and bathymetry

We present here two different global Middle Miocene topography/bathymetries, characterizing the

MMCO and the MMG periods (Fig. 2.2., Table 2.2.). Both global topography/bathymetries are mainly based on the 2°x2° reconstruction of Herold et al. (2008), although some important modifications, which will be described below, were applied to their original dataset. To reconstruct paleogeography and paleotopography Herold et al. (2008) used a global plate rotation model and geological data. Ocean depth was reconstructed by applying an age–depth relationship to a global Middle Miocene isochron map. Sediment thickness and large igneous provinces were also considered in the reconstruction of ocean depth.

In Herold et al. (2008), the Andes and the Tibetan plateau were set with estimated Early to Middle Miocene elevations. The Rocky Mountains and the east African topography were reduced to 75 and 25 % of their current elevation, respectively. The Greenland topography was also reduced, representing ice-free conditions. The Bering Strait was closed and the Hudson Bay removed. Unlike Herold et al. (2008), who assumed the Tethys seaway closed, we decided to leave the seaway open (based on a modification by the authors of Herold et al., 2008; Nicholas Herold, personal communication, 2011). According to Rögl (1999), the Tethys passage closed during the Burdigalian (20.44–15.97 Ma), re-opened temporary during the Langhian (15.97–13.65 Ma) and closed again during the Serravallian (13.65–11.62 Ma). Also based on Rögl (1999), the Paratethys was intermittently connected and disconnected from the global ocean during the Burdigalian to Serravallian interval. In Herold et al. (2008), as in our reconstruction, the Paratethys is connected to the global ocean. In view of the variable configuration of the Tethys/Paratethys across the Middle Miocene, it would be recommendable to test different Tethys/Paratethys configurations when performing Middle Miocene experiments with GCMs, although such testing can be limited by model constraints: seas disconnected from the global ocean can produce freshwater imbalance in GCMs and narrow ocean passages require high resolution ocean grids to allow ocean flux calculation (Rosenbloom et al., 2011). Some studies, indeed, suggest that the Tethys passage closure might have played a role in Middle Miocene atmosphere and ocean circulation patterns (Ramstein

et al., 1997; Hamon et al., 2013).

Additional important modifications were applied to the original dataset of Herold et al. (2008) regarding Antarctic ice sheet geometry, sea level and configuration of the Southeast Asian and Panama seaways (see discussion below in subsections 2.2.4.1.–2.2.4.4.) (Fig. 2.3.).

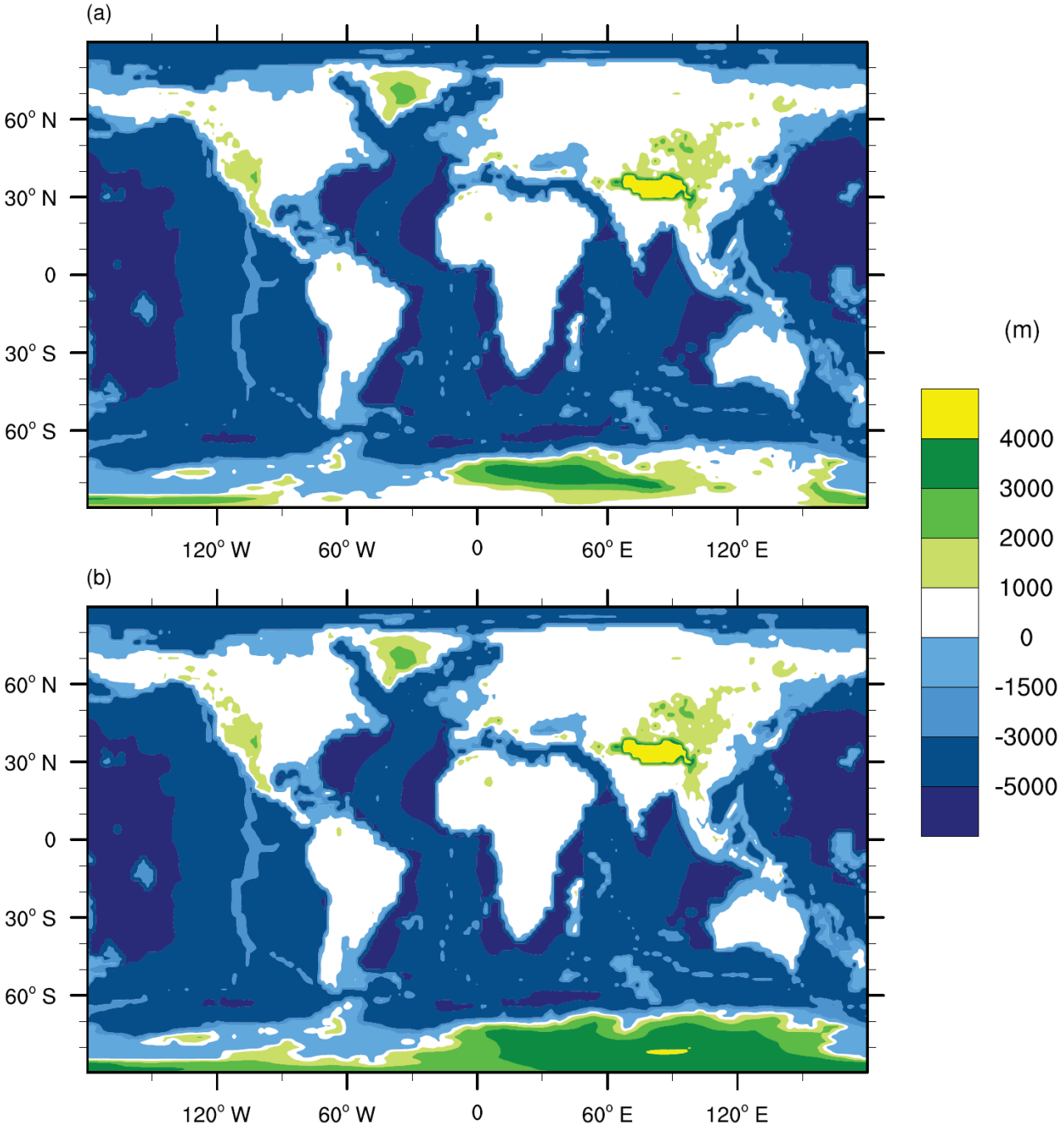

Figure 2.2. *Topography/bathymetry reconstruction for the (a) MMCO and the (b) MMG.*

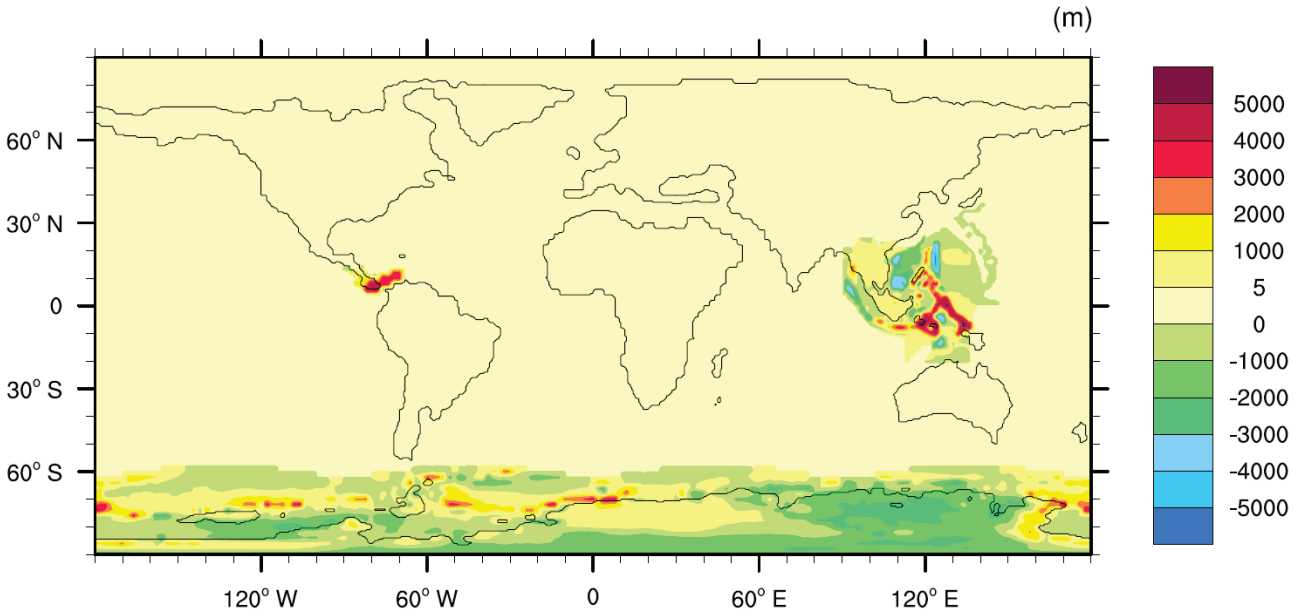

Figure 2.3. *Difference between MMCO and the topography/bathymetry by Herold et al. (2008), in meters. Sea level is 4 m higher in the MMCO dataset (subsection 2.2.4.2.), the Indonesian Throughflow barriers are shallower (subsection 2.2.4.3.), the Panama seaway is narrower (subsection 2.2.4.4.), and the Antarctic topography/bathymetry is based on David Pollard's data (subsection 2.2.4.1.) and consistent with MMCO ice volume estimates.*

2.2.4.1. Antarctica

Antarctic ice sheet geometry was modified for consistency with our ice sheet volume estimates for the MMCO and MMG (see sect. 2.2.1.). In the high southern latitudes, from 60° S to 90° S, the original topography/bathymetry from Herold et al. (2008) was replaced by the Antarctic topography/bathymetry data from David Pollard described above (Fig. 2.1. e, f).

2.2.4.2. Sea level

Sea level was adjusted to ~ 48 m and ~ 5 m above present-day for the MMCO and MMG, respectively (Table 2.2.). These values were derived from our sea level equivalent estimates (see above) by assuming 64 m of present-day sea level equivalent. This present-day estimate is in good agreement with Vaughan et al. (2013) (58.3 m for the Antarctic ice sheet and 7.36 m for the

Greenland ice sheet). The adjustments were applied taking into account that sea level is ~ 52 m above present-day in Herold et al. (2008) (Nicholas Herold, pers. comm.) and at present-day level in David Pollard's data. We note that the sea level adjustment of 4 m (i.e. 48 m above present-day instead of 52 m) with respect to Herold et al. (2008) for the MMCO is minor and has virtually no effect in common global climate models at low spatial resolution.

2.2.4.3. Southeast Asian gateway

Southeast Asian paleogeography was modified based on Hall's (2012) reconstruction constrained at 15 Ma (Fig. 2.4.). Hall's data, available as a georeferenced image, were converted into grid format using ArcGIS. Qualitative height/depth values were assigned to the different geographic features: ~ 2800 m for volcanoes, ~ 1000 m for highlands, ~ 250 m for land, ~ -22 m for carbonate platforms, ~ -200 m for shallow sea, < -4000 m for deep sea, and ~ -5500 m for trenches. After embedding the data into the MMCO global dataset, minor manual smoothing was applied at the margins of the embedded region. Here, shallow bays were removed and single, shallow grid points surrounded by much deeper grid points were deepened to the adjacent depth. In total, these modifications affected ~ 0.5 % of the total number of grid points.

Based on the depth values assigned to the different geographic features in the Southeast Asia reconstruction, the deepest connection between the Indian and the Pacific Ocean would be only ~ 200 m deep. This is probably too shallow, since in the Middle Miocene the Indonesian gateway was likely open to both surface and intermediate water (Kuhnt et al., 2004). Deep water passages were therefore added to the MMCO global topography/bathymetry dataset, based on the postulated Middle Miocene ocean paths across the Indonesian archipelago described in Kuhnt et al. (2004) (Fig. 2.4.). The depth values assigned to these passages are shallower than those of the present-day passages (Kuhnt et al., 2004). Based on an educated guess the depths of the two eastern passages were set to 800 m, shallower than those of the present-day eastern Lifamatola (~ 1940 m) and Timor (~ 1300–1450 m) passages (Gordon et al., 2003a). The northwestern passage was assigned a depth

of 1000 m, shallower than that of the present-day northwestern Sangihe Ridge sill (~ 1350 m) (Gordon et al., 2003a). The depth of the southwestern passage was set to 600 m, slightly shallower than that of the present-day southwestern Dewakang sill (680 m) (Gordon et al., 2003a). Assigned widths are somewhat arbitrary. The eastern passages were both given a width of ~ 150 km (~ 3 grid cells), and the northwestern and southwestern passages a width of ~ 350 km (~ 6 grid cells) and ~ 220 km (~ 4 grid cells) respectively.

For the MMG, the same Southeast Asia topography/bathymetry reconstruction was used as for the MMCO after applying a ~ 43 m sea level change, in correspondence with our MMCT sea level fall estimate (see above).

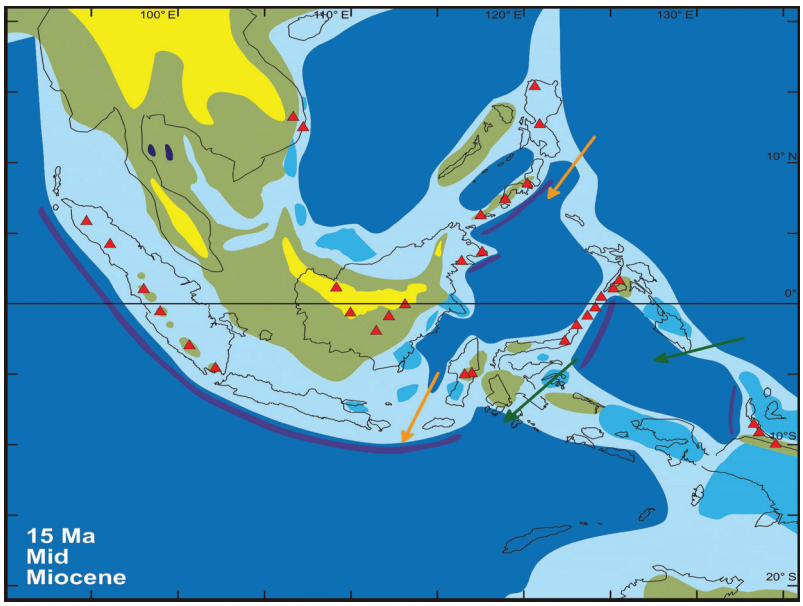

Figure 2.4. *Paleogeographic reconstruction of Southeast Asia for 15 Ma from Hall (2012). Geographic features: volcanoes in red (triangles), highlands in yellow, land in green, carbonate platforms in blue, shallow sea in light blue, deep sea in dark blue, and trenches in violet. Figure courtesy of Robert Hall (Royal Holloway, University of London). Arrows represent Middle Miocene postulated ocean paths across the Indonesian archipelago and are based on Kuhnt et al. (2004). Eastern paths shown in green, western paths in orange.*

2.2.4.4. Panama seaway

Also the Panama seaway was modified such that substantial differences exist compared to the original dataset of Herold et al. (2008). Montes et al. (2012) suggest a narrow Panama strait already by the Early Miocene, with a width of ~ 200 km. Therefore, the width of the seaway was set accordingly in our paleogeographic dataset, together with a depth of ~ 1000 m which reflects Panama sill reconstructions for the Middle Miocene by Duque-Caro (1990).

2.2.5. Global vegetation

The current MMCO and MMG global vegetation reconstructions (Fig. 2.5.) were based on Pound et al. (2012), Wolfe (1985) and Morley (2011). The study by Pound et al. (2012) includes global vegetation reconstructions for the Langhian (15.97–13.65 Ma) (approximately the end of the MMCO) and the Serravallian (13.65–11.61 Ma) (roughly coincident with the MMG). Wolfe's (1985) study contains an Early Miocene global vegetation reconstruction. The reconstructions from Pound et al. (2012) and Wolfe (1985) are the only Early/Middle Miocene global reconstructions. Morley's (2011) Middle Miocene reconstruction focuses only on the distribution of tropical forests.

The study by Pound et al. (2012), based on paleobotanical evidence from 617 Middle/Late Miocene data locations, constituted the main source of global vegetation data for our MMCO and MMG boundary conditions. Morley's (2011) study added some detail to the current reconstructions in the tropical areas. Wolfe's (1985) Early Miocene data were used in regions where the Middle Miocene reconstructions by Pound et al. (2012) and Morley (2011) had scarce data coverage and also to characterize the vegetation patterns of the main mountain ranges.

The above mentioned studies use different nomenclatures to classify the different types of vegetation. Pound et al. (2012) use the BIOME4 classification (Kaplan, 2001), while Wolfe (1985) uses the classification scheme described in Wolfe (1979). Here, we coded the data in the Land Surface Model (LSM) (Bonan, 1996) biome classification scheme. All biome names in this study

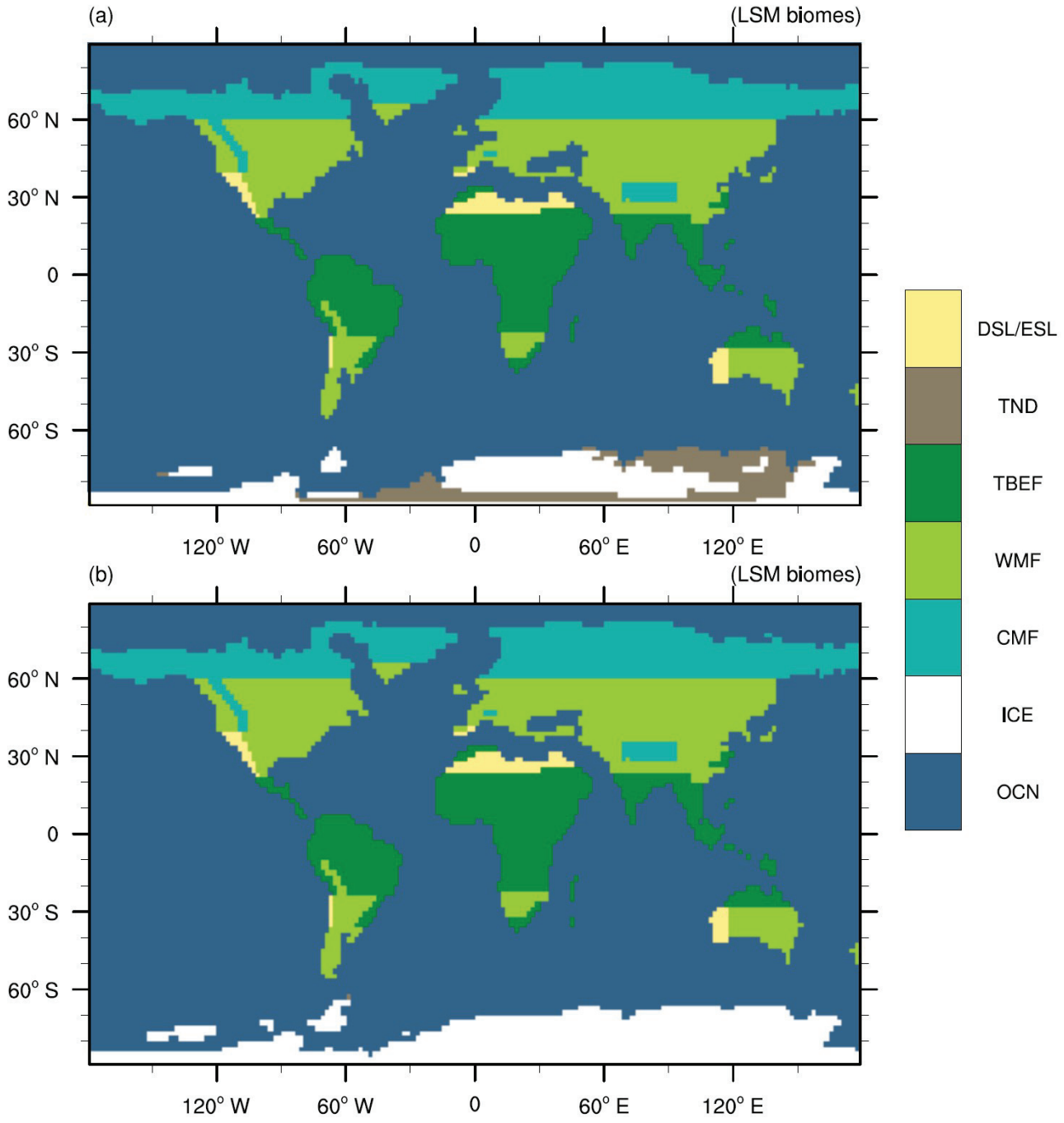

Figure 2.5. *Vegetation reconstruction for the (a) MMCO and the (b) MMG. Colors represent LSM biomes: DSL = deciduous shrubland, ESL = evergreen shrubland, TND = tundra, TBEF = tropical broadleaf evergreen forest, WMF = warm mixed forest, CMF = cool mixed forest, ICE = land ice, and OCN = ocean.*

are in italics, with LSM biome names in addition set in quotation marks. Table 2.3. shows how the data from Pound et al. (2012), Wolfe (1985) and Morley (2011) were converted into the LSM scheme. However, we note that the correspondence between biomes of different schemes is not always optimal (see notes in Table 2.3.). The *warm-temperate evergreen broadleaf and mixed forest* BIOME4 biome was converted into the LSM scheme as "*warm mixed forest".* The "*warm mixed forest"* LSM biome represents a mixture of needleleaf evergreen temperate trees and broadleaf deciduous temperate trees, meanwhile the *warm-temperate evergreen broadleaf and mixed forest* BIOME4 biome represents either a) temperate broadleaf evergreen trees alone, or b) cool conifer trees mixed with temperate broadleaf evergreen trees, or c) temperate deciduous trees mixed with either temperate broadleaf evergreen trees or cool conifer trees. The conversion is suboptimal because no broadleaf evergreen temperate trees are present in the "*warm mixed forest"* LSM biome. Nevertheless, the "*warm mixed forest"* still constitutes a fair representation of the *warm-temperate evergreen broadleaf and mixed forest* BIOME4 biome. In case a more precise representation in the LSM scheme of the *warm-temperate evergreen broadleaf and mixed forest* BIOME4 biome was required, the LSM scheme could be modified by adding a new biome containing the exact specific plant types present in the *warm-temperate evergreen broadleaf and mixed forest* BIOME4 biome described above (a similar approach is used in Herold et al., 2010). Note also that Table 2.3. does not contain all the biomes present in the different vegetation schemes, but only the ones effectively used in the current reconstructions.

Neither Pound et al. (2012) nor Wolfe (1985) or Morley (2011) provide the data in a gridded format, a requirement for the use in GCMs. According to the geographical coordinates specified in those reconstructions, we merged the data on a 2°x2° latitude/longitude grid for MMCO and MMG, giving preference to the Middle Miocene reconstructions by Pound et al. (2012) and Morley (2011). The Early Miocene reconstruction of Wolfe (1985) was only used at locations where no data are available from the other two reconstructions. An exception are the Alps, Rocky Mountains,

BIOME4	**LSM**
tropical evergreen broadleaf forest	tropical broadleaf evergreen forest
tropical deciduous broadleaf forest and woodland	tropical broadleaf deciduous forest
warm-temperate evergreen broadleaf and mixed forest	warm mixed forest[1]
cool-temperate mixed forest	cool mixed forest[2]
tropical savanna	savanna
temperate xerophytic shrubland	evergreen shrub land or deciduous shrub land
temperate deciduous broadleaf savanna	deciduous shrub land
temperate grassland	cool grassland
low- and high-shrub tundra	tundra
prostrate dwarf-shrub tundra	tundra
ice	land ice
Wolfe's (1979) classification	**LSM**
mixed coniferous forest	cool mixed forest[3]
tropical rain forest	tropical broadleaf evergreen forest
paratropical rain forest	tropical broadleaf evergreen forest[4]
Morley's (2011) classification	**LSM**
megathermal rain forest	tropical broadleaf evergreen forest
monsoonal megathermal forest	tropical broadleaf deciduous forest

Table 2.3. *Conversion of vegetation types to the LSM vegetation scheme.*

[1] The warm-temperate evergreen broadleaf and mixed forest may contain broadleaf evergreen trees, needleleaf evergreen trees and deciduous trees. The warm mixed forest contains needleleaf evergreen trees and deciduous trees, but not broadleaf evergreen trees. [2] The deciduous trees in the cool-temperate mixed forest are temperate, meanwhile the ones in the cool mixed forest are boreal. [3] The mixed coniferous forest is mainly needleleaf evergreen, but broadleaf trees are also present. These can be deciduous or evergreen. The cool mixed forest is formed by needleleaf evergreens and broadleaf deciduous. Broadleaf evergreens are not present. [4] The paratropical rain forest is mainly broadleaf evergreen, but it may contain some broadleaf deciduous and conifers.

Himalayas and Tibetan Plateau, where we used the information from Wolfe (1985). At the regions where the reconstructions from Pound et al. (2012) and Morley (2011) were conflicting with each other, the reconstruction of Pound et al. (2012) was used, except for locations where the latter was less well constrained by proxy information than Morley (2011).

The MMCO and the MMG global vegetation reconstructions presented here solely differ in terms of

"tundra" distribution on Antarctica (Fig. 2.5.). In both reconstructions *"tundra"* was assigned to the ice-free regions of Antarctica, taking account of the MMCO and MMG ice sheet geometries (Fig. 2.1.c, d). Assuming the *"tundra"* distribution to be the only difference in terms of vegetation between the MMCO and the MMG is a simplification. Part of the *warm-temperate evergreen broadleaf and mixed forest* (*"warm mixed forest"* in the LSM scheme) present in the middle latitudes during the Langhian was replaced by "cooler and/or drier temperate biomes" during the Serravallian (Pound et al., 2012). This cooling and/or drying trend was observed for example in areas like western North America or Europe (Pound et al., 2012). Additionally, by the Serravallian, in the tropics, some drier biomes than those present there during the Langhian had started to spread (e.g. in Southeast Asia) (Pound et al., 2012). Nevertheless, the Langhian and Serravallian global vegetation patterns were 'similar' in comparison with the 'markedly different biome pattern of the Tortonian from that of the Serravallian' (see Fig. 5. and Fig. 6. in Pound et al., 2012), which justifies our simplified approach. However, for studies with a specific focus on vegetation-triggered climatic changes across the MMCT, the user could modify our MMG vegetation dataset (LSM scheme) as follows (based on Pound et al., 2012): a) in the mid-latitudes of western North America, the *"warm mixed forest"* between 40 and 50° N could be partly replaced with *"warm broadleaf deciduous forest"*. Also a *"cool mixed forest"* could be added in the same region at 42° N; b) in Europe, some *"deciduous shrub land"* could be added to the *"warm mixed forest"* in southern France between 42.5–44° N and 6–9° E, and also between 38–47° N and 29–36° E.

We are aware that the Middle Miocene global vegetation reconstructions presented here are rather coarse. Still, we consider it a fair characterization of the MMCO and MMG global vegetation distributions. Grosso modo, the present reconstructions are characterized by *"cool mixed forest"* at high northern latitudes, predominantly *"warm mixed forest"* at middle latitudes, *"tropical broadleaf evergreen forest"* in the tropics, and *"tundra"* in the ice-free regions of Antarctica (Fig. 2.5.). Compared to PI, the vegetation of the Middle Miocene represents a warmer and wetter climate. In

the northern hemisphere high latitudes forests are warmer, with no forest tundra or tundra present. The mid-latitudes present warmer and wetter biomes, with e.g. less shrubland-type biomes. The tropics are wetter, with less savanna and less grasses. There is no evidence for neither a desert in northern Africa (Sahara) nor in central Asia. In the southern hemisphere high latitudes tundra is present at the MMCO and disappears after the Antarctic ice sheet expansion at the MMG (Pound et al., 2012; Bonan et al., 2002). For a higher degree of detail, in GCMs including a dynamic vegetation component, our Middle Miocene vegetation datasets could be used to initialize the vegetation model. Another valid approach would be using the output from an offline vegetation model as boundary condition (e.g., the ones described in Henrot et al., 2017), although here our aim was to provide vegetation boundary conditions based on paleobotanical data. A detailed discussion of the vegetation patterns we assigned to each region can be found in the Appendix B.

2.2.6. Testing the boundary conditions with CCSM3

To provide evidence of the suitability of our boundary conditions for global climate modeling, a small taste of CCSM3 results from the MMCO and MMG experiments, which employ those, and the PI experiment, as control run, is presented below.

Global mean precipitation rates are 3.00, 2.86, and 2.72 mm/day for the MMCO, MMG, and PI experiments, respectively. Some patterns distinguishing the Miocene runs from the PI run include lower precipitation rates during the Miocene along the northwest coast of South America (15° S–10° N) (up to 3–4 mm/day lower) (Figs. 2.6., 2.7.), although reaching further inland. In central Africa, between 20° S–5° N, the results show values also up to 3–4 mm/day lower than PI, which might be related to the reduced Miocene east African topography (Jung et al., 2016). An intensification of the precipitation occurs in the Indian Ocean, compared to PI, with the Intertropical Convergence Zone (ITCZ) reaching further north at ~ 90° E (Bay of Bengal). On the contrary, in the equatorial Pacific the PI run exhibits higher precipitation rates than the Miocene runs. These

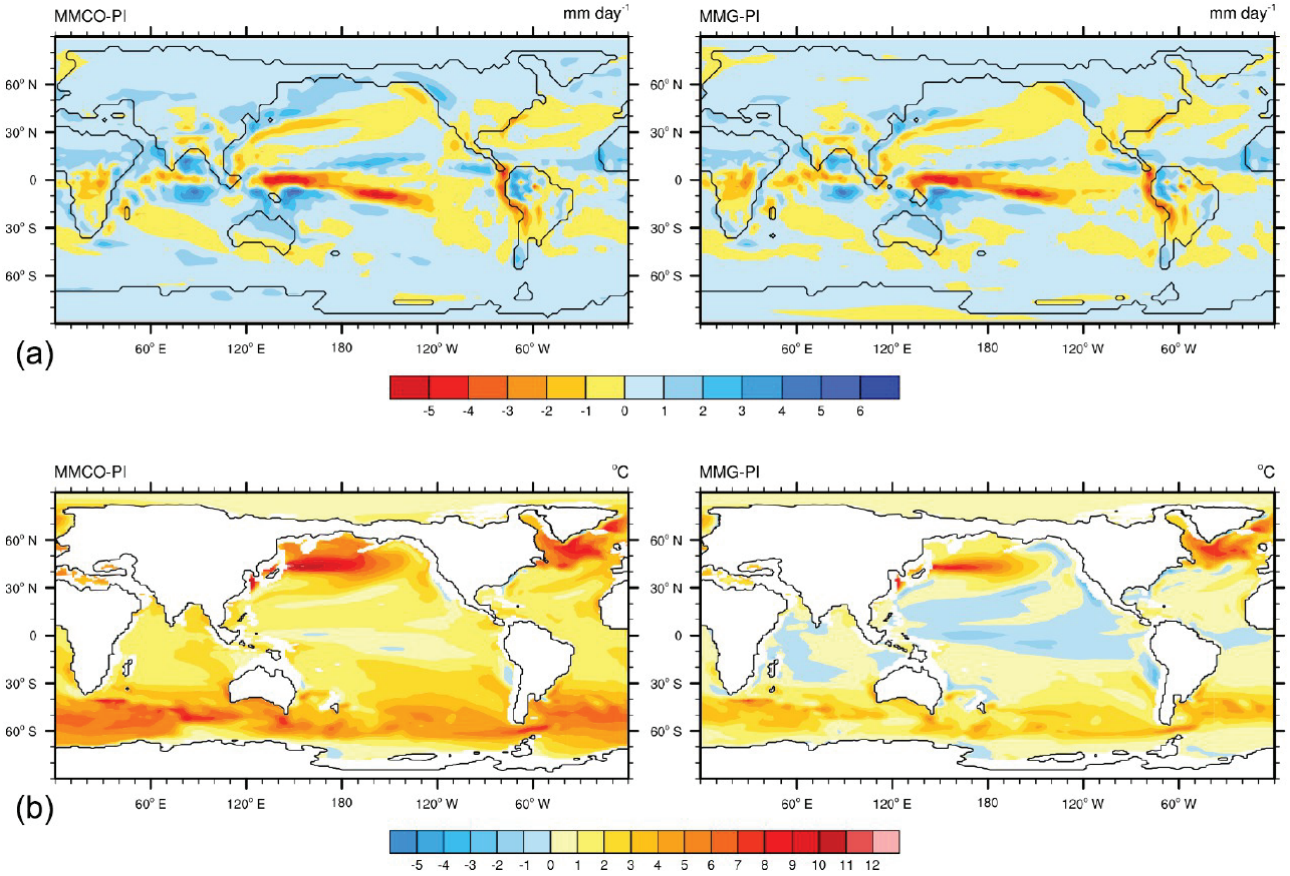

Figure 2.6. *Precipitation (mm day−1) (a) and sea surface temperature (°C) (b) differences between MMCO and MMG experiments, and PI, respectively.*

changes in the rainbelt patterns could be related to the different extent and distribution of ice sheets in both hemispheres. Other studies have already suggested that global ice sheets might have an effect on the ITCZ (Holbourn et al., 2010; Groeneveld et al., 2017). Other interesting patterns are the decrease in precipitation across the MMCT over the east African coast, between 0–20° N (0.5–2 mm/day lower), as well as the drying at high latitudes (0–1 mm/day). Regarding sea surface temperatures (SSTs) (Fig. 2.6.), the highest values correspond to the MMCO experiment, with a mean global SST of 19.62 °C, followed by the MMG experiment (18.04 °C) and the PI experiment (16.85 °C). When considering surface air temperatures (at 2 m height), our results show mean global values of 16.38 °C, 13.88 °C, and 12.16 °C for the MMCO, MMG, and PI, respectively (Fig. 2.8.). The modeled decrease in mean global surface air temperatures (2.5 °C) and SSTs (1.6 °C)

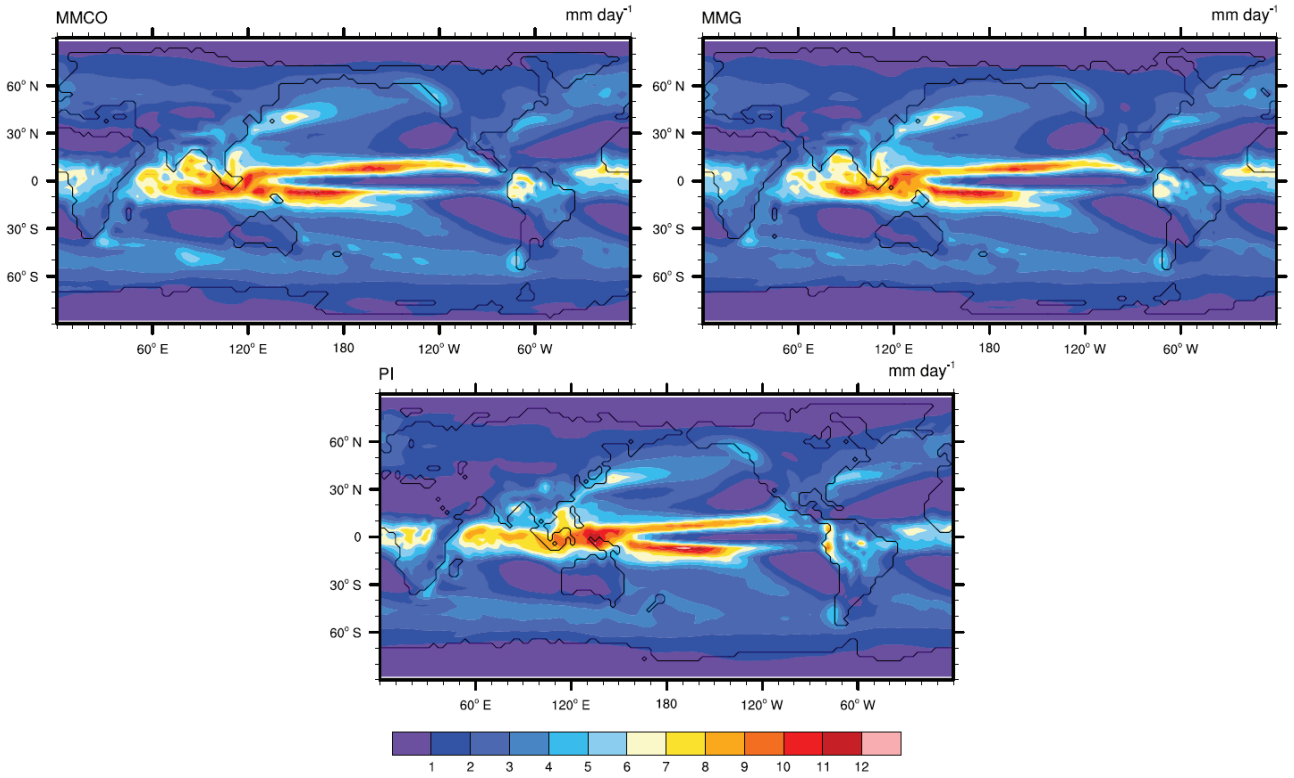

Figure 2.7. *Precipitation for MMCO, MMG, and PI, in mm day−1.*

between MMCO (CO_2 = 400 ppmv) and MMG (CO_2 = 200 ppmv) is in good agreement with the CCSM3 climate sensitivity values suggested in Kiehl et al. (2006). Our global mean surface air temperature and precipitation values support the idea of a Middle Miocene climate warmer and wetter than PI, and a cooling and drying trend across the MMCT. Knorr and Lohmann (2014) MMCT model results show a decrease of 3.1 °C in global mean surface air temperature across the MMCT, a value slightly higher than our 2.5 °C estimate. Although CO_2 is lower in the MMG simulation than in the control run, SSTs are higher for MMG than for PI. Potential causes for a MMG climate warmer than PI are the lower extent of ice sheets (the Antarctic ice sheet is smaller and the northern Hemisphere free of ice sheets in the MMG run), and the different vegetation cover (Knorr et al., 2011).

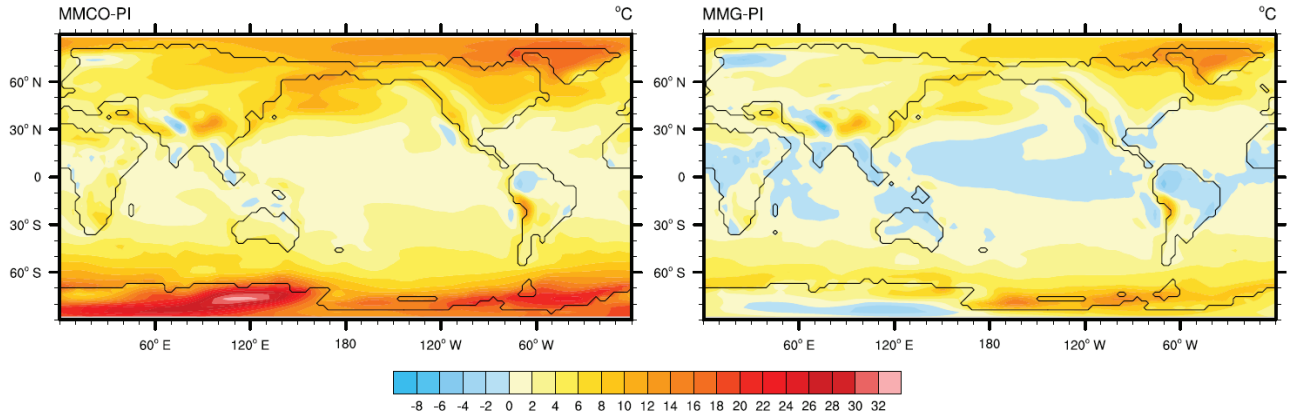

Figure 2.8. *Surface air temperature differences (at 2 m height) (in °C) between MMCO and MMG experiments, and PI, respectively.*

2.2.7. Data availability

All the MMCO and MMG boundary conditions described in this chapter can be found in NetCDF format at PANGAEA (https://doi.pangaea.de/10.1594/PANGAEA.888504). The MMCO and MMG global topography/bathymetry data are available from the 0.5°x0.5° lat/lon grid files mmco_topo_bathy_v1_0.nc and mmg_topo_bathy_v1_0.nc, respectively. The MMCO and MMG global vegetation data can be found in the 2°x2° lat/lon grid files mmco_veg_v1_0.nc and mmg_veg_v1_0.nc, respectively.

3. Modeling the Middle Miocene Climate Transition – a global approach

3.1. The ocean state during the Middle Miocene versus pre-industrial

Our experiments indicate a Middle Miocene climate warmer than PI. At the MMCO, for example, modeled global mean sea surface temperatures (SSTs) are 2.77 °C warmer than at PI (Fig. 3.1.). The areas showing the strongest anomalies compared to PI are the northern North Pacific, where the MMCO experiment shows SSTs > 5 °C warmer than PI; the North Atlantic, with MMCO SSTs > 4 °C warmer than PI; and a global belt below 40° S, with MMCO SSTs > 3 °C warmer than PI (Fig. 3.1.). Middle Miocene global mean ocean temperatures at depth are warmer than PI as well: 2.72 °C warmer at 2000–2250 m for MMCO (Fig. 3.2.).

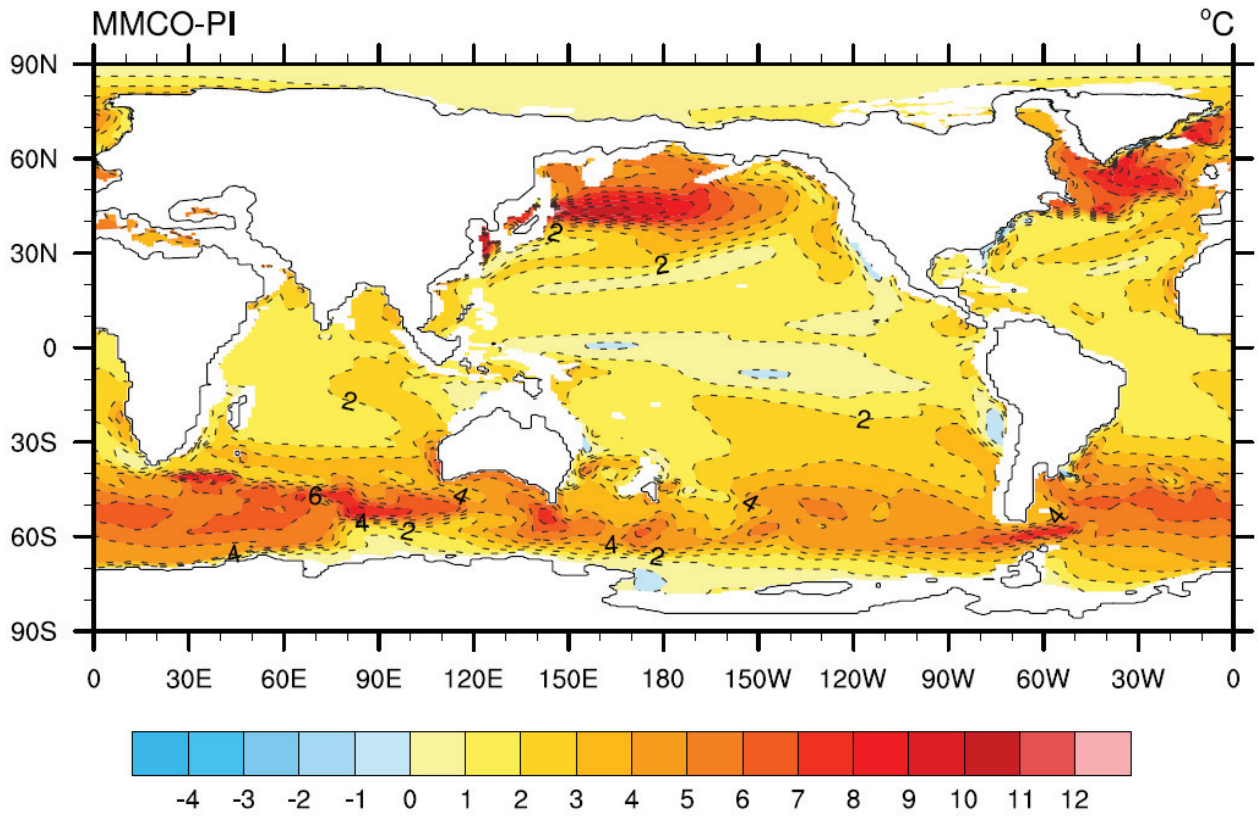

Figure 3.1. *Sea surface temperature differences between MMCO and PI, in °C.*

An outstanding result in the Middle Miocene experiments is the weaker Antarctic Circumpolar Current (ACC) compared to PI (Fig. 3.3.). At the Drake Passage, for example, the intensity of the ACC is of ~ 130 Sv for the MMCO versus ~ 190 Sv for PI. Another remarkable feature is the stronger deeper cell and the weaker upper cell of the MOC in the Middle Miocene experiments, compared to PI (Fig. 3.4.). Besides, the Middle Miocene experiments exhibit increased southward ocean heat transport in the Southern Hemisphere (up to 0.7 PW more at ~ 12° S for MMCO, Fig. 3.5.) and decreased northward ocean heat transport in the Northern Hemisphere (up to 0.35 PW less at ~ 15° N for MMCO, Fig. 3.5.).

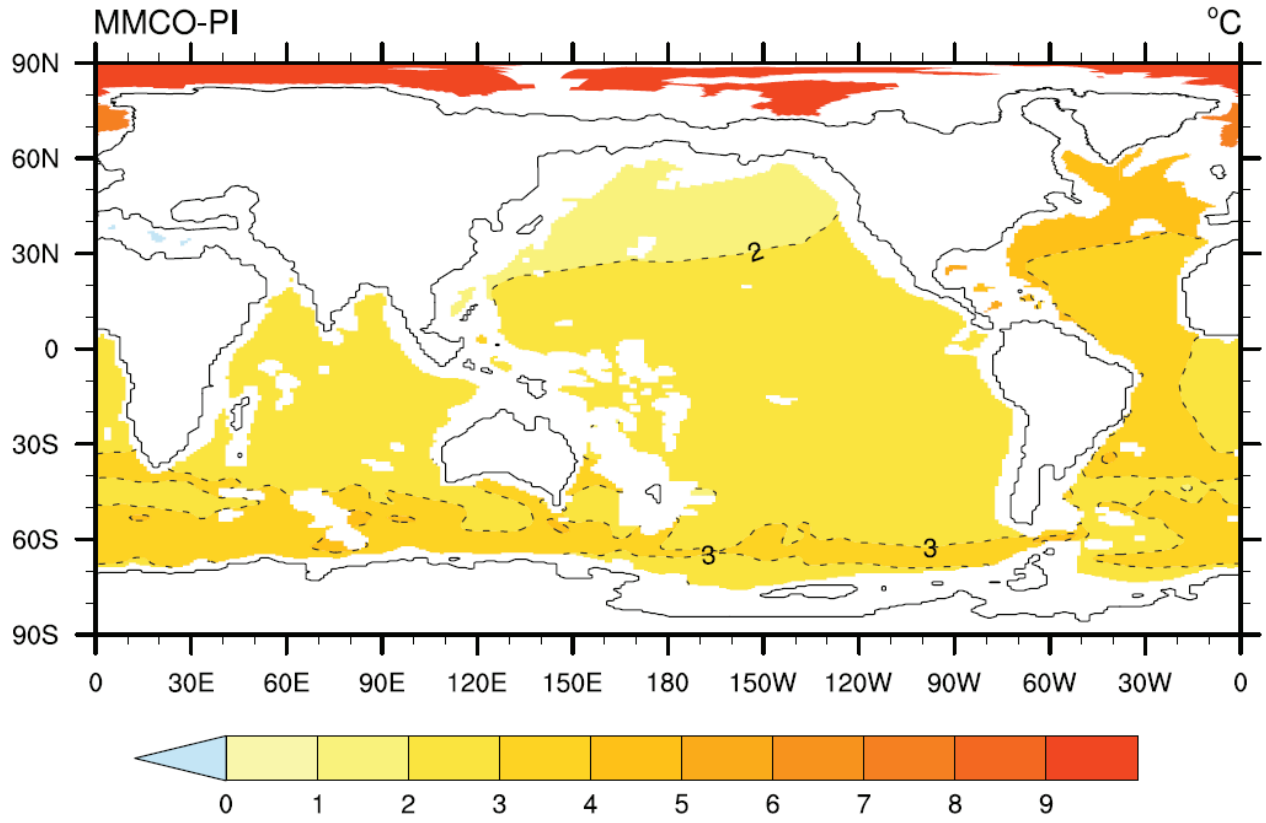

Figure 3.2. *Ocean temperature differences at 2000–2250 m depth between MMCO and PI, in °C.*

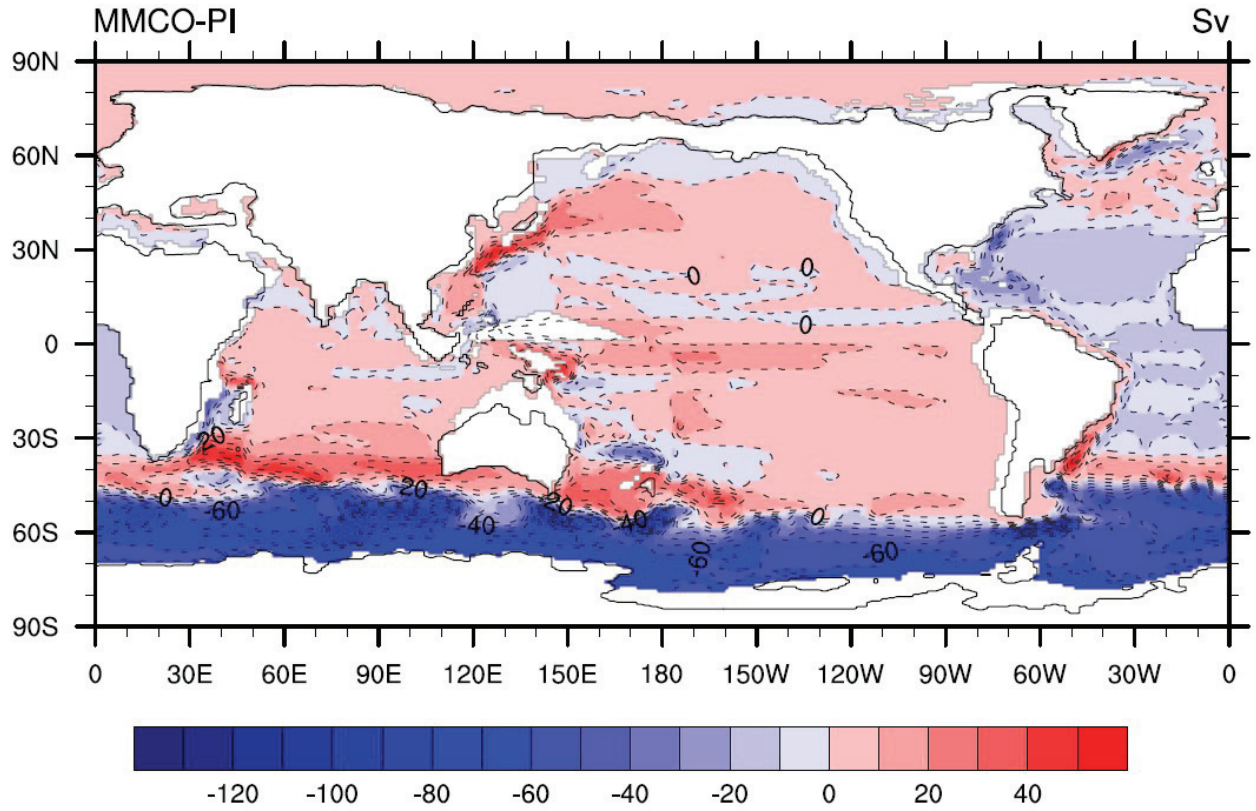

Figure 3.3. *Barotropic stream function differences between MMCO and PI, in Sv.*

3.2. Ocean changes during the Middle Miocene Climate Transition

3.2.1. Changes in sea surface temperatures

Mean global SSTs decrease from 19.62 °C during the MMCO to 18.04 °C during the MMG. The regions showing the most pronounced cooling are the northern North Pacific (between ~ 2–5 °C of cooling) and some areas of the Southern Ocean (up to ~ 5 °C of cooling) (Fig. 3.6.). Note that although cooling is the dominant tendency across the MMCT, slight warming occurs in some very restricted areas (e.g., close to the Antarctic coast at ~ 165° W).

The effect of the atmospheric CO_2 decrease on SSTs can be analyzed by comparing the experiments MMCO200 vs MMCO (non-expanded ice sheet) and MMG vs MMG400 (expanded ice sheet) (Fig.

3.6.). A significant decrease in mean global SSTs is observed in both cases: of 1.95 °C with a non-expanded ice sheet, and of 1.9 °C with an expanded ice sheet. Again, cooling is most pronounced in the Southern Ocean and in the northern North Pacific.

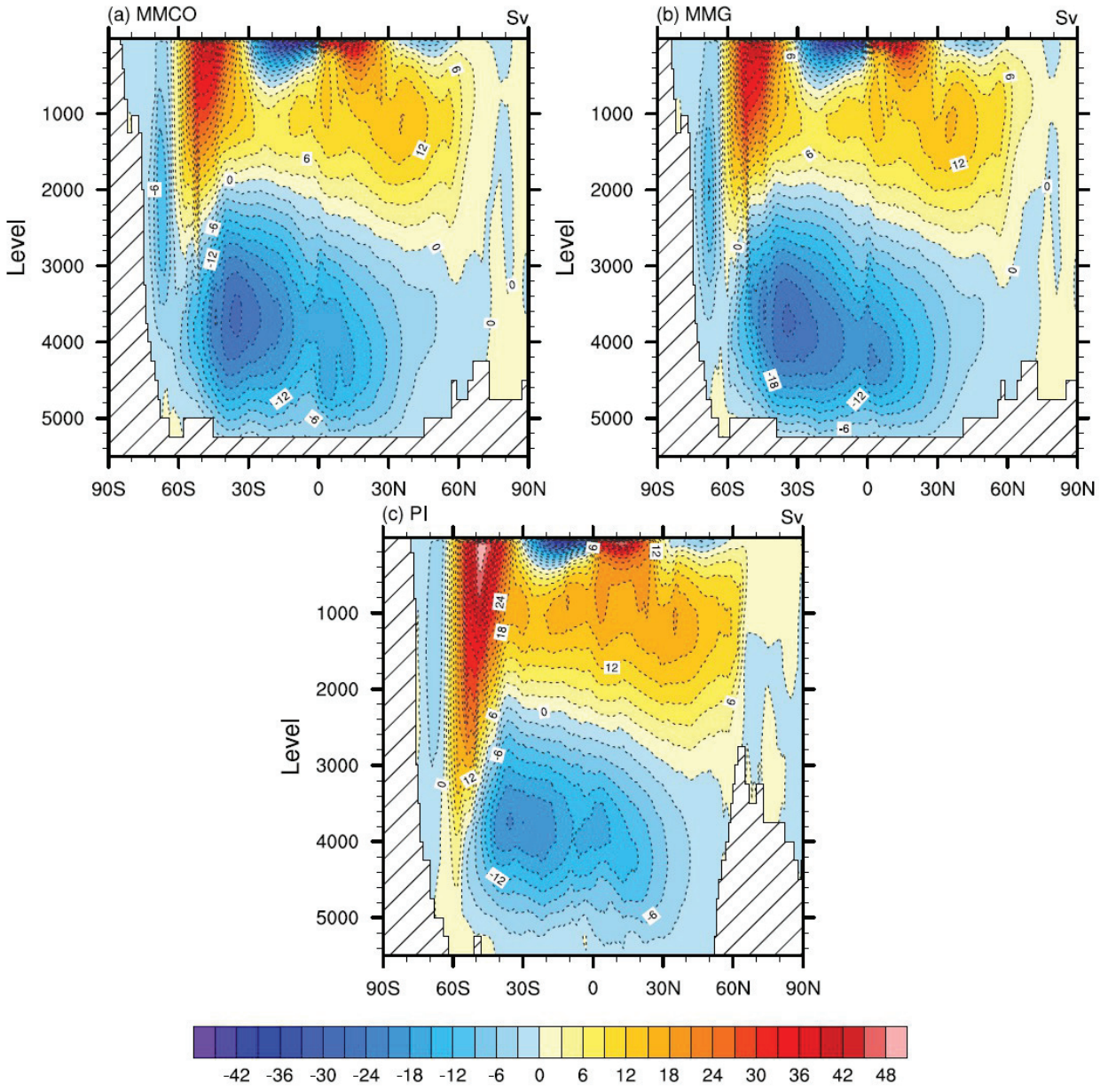

Figure 3.4. *Global Meridional Overturning Circulation (Eulerian component): a) MMCO, b) MMG, and c) PI, in Sv.*

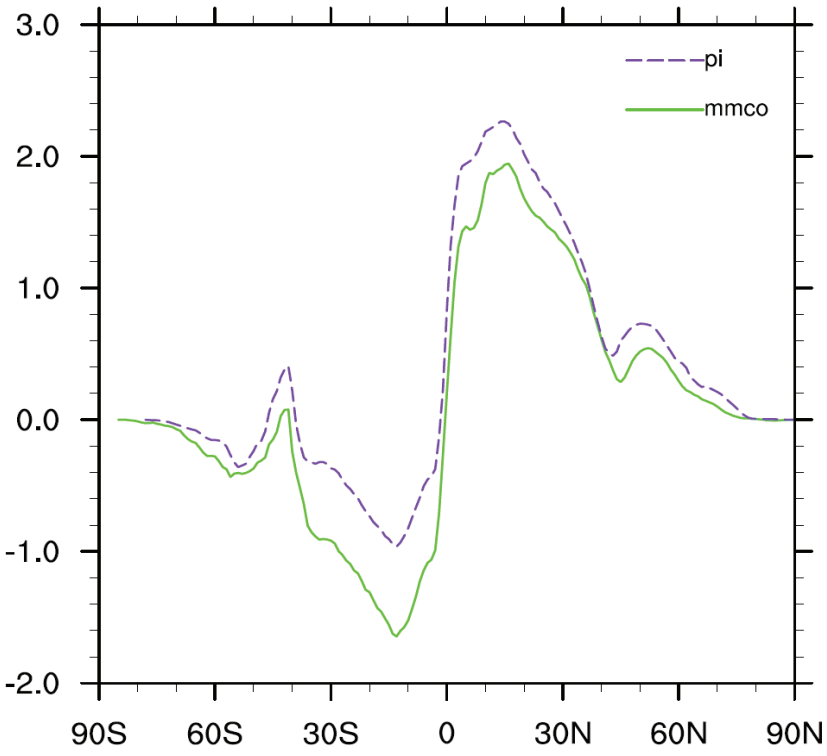

Figure 3.5. *Global meridional ocean heat transport for MMCO and PI, in PW.*

By comparing the experiments MMG400 vs MMCO (CO_2 = 400 ppmv) and MMG vs MMCO200 (CO_2 = 200 ppmv) (Fig. 3.6.), the effect of the Antarctic ice sheet expansion is assessed. In both cases slight increases in mean global SSTs are observed: of 0.32 °C with CO_2 fixed at 400 ppmv, and of 0.37 °C with CO_2 fixed at 200 ppmv. Warming is particularly pronounced in some regions of the Southern Ocean, with increases in temperature by up to 3–4 °C. Although warming is the dominant trend, localized cooling patterns are detected in the simulations, e.g. in the Southern ocean at ~ 90° E and in the North West Pacific ~ 40–50° N (with values reaching up to 3–4 °C of cooling). Globally, the effects of CO_2 and Antarctic ice sheet on SSTs are opposite in sign and the effects of the first clearly dominate those of the second.

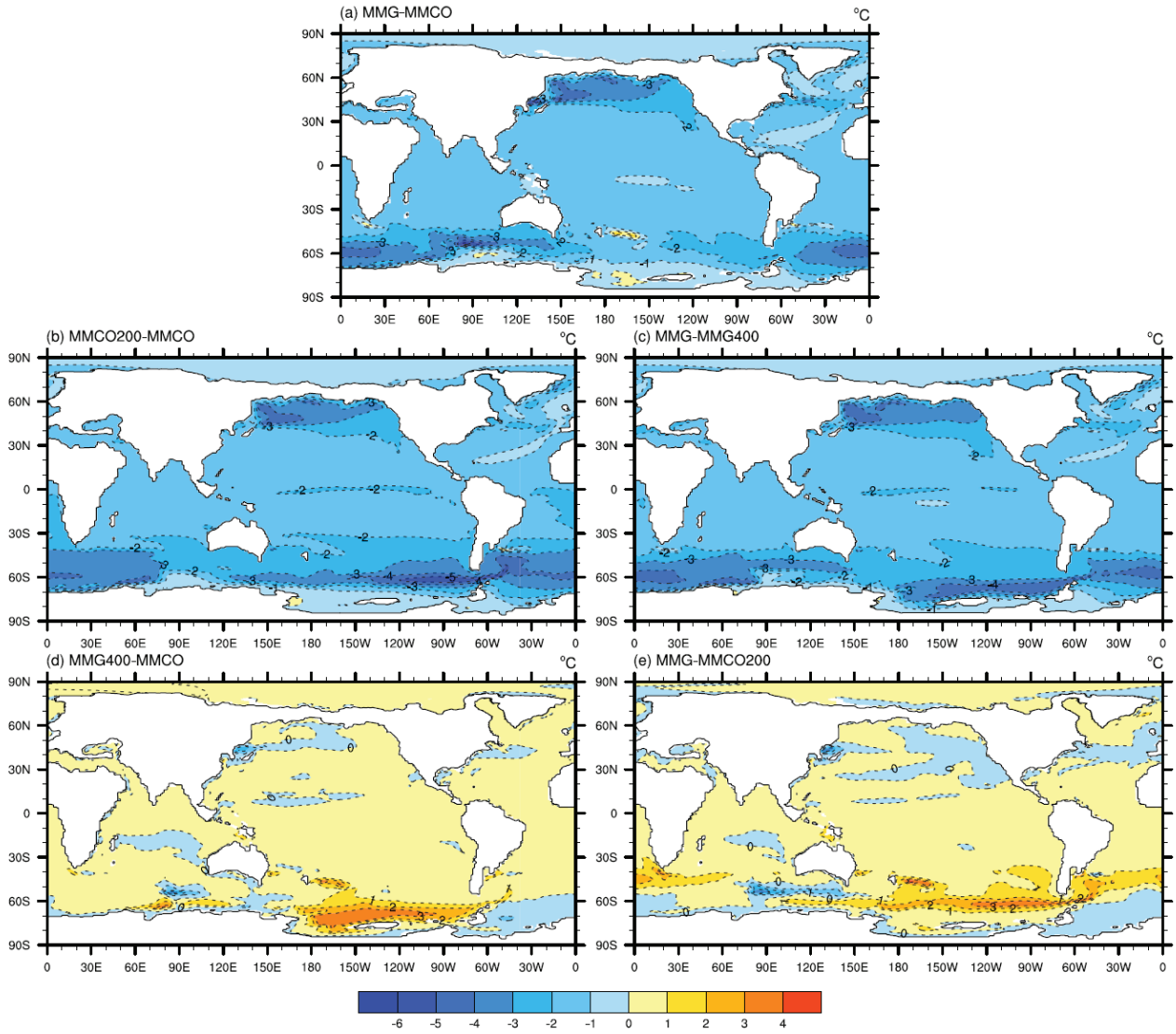

Figure 3.6. *Sea surface temperature differences: a) MMG-MMCO (MMCT), b) MMCO200-MMCO and c) MMG-MMG400 (CO_2 effect), and d) MMG400-MMCO and e) MMG-MMCO200 (ice sheet effect), in °C.*

3.2.2. Changes in ocean temperatures at depth

Waters cool down across the MMCT at almost all depths and latitudes. The only exceptions occur near the ocean surface above ~ 70° N and between 800–1000 m depth at ~ 80° S (warming by less than 0.5 °C) (Fig. 3.7.). In most regions, ocean temperatures decrease between 1.5–2 °C, and cooling, in general, is stronger above 2500 m depth (Fig. 3.7.).

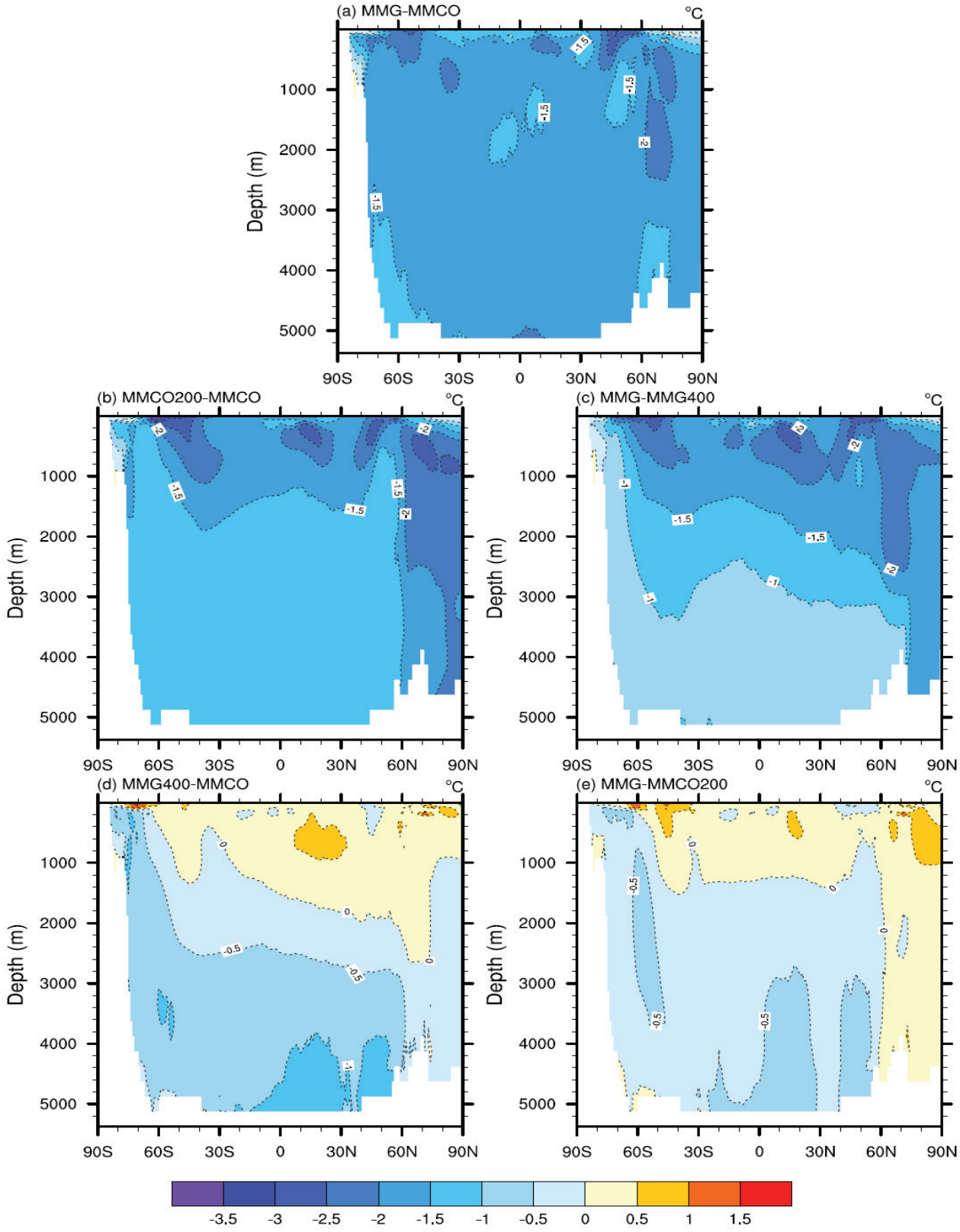

Figure 3.7. *Global zonally averaged temperature differences: a) MMG-MMCO (MMCT), b) MMCO200-MMCO and c) MMG-MMG400 (CO_2 effect), and d) MMG400-MMCO and e) MMG-MMCO200 (ice sheet effect), in °C.*

The CO_2 decrease causes significant cooling of waters at almost all depths and latitudes. The cooling effect is significantly weaker at the lower cell of the MOC, compared to the upper cell (Fig. 3.7.). The Antarctic ice sheet expansion effect on ocean temperatures is not uniform and varies significantly with depth (Fig. 3.7.). Cooling dominates below ~ 1400 m depth, while warming occurs above 1400 m depth (and also at deeper levels in the Arctic, for the MMG-MMCO200 case). Figure 3.7. suggests that the Antarctic ice sheet expansion would cool down waters close to the surface at high southern latitudes and that these waters would spread to lower latitudes through the lower cell of the MOC. Both the CO_2 decrease and the Antarctic ice sheet expansion contribute locally to cooling of waters across the MMCT and the CO_2 decrease is the major driver of the cooling.

In order to identify the areas where upper ocean cooling is transmitted to the deep ocean, temperature changes at 2000–2250 m depth are plotted (Fig. 3.8.). At that depth, mean temperatures decrease from 3.64 °C during the MMCO to 2.03 °C during the MMG. The strongest cooling is simulated in an area of the Southern Ocean between ~ 80–160° E, where temperatures decrease by 2.5–3° C (see sect. 3.2.3. below), and in the North Atlantic (see sect. 3.2.4. below), where temperatures decrease up to 2–2.5 °C (Fig. 3.8.). Figures 3.7. and 3.8. indicate that the cooling of deep waters in the Southern Ocean is caused both by the CO_2 decrease and the Antarctic ice sheet expansion. On the contrary, cooling in the North Atlantic at 2000–2250 m depth is caused by the CO_2 decrease (Fig. 3.8.).

3.2.3. Cooling of deep waters at southern high latitudes

Significant cooling of deep waters occurs in the Southern Ocean across the transition (1.5–2 °C) (Fig. 3.7.) which, as mentioned above, is linked to both the CO_2 and the Antarctic ice sheet forcings. The geometry of the isotherms (Fig. 3.9.) suggests that cooling originates close to or at the ocean

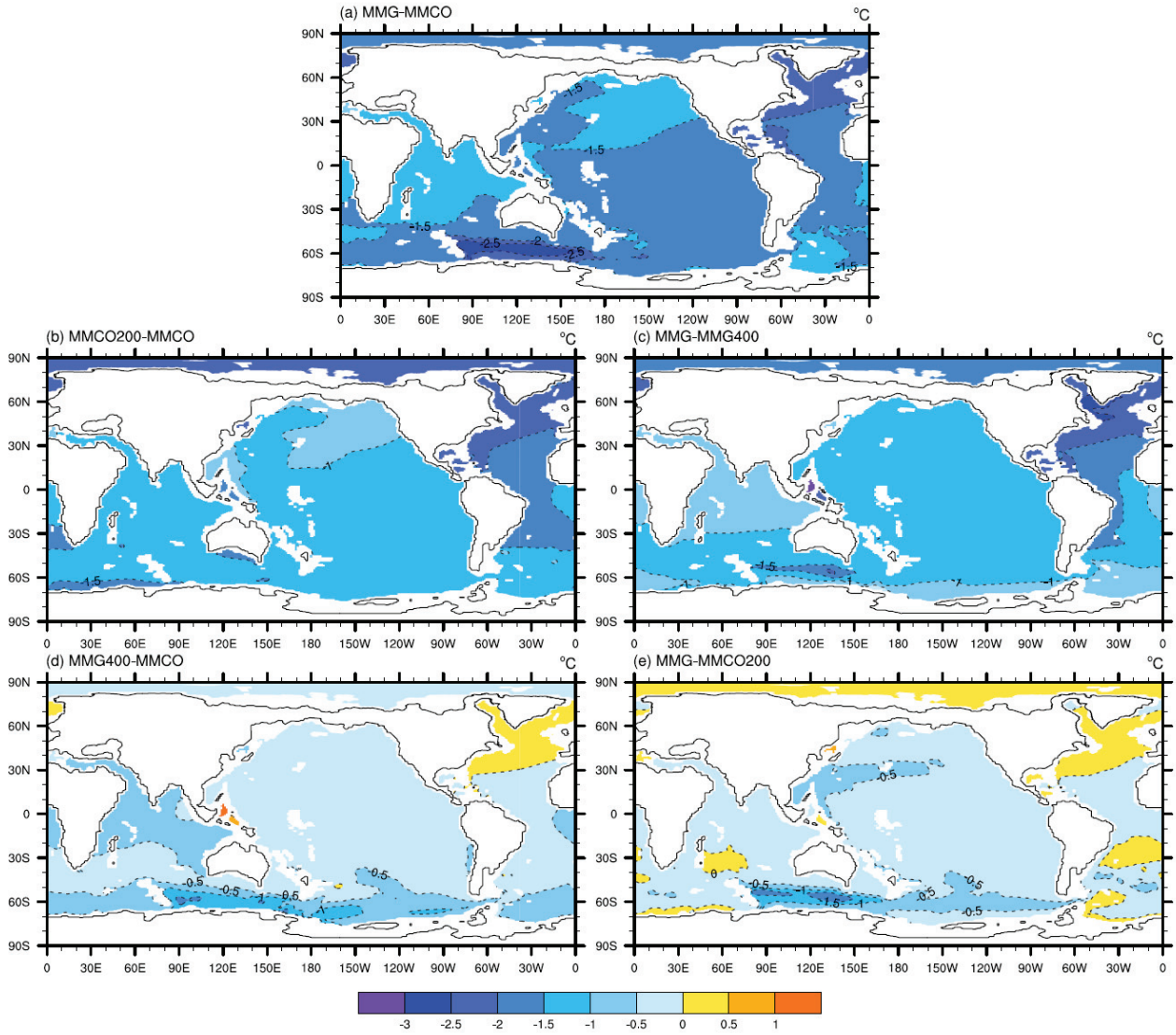

Figure 3.8. *Ocean temperature differences at 2000–2250 m depth: a) MMG-MMCO (MMCT), b MMCO200-MMCO and c) MMG-MMG400 (CO_2 effect), and d) MMG400-MMCO and e) MMG-MMCO200 (ice sheet effect), in °C.*

surface in the surroundings of Antarctica and spreads to the bottom through water convection. Evidence of water convection in the Southern Ocean at the MMCO and MMG can be derived from the steep isopycnals below ~ 60° S in the potential density field (Fig. 3.10.). Furthermore, the MOC field shows evidence of Antarctic Bottom Water (AABW) formation both at the MMCO and MMG (Fig. 3.4.). The austral winter mixed layer could potentially provide evidence of water convection as well, although convection occurring directly at the Antarctic continental shelf could be masked in

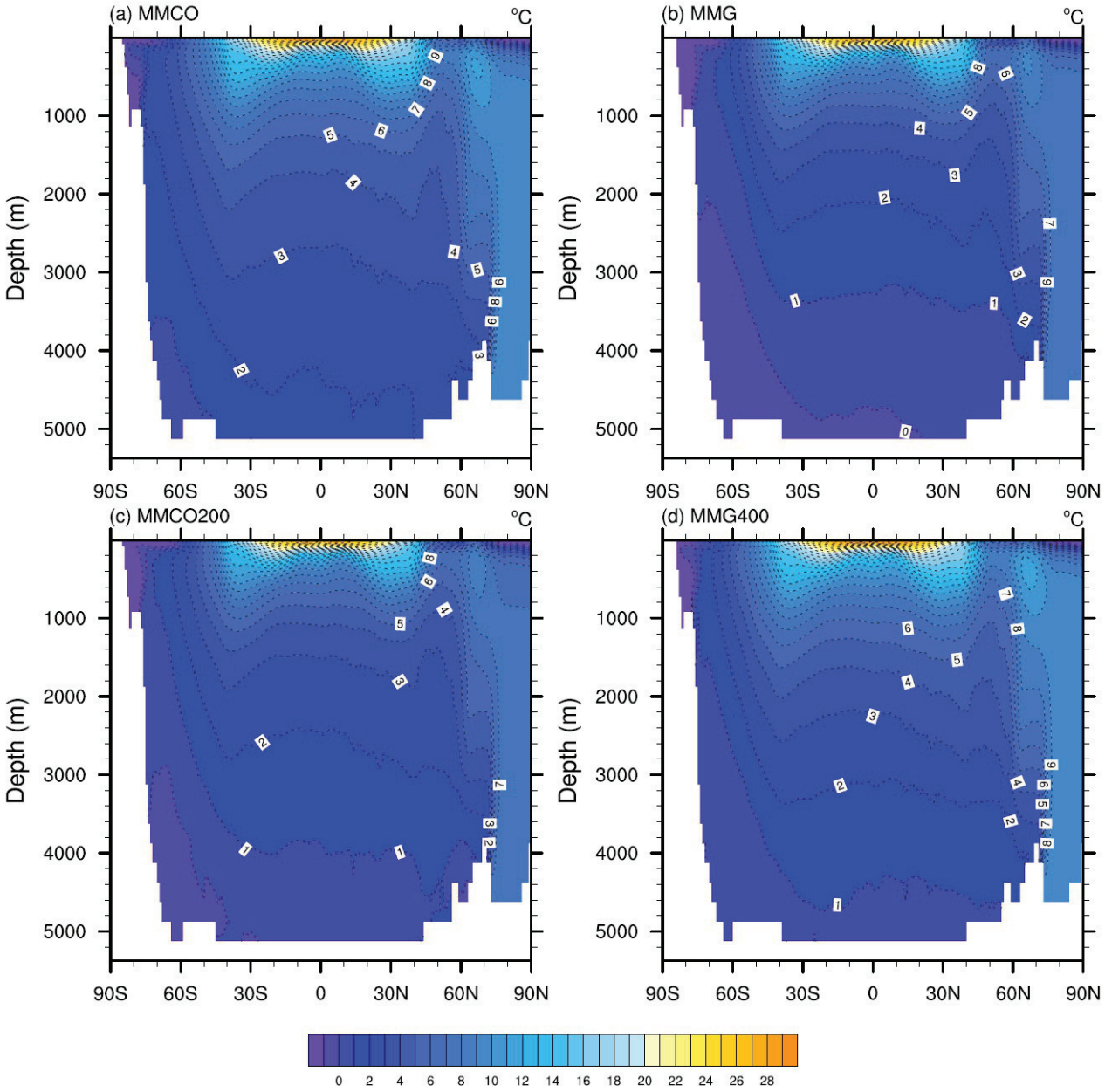

Figure 3.9. *Global zonally averaged temperature: a) MMCO, b) MMG, c) MMCO200, and d) MMG400, in °C.*

that field. During the MMCO, the austral winter mixed layer shows a convection area at the East Antarctic coast, between ~ 0–80° E, with mean depths down to 1800–1900 m (Fig. 3.11.). During the MMG, the austral winter mixed layer shows moderate convection at ~ 60° S between 90–120° E, with mean depths only down to 600–700 m (Fig. 3.11.).

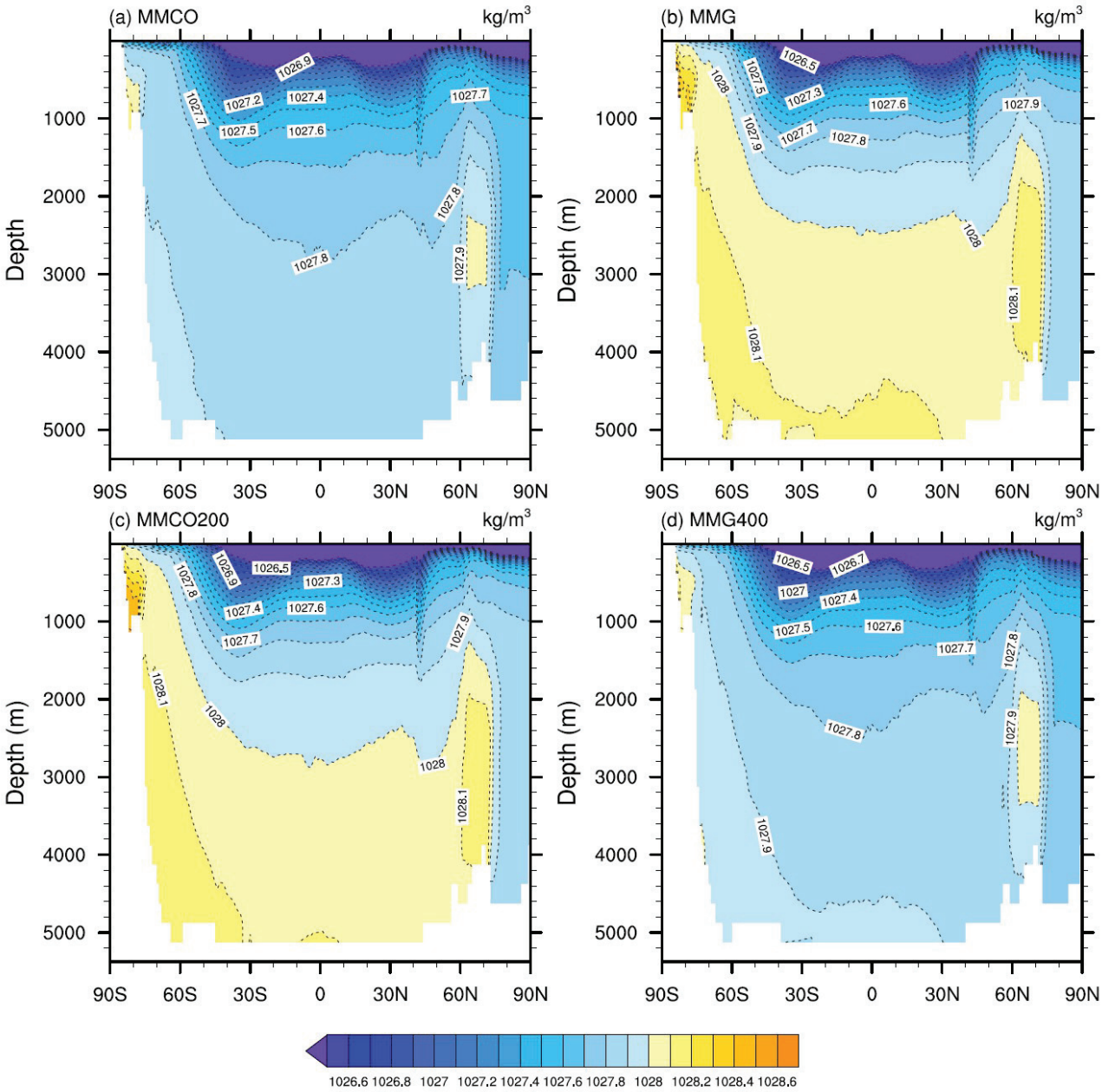

Figure 3.10. *Global zonally averaged potential density: a) MMCO, b) MMG, c) MMCO200, and d) MMG400, in kg/m³.*

The larger increase in potential density of the waters attached to and at the bottom of the Antarctic shelf (0.2–0.25 kg/m^3 increase) compared to the waters surrounding them (0.15–0.2 kg/m^3 increase) (Fig. 3.12.) suggests an increase in AABW formation across the MMCT, which would be related to the CO_2 forcing (Fig. 3.12.). Figure 3.13. suggests that the increase in AABW formation is related to a salinity increase triggered by the CO_2 dropdown. The increase in salinity is caused by freshwater

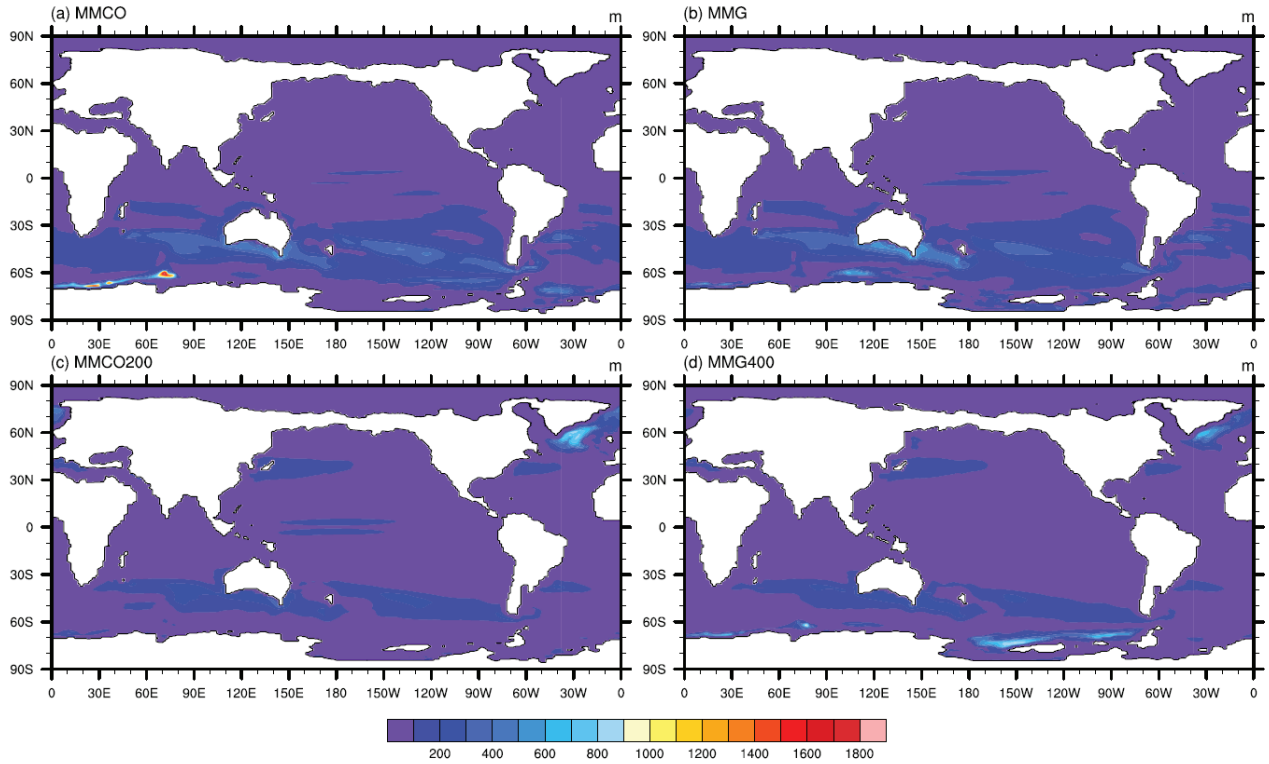

Figure 3.11. *Austral winter mean mixed layer depth: a) MMCO, b) MMG, c) MMCO200, and d) MMG400, in m.*

flux anomalies linked to sea ice formation and to variations in the evaporation/precipitation balance around Antarctica (Figs. 3.14., 3.15.).

The MOC field, though, does not show uniform strengthening of its deeper cell across the MMCT (Fig. 3.16.). Strengthening of the deep cell of the MOC occurs below ~ 70° S (2–3 Sv), as well as between 0–30° S, below ~ 3400 m (up to 7–8 Sv). Weakening also occurs, for example between 55–65° S, below ~ 2000 m (up to 4–5 Sv). However, only the Eulerian component of the MOC was considered in this study (the eddy-induced component was not available), which might have an effect on the results.

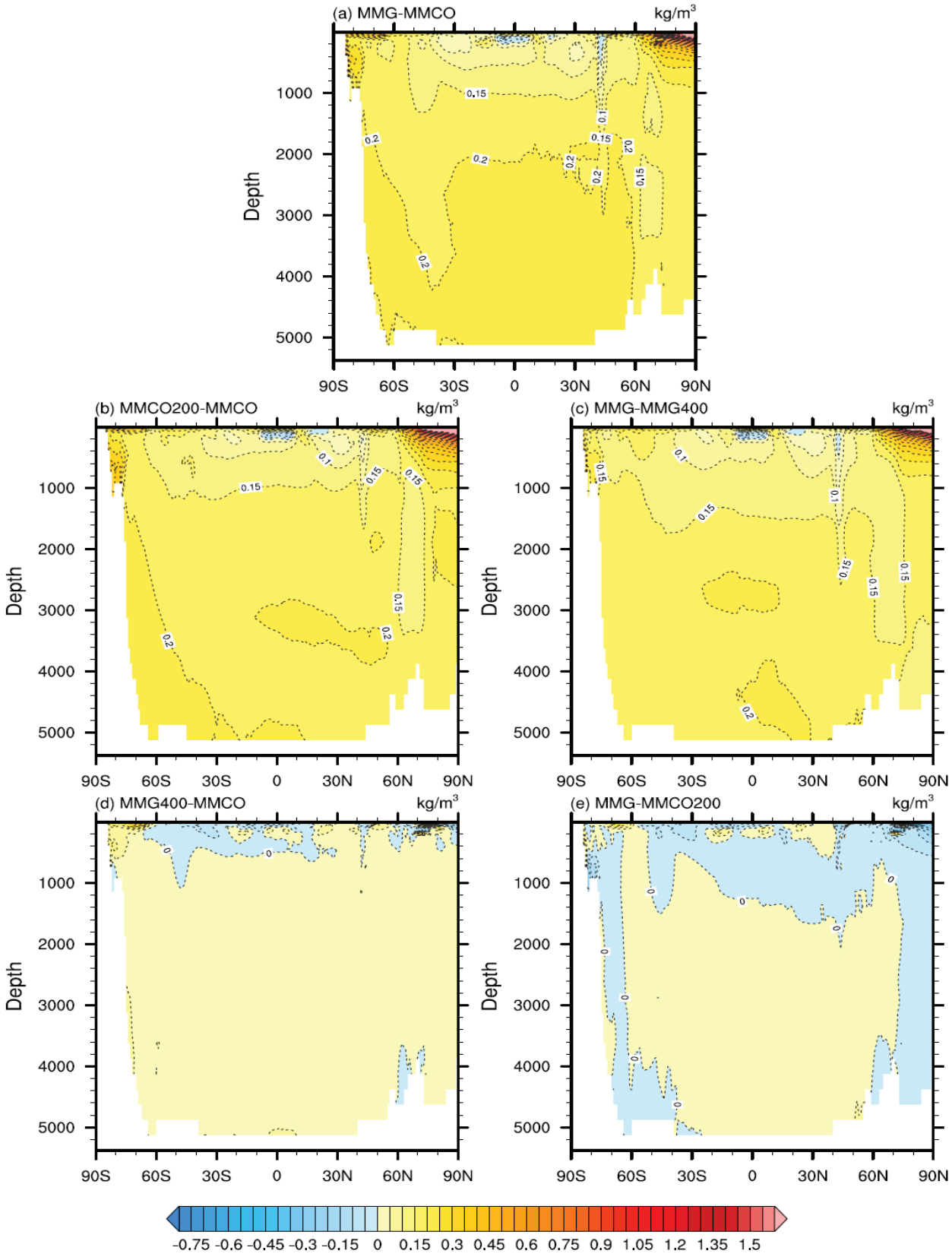

Figure 3.12. *Global zonally averaged potential density differences: a) MMG-MMCO (MMCT), b) MMCO200-MMCO and c) MMG-MMG400 (CO_2 effect), and d) MMG400-MMCO and e) MMG-MMCO200 (ice sheet effect), in kg/m^3.*

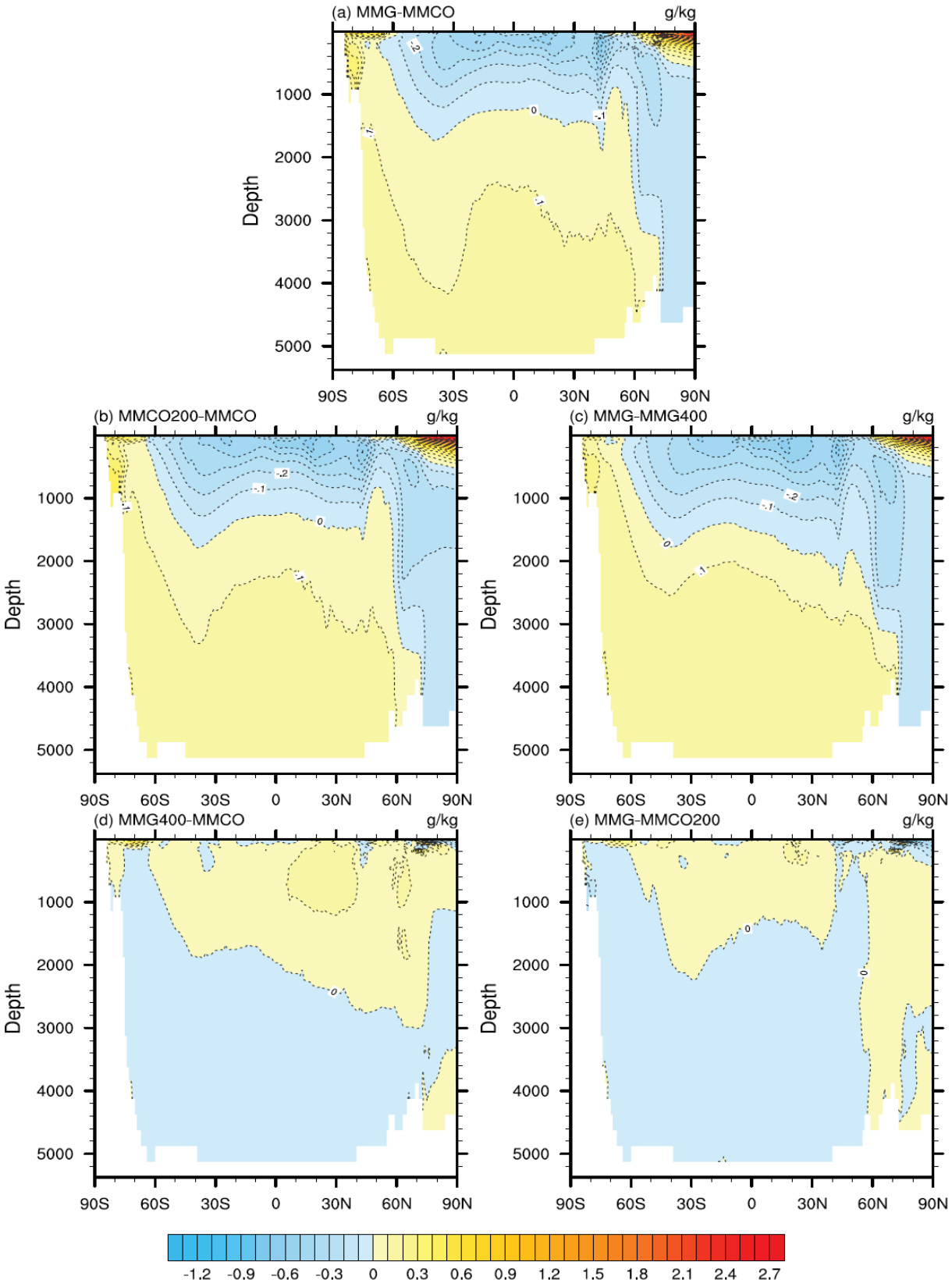

Figure 3.13. *Global zonally averaged salinity differences: a) MMG-MMCO (MMCT), b) MMCO200-MMCO and c) MMG-MMG400 (CO_2 effect), and d) MMG400-MMCO and e) MMG-MMCO200 (ice sheet effect), in g/kg.*

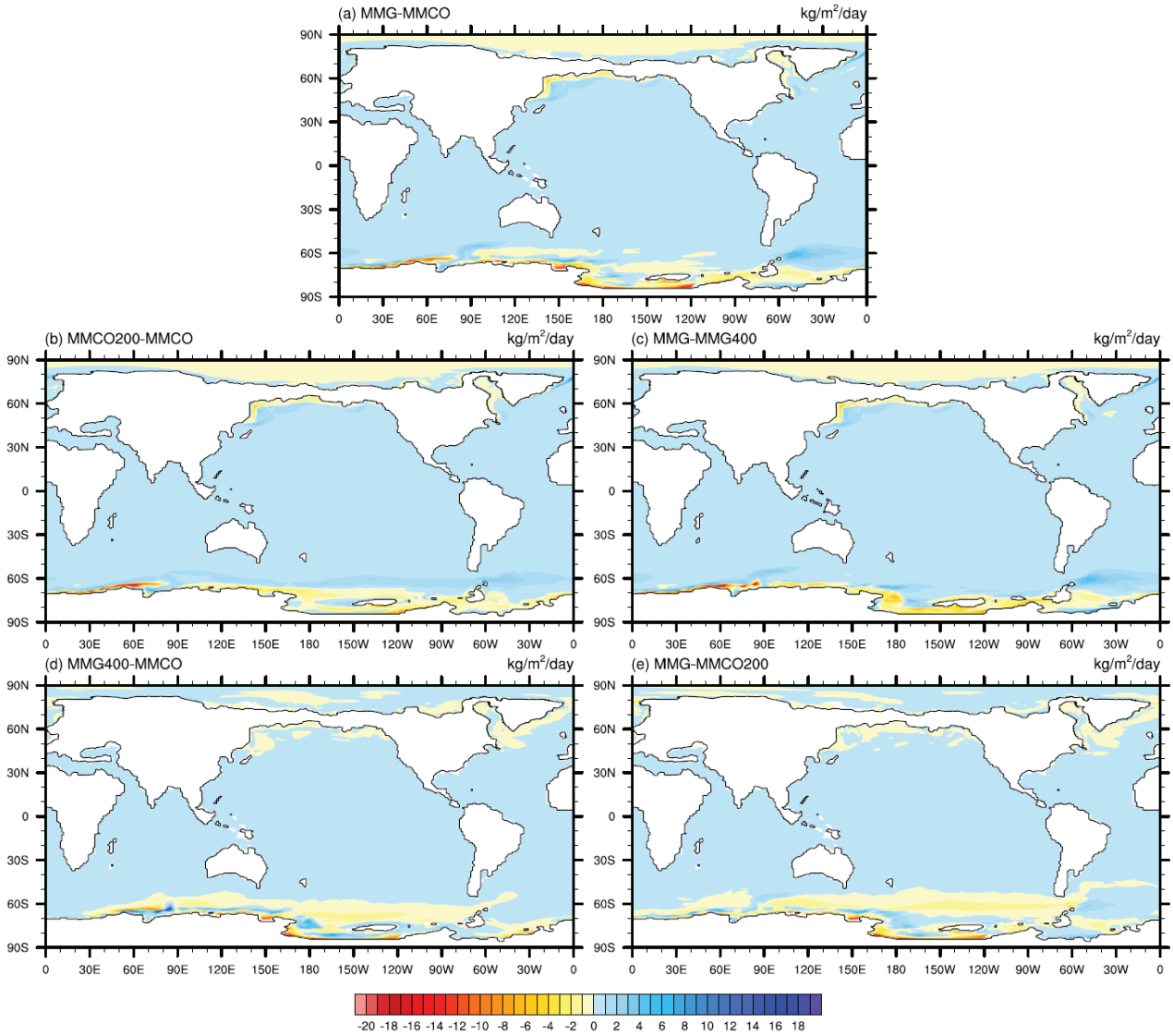

Figure 3.14. *Freshwater flux differences (related to sea ice formation): a) MMG-MMCO (MMCT), b) MMCO200-MMCO and c) MMG-MMG400 (CO_2 effect), and d) MMG400-MMCO and e) MMG-MMCO200 (ice sheet effect), in kg of freshwater/m^2/day. Positive values indicate an increase in freshwater into the ocean. Note: the field plotted is MELT_F + conversion factor * SALT_F, where MELT_F and SALT_F are CCSM3 ocean model variables.*

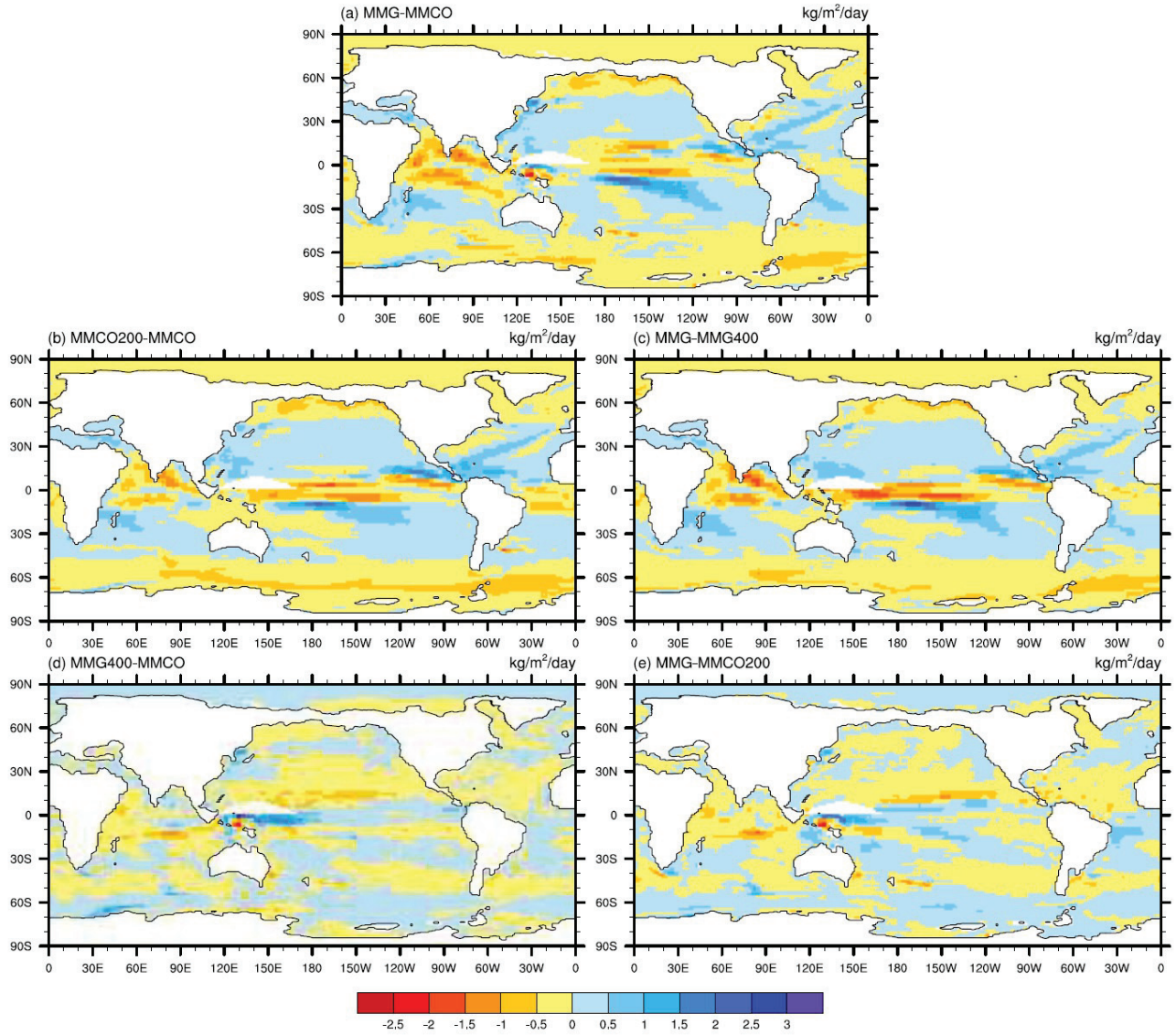

Figure 3.15. *Freshwater flux differences (from precipitation and evaporation): a) MMG-MMCO (MMCT), b) MMCO200-MMCO and c) MMG-MMG400 (CO_2 effect), and d) MMG400-MMCO and e) MMG-MMCO200 (ice sheet effect), in kg of freshwater/m^2/day.*

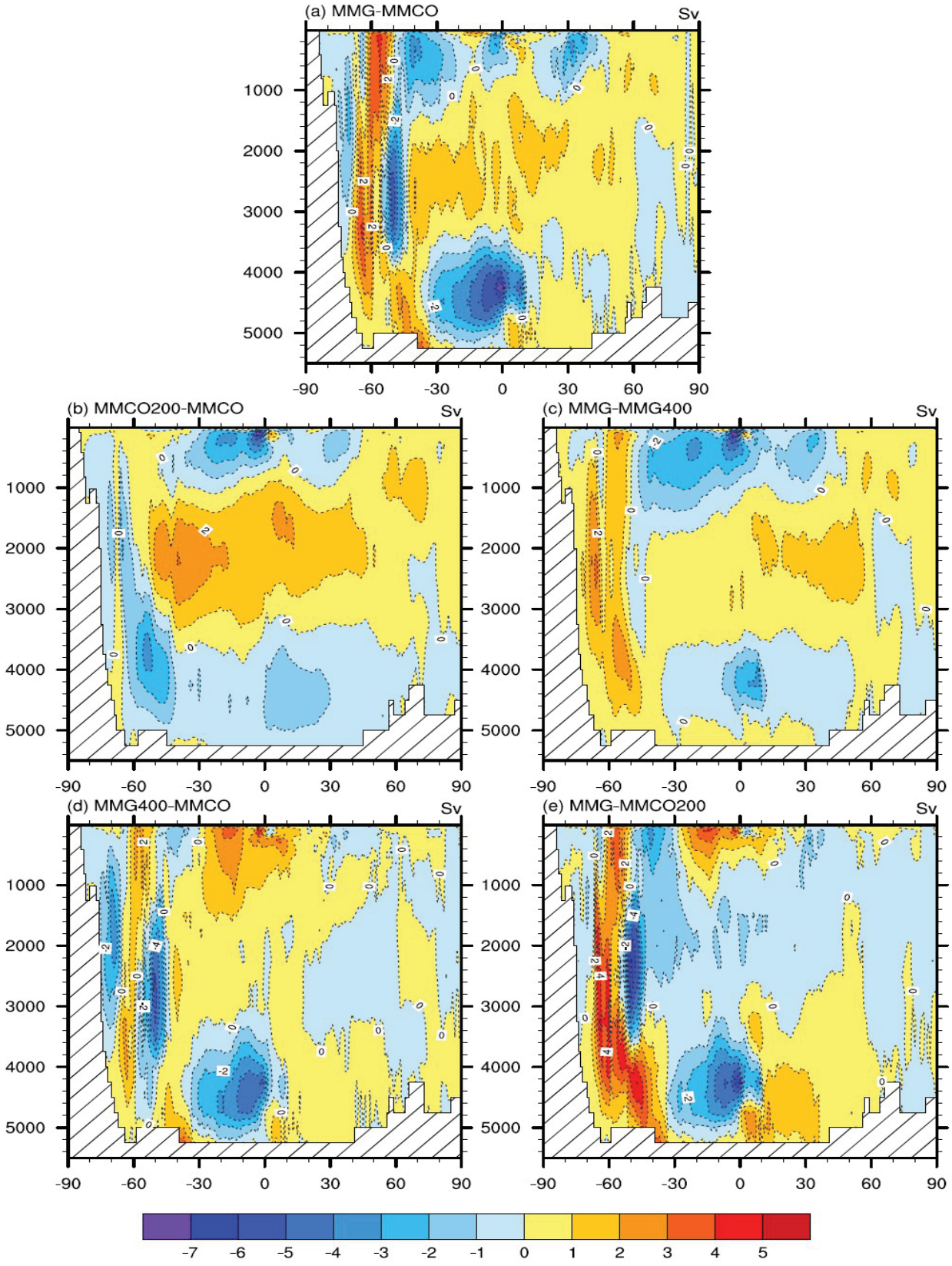

Figure 3.16. *Global Meridional Overturning Circulation differences (Eulerian component): a) MMG-MMCO (MMCT), b) MMCO200-MMCO and c) MMG-MMG400 (CO_2 effect), and d) MMG400-MMCO and e) MMG-MMCO200 (ice sheet effect), in Sv.*

3.2.4. Cooling of deep waters in the North Atlantic

In this section we take a closer look into the already mentioned cooling of deep waters in the North Atlantic, which is linked to the CO_2 decrease across the MMCT (Figs. 3.8., 3.17.). This cooling is caused by water convection in the North Atlantic, at ~ 50–60° N (Figs. 3.18., 3.19.). Convection occurs both during the MMCO and the MMG. During the MMCO, the mean boreal winter mixed layer reaches depths down to ~ 1600 m. During the MMG, the water convection region has expanded notably, and the mean mixed layer depth reaches values of up to ~ 1770 m (Fig. 3.19.). This increase in water convection is consistent with the upper cell of the MOC showing moderate strengthening across the MMCT at those latitudes (Figs. 3.4., 3.16.). The mixed layer, MOC, and potential density fields (Figs. 3.4., 3.16., 3.19., 3.20.) indicate that the increase in convection is linked to the CO_2 decrease across the transition.

The convection of waters in the North Atlantic during the Middle Miocene is caused by the high salinity of the North Atlantic waters, with values of 35.9–36 g/kg and 35.7–35.8 g/kg at 60° N at ~ 500 m depth for the MMCO and MMG, respectively (Fig. 3.21.), and by the relatively cold upper ocean temperatures in that region (Fig. 3.22.) .

The increase in convection in the North Atlantic across the MMCT is due to a decrease in the upper ocean temperatures (Fig. 3.17.) caused by the CO_2 dropdown. At ~ 171 m depth, e.g., between 50–60° N, temperatures decrease in the order of 2.5–3 °C (Fig. 3.23.). This increase in convection is not related to salinity changes. Salinity is reduced in the convection area across the MMCT (Fig. 3.24.).

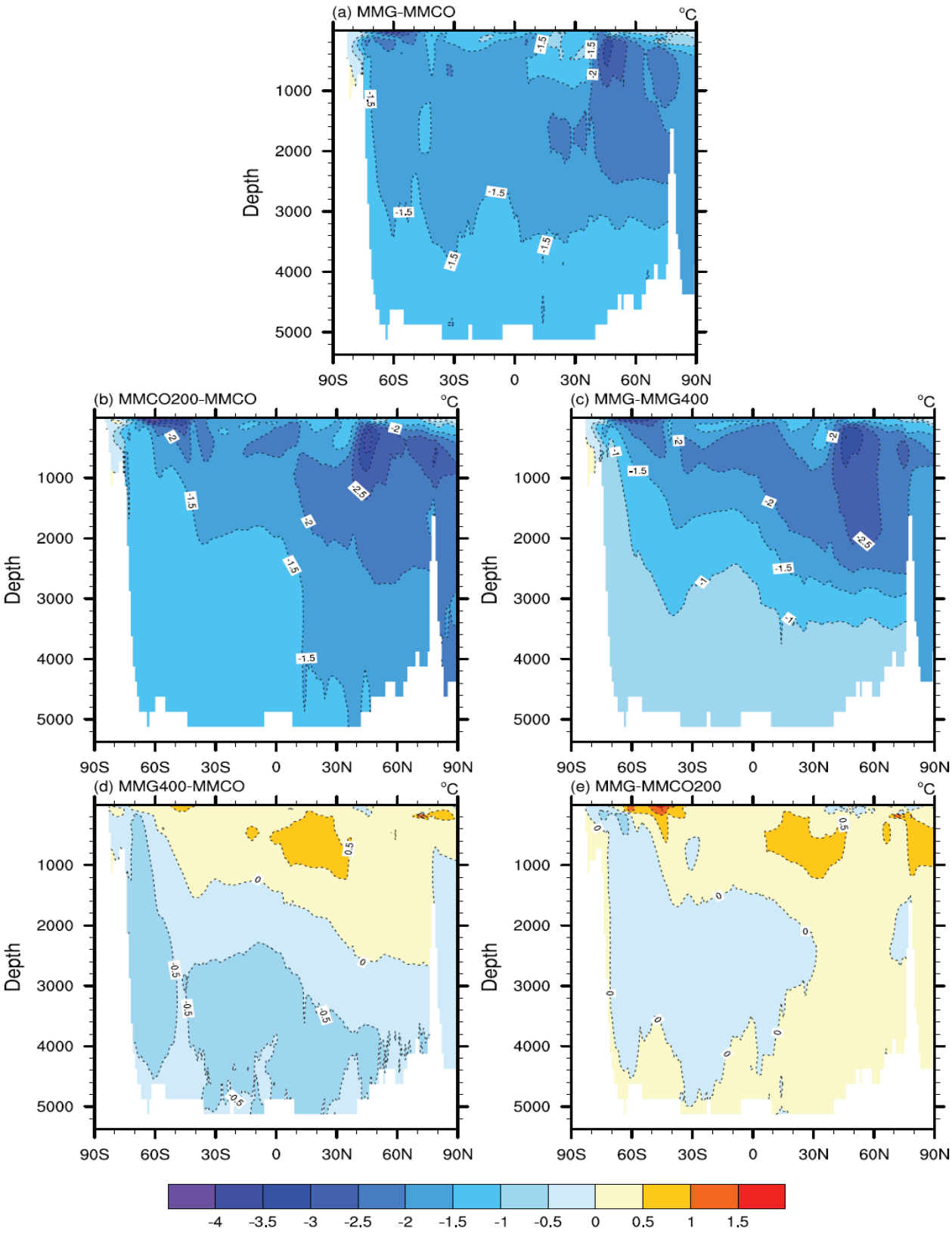

Figure 3.17. *Zonally averaged temperature differences for the Atlantic ocean: a) MMG-MMCO (MMCT), b) MMCO200-MMCO and c) MMG-MMG400 (CO_2 effect), and d) MMG400-MMCO and e) MMG-MMCO200 (ice sheet effect), in °C.*

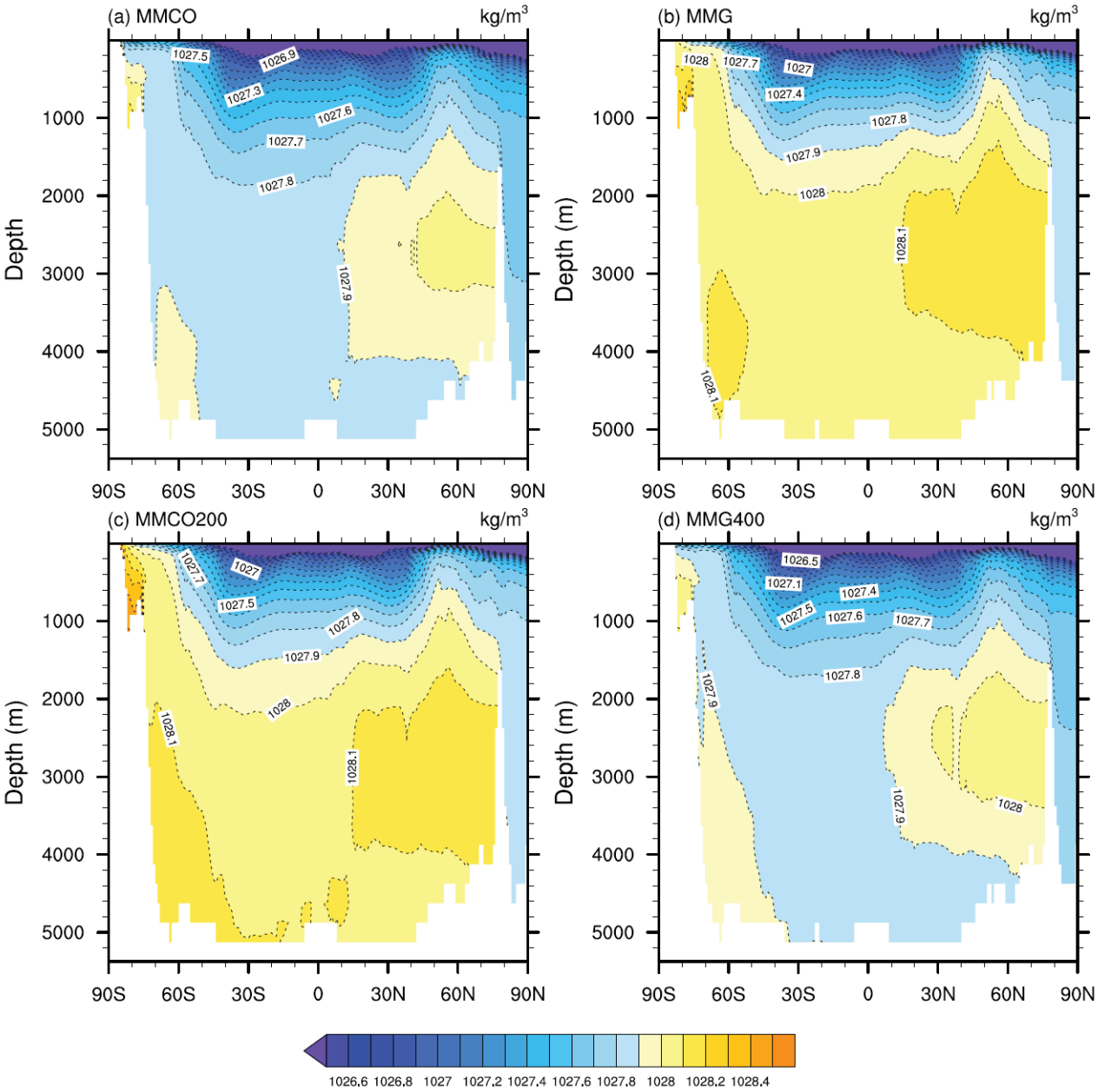

Figure 3.18. *Zonally averaged potential density for the Atlantic: a) MMCO, b) MMG, c) MMCO200, and d) MMG400, in kg/m³.*

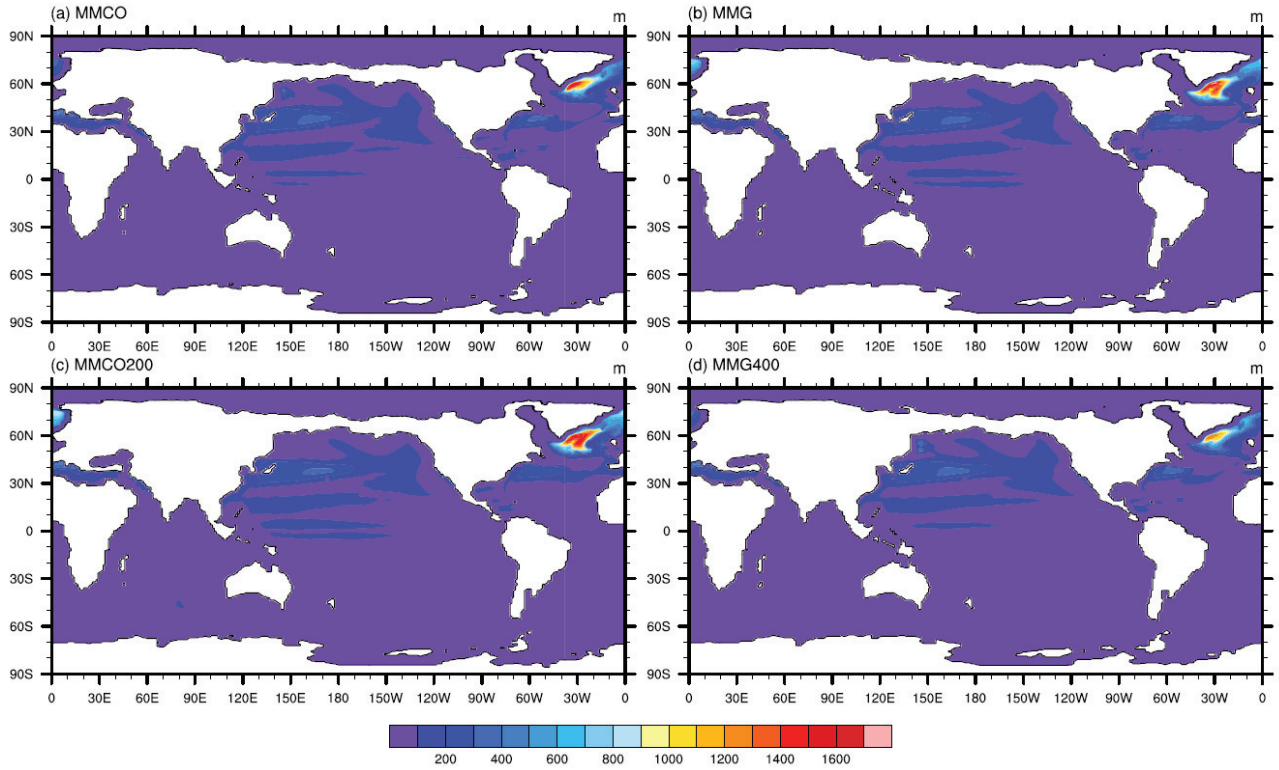

Figure 3.19. *Boreal winter mean mixed layer depth: a) MMCO, b) MMG, c) MMCO200, and d) MMG400, in m.*

3.3. Changes in near-surface winds in the Southern Hemisphere across the MMCT

Important changes in the pattern of near-surface winds occur in the Southern Hemisphere below ~ 50° S (Fig. 3.25.) across the MMCT. Strengthening of near-surface winds is the dominant tendency, although localized weakening is also detected in the simulations. Strengthening of the easterlies is observed along the Antarctic coast, with increases in wind speed of up to 8–9 m/s. Moderate strengthening of the westerlies occurs at a global belt around 50–60° S, with increases of up to 2–3 m/s. In contrast, on East Antarctica, between 20° and 120° E, at ~ 80° S, weakening of near-surface winds occurs, with decreases of up to 6–7 m/s.

The sensitivity analysis reveals that the changes in the near-surface wind patterns occurred on the Antarctic continent and the Southern Ocean across the MMCT are caused by the expansion of the

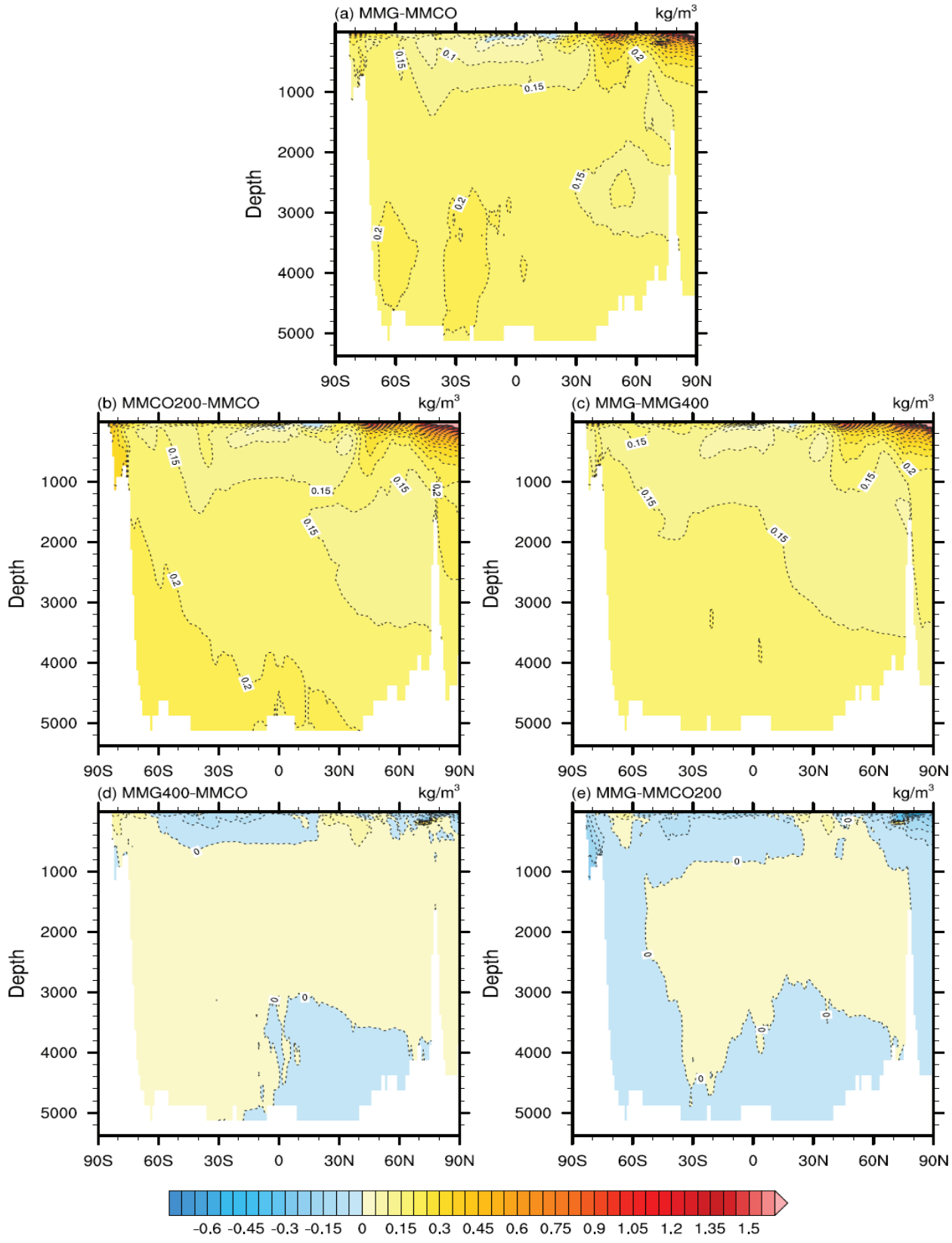

Figure 3.20. *Zonally averaged potential density differences for the Atlantic: a) MMG-MMCO (MMCT), b) MMCO200-MMCO and c) MMG-MMG400 (CO_2 effect), and d) MMG400-MMCO and e) MMG-MMCO200 (ice sheet effect), in kg/m³.*

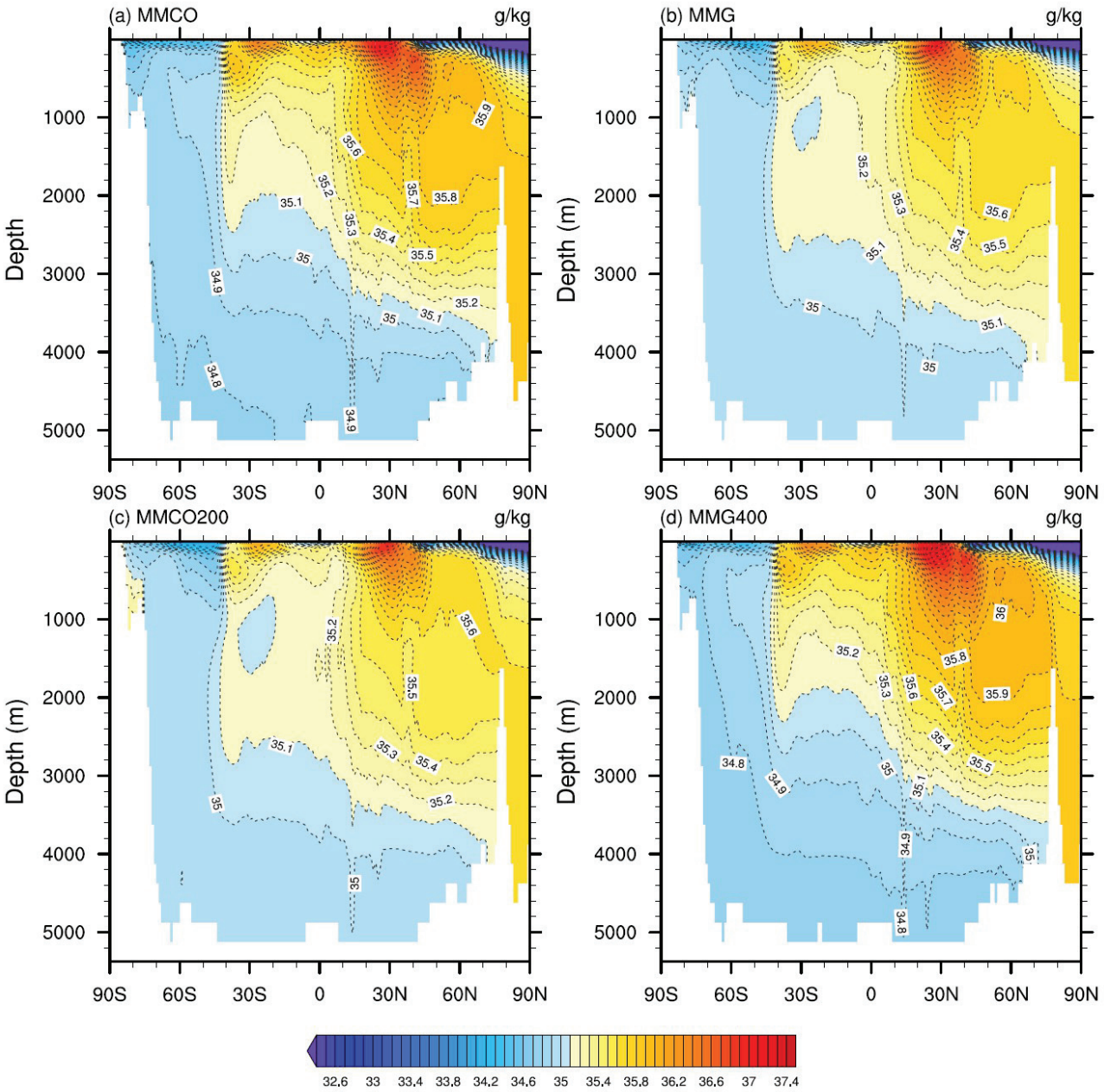

Figure 3.21. *Zonally averaged salinity for the Atlantic: a) MMCO, b) MMG, c) MMCO200, and d) MMG400, in g/kg. Note: temperatures are averaged over the longitude interval 100° W to 10° E.*

Antarctic ice sheet (Fig. 3.25.), which triggers variations in the pressure field around Antarctica. The sea level pressure gradient between the polar highs and subpolar lows increases across the MMCT: from a gradient of 24–30 hPa for MMCO to a gradient of 27–33 hPa for MMG (Fig. 3.26.), causing strengthening of the easterlies. Besides, the sea level pressure gradient between the

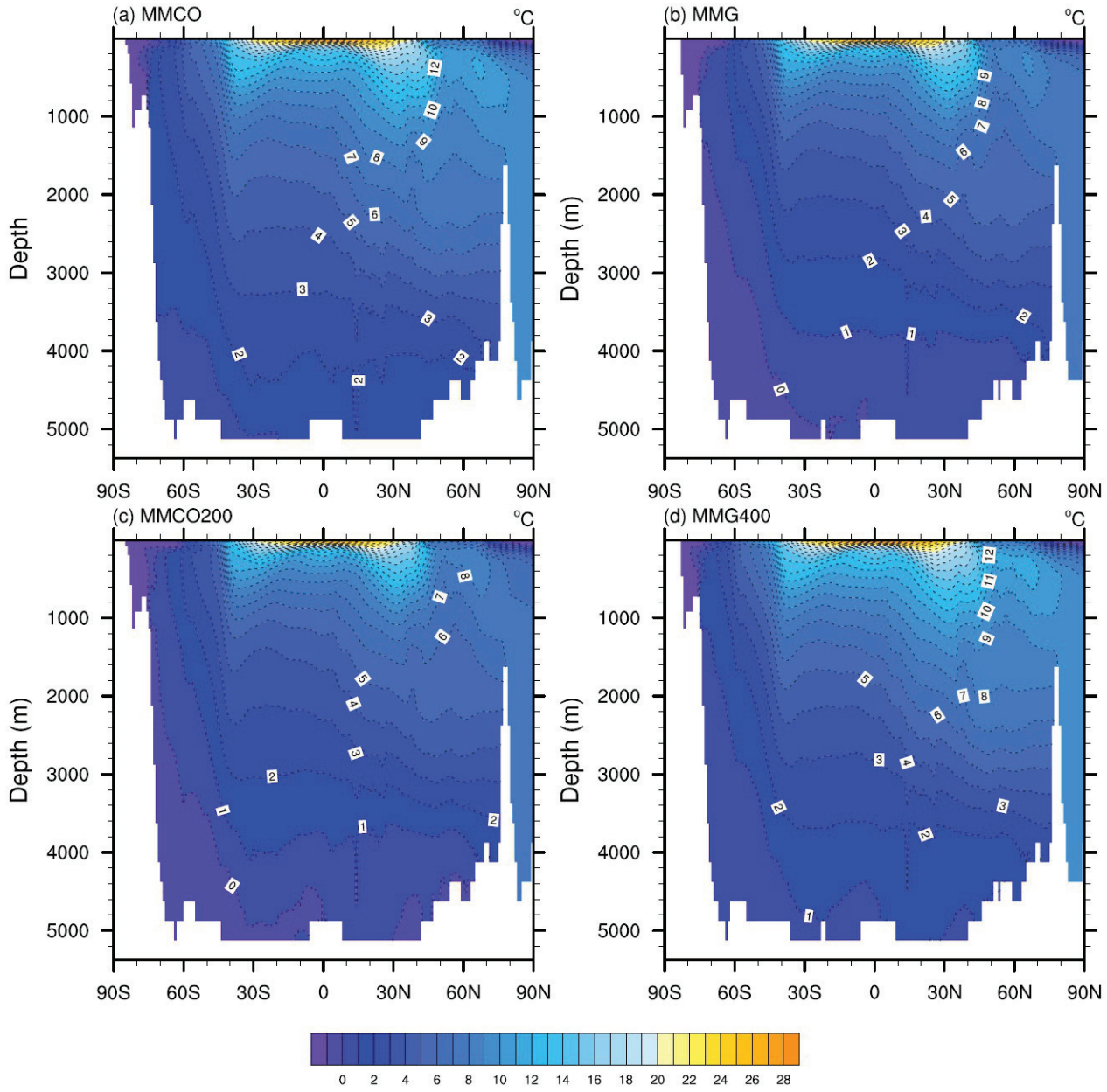

Figure 3.22. *Zonally averaged temperature for the Atlantic: a) MMCO, b) MMG, c) MMCO200, and d) MMG400, in °C.*

subpolar lows and subtropical highs increases across the MMCT: from 39–45 hPa for MMCO to 42–48 hPa for MMG. This increase translates into strengthening of the Southern Hemisphere westerlies.

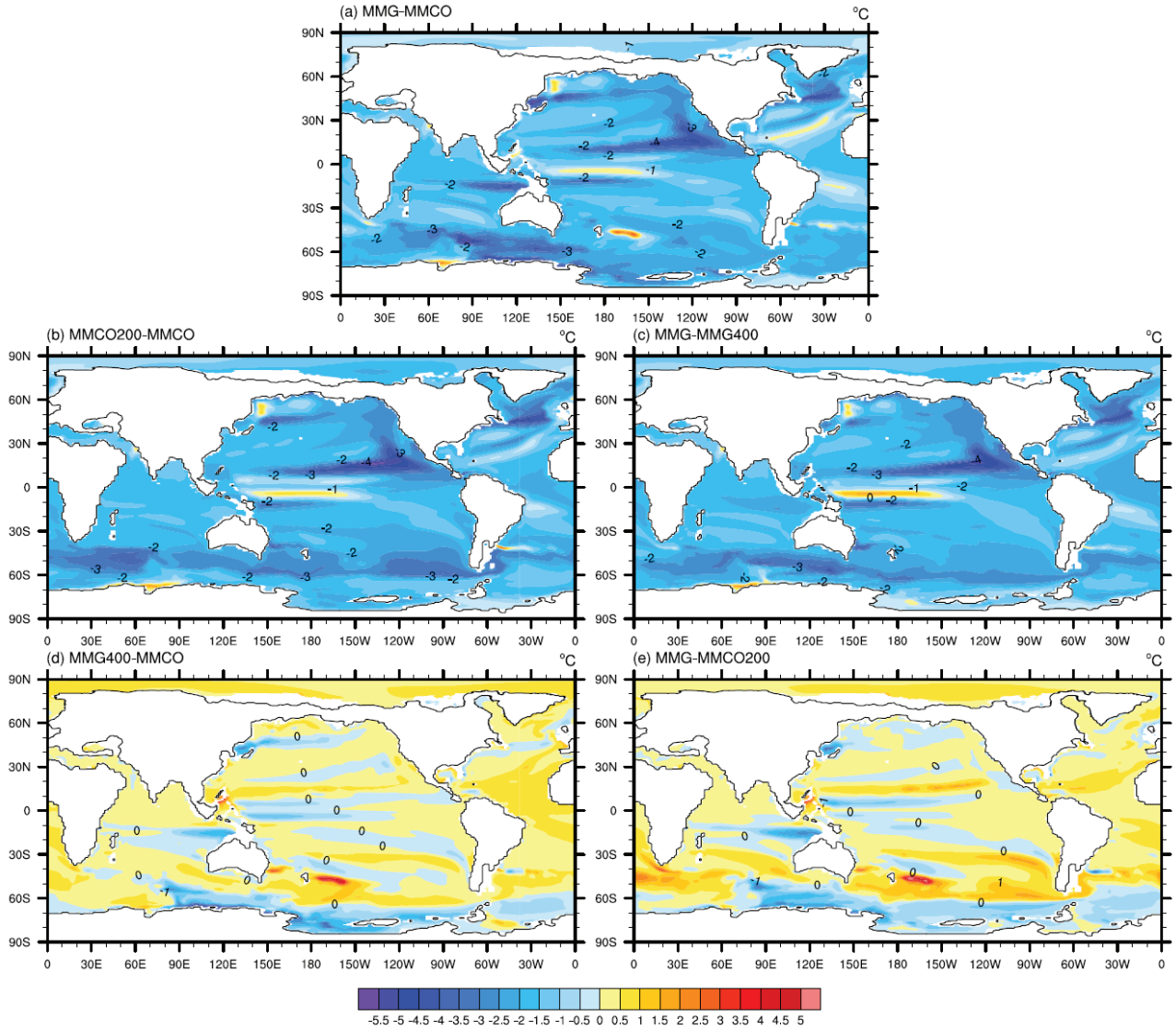

Figure 3.23. *Ocean temperature differences at 159.3–183.5 m depth: a) MMG-MMCO (MMCT), b) MMCO200-MMCO and c) MMG-MMG400 (CO_2 effect), and d) MMG400-MMCO and e) MMG-MMCO200 (ice sheet effect), in °C.*

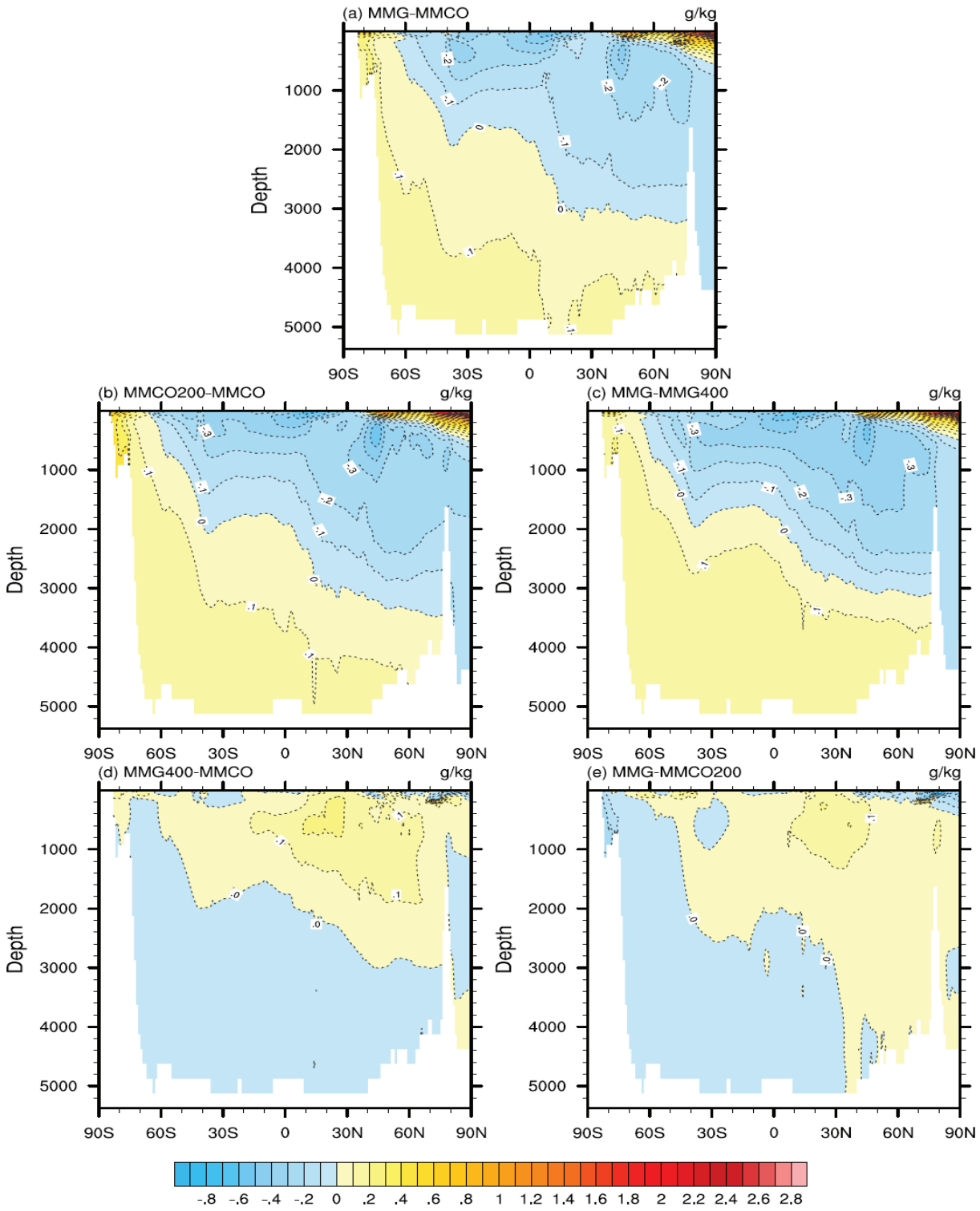

Figure 3.24. *Zonally averaged salinity differences for the Atlantic: a) MMG-MMCO (MMCT), b) MMCO200-MMCO and c) MMG-MMG400 (CO_2 effect), and d) MMG400-MMCO and e) MMG-MMCO200 (ice sheet effect), in g/kg.*

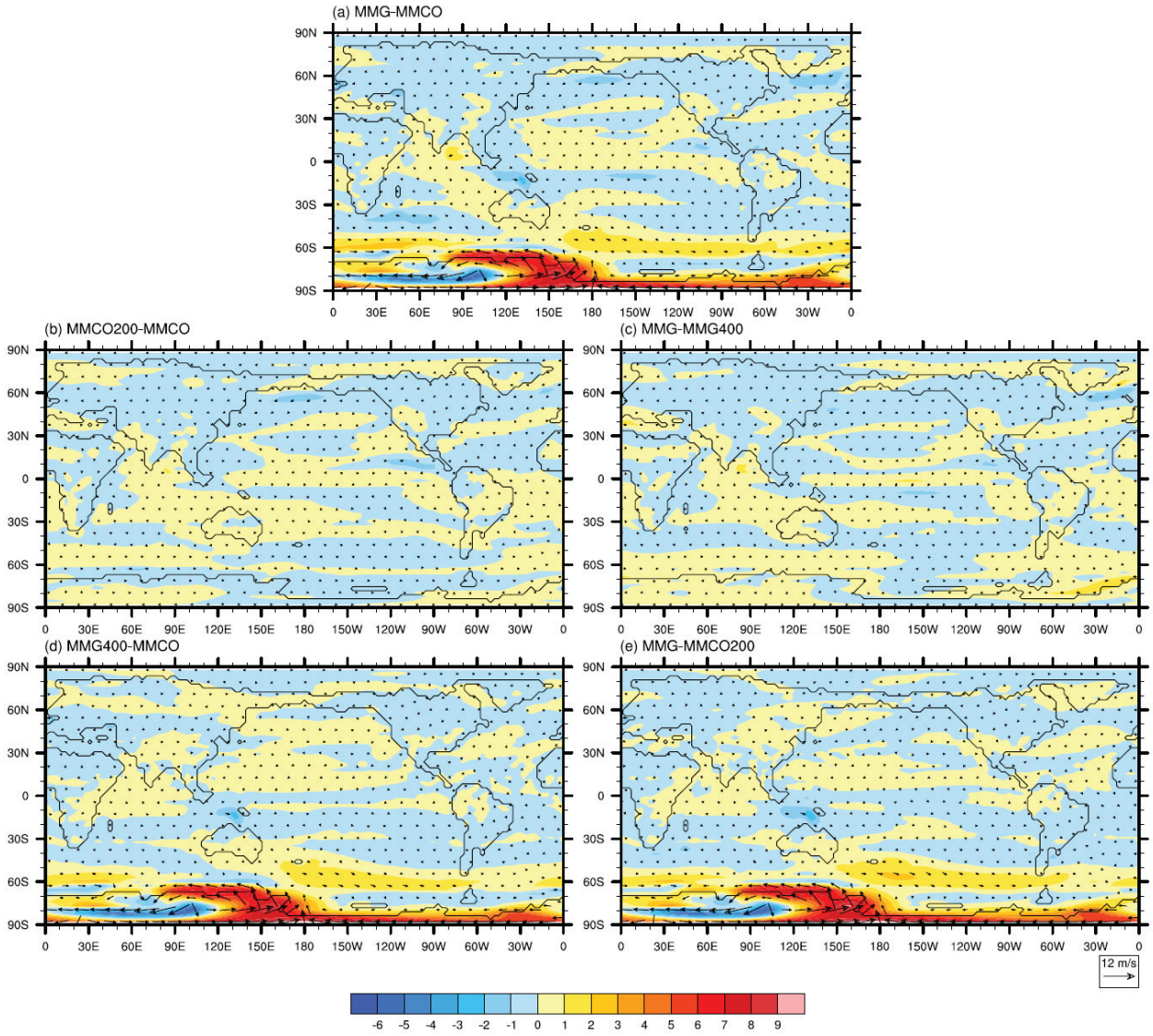

Figure 3.25. *Near-surface wind differences: a) MMG-MMCO (MMCT), b) MMCO200-MMCO and c) MMG-MMG400 (CO_2 effect), and d) MMG400-MMCO and e) MMG-MMCO200 (ice sheet effect), in m/s.*

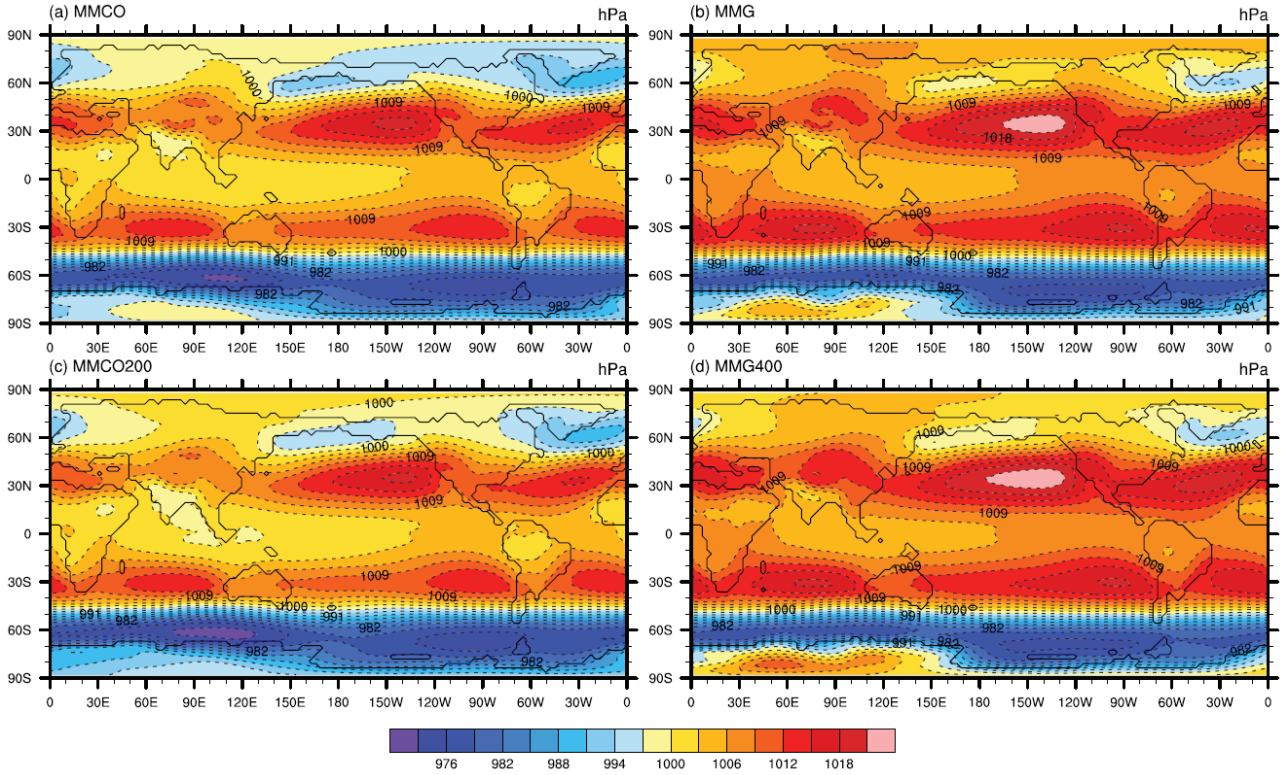

Figure 3.26. *Sea level pressure: a) MMCO, b) MMG, c) MMCO200, and d) MMG400, in hPa.*

3.4. Discussion

3.4.1. The global ocean during the Middle Miocene versus PI

This study supports the idea of a Middle Miocene climate warmer than PI (Pound et al., 2012). During the MMCO, for example, we modeled global mean SSTs 2.77 °C warmer than during PI (Fig. 3.1.). The regions presenting the strongest warming of sea surface waters compared to PI are the northern North Pacific, the North Atlantic, and the Southern Hemisphere middle and high latitudes. In the northern North Pacific and the North Atlantic these warmer conditions are linked to the absence of Northern Hemisphere ice sheets and the closed Bering Strait configuration in our boundary conditions. At the Southern Hemisphere middle and high latitudes the warming is

probably related to the less extensive Antarctic ice sheets compared to PI. Also ocean temperatures at depth are significantly warmer during the Middle Miocene compared to PI. At 2000–2250 m depth, e.g., during the MMCO, mean global temperatures are 2.72 °C warmer than at PI (Fig. 3.2.).

A remarkable difference in ocean circulation between the Middle Miocene and PI is the significantly weaker ACC (Fig. 3.3.), ~ 60 Sv weaker at the Drake Passage for MMCO. This feature is linked to the more southern position of Australia during the Middle Miocene. Another interesting feature is the stronger deeper cell of the MOC and the weaker upper cell during the Middle Miocene, compared to PI (Fig. 3.4.). Besides, we observe increased poleward ocean heat transport in the Southern Hemisphere and decreased poleward ocean heat transport in the Northern Hemisphere during the Middle Miocene (Fig. 3.5.).

3.4.2. Cooling of surface waters across the MMCT

Mean global SSTs decrease 1.58 °C across the MMCT, with the most pronounced cooling occurring in the Southern Ocean and the northern North Pacific (Fig. 3.6.). Mg/Ca data from ODP Hole 1171C at the South Tasman Rise, which would have been located at ~ 55° S during the Middle Miocene, indicate a decrease in the local SSTs across the MMCT of ~ 2 °C (Shevenell et al., 2004). This value is in good agreement with our modeled value for that area (2–3 °C of cooling) (to allow comparison we assumed that the longitude of that site remained unchanged since the Middle Miocene: ~ 149° E).

Our results indicate that the forcing responsible for the decrease in mean global SSTs across the MMCT is the dropdown in atmospheric CO_2 (Fig. 3.6.). The CO_2 dropdown cools down the atmosphere, triggering a positive heat flux from the ocean to the atmosphere and thus causing cooling of the upper ocean (Wong and Minnett, 2018). The Antarctic ice sheet expansion, contrarily, produces a very slight increase in global mean SSTs. Surface cooling over Antarctica induced by the

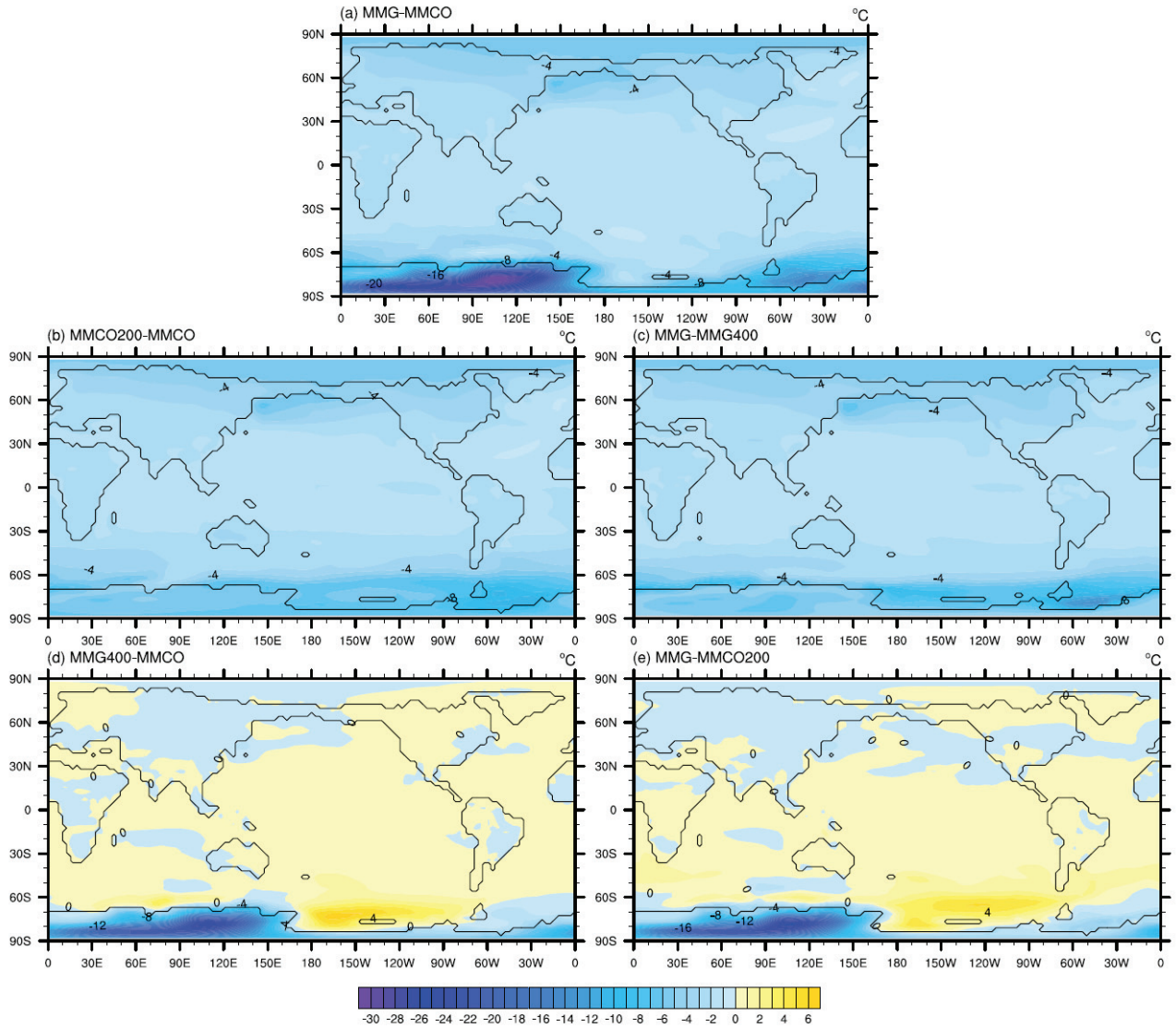

Figure 3.27. *Surface air temperature differences: a) MMG-MMCO (MMCT), b) MMCO200-MMCO and c) MMG-MMG400 (CO_2 effect), and d) MMG400-MMCO and e) MMG-MMCO200 (ice sheet effect), in °C.*

increased topography (Fig. 3.27.) causes a decrease in the upwelling longwave flux at the top of the atmosphere in that area (Fig. 3.28.), inducing a reduction in the southward atmospheric energy transport outside Antarctica (Singh et al., 2016) and thus a slight increase in surface air temperatures (SATs) (and SSTs) outside Antarctica (Figs. 3.27., 3.6.).

Note, also, that the response of SSTs to the two different forcings is highly linear: the decrease of

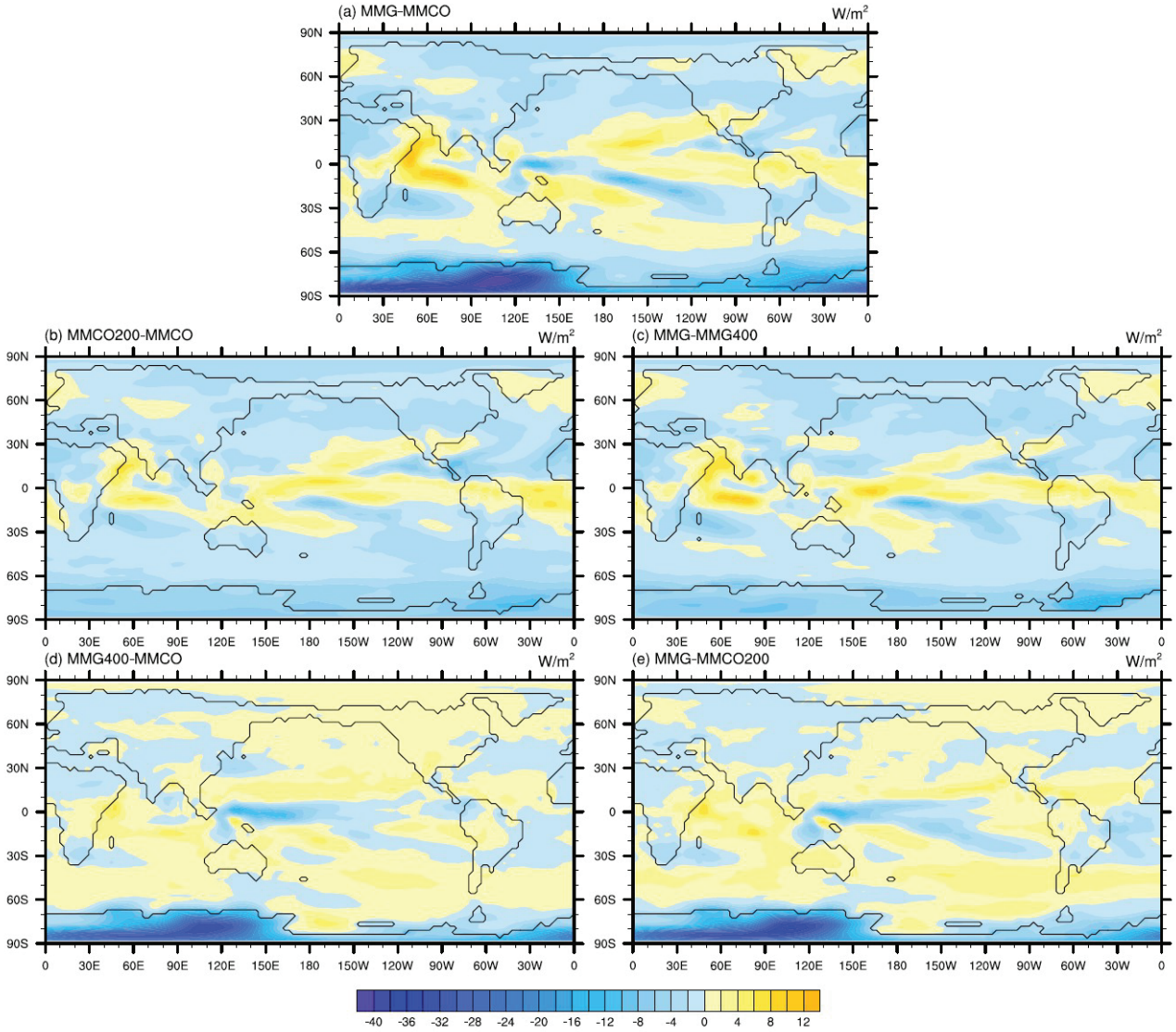

Figure 3.28. *Upwelling longwave flux differences at the top of the atmosphere: a) MMG-MMCO (MMCT), b) MMCO200-MMCO and c) MMG-MMG400 (CO_2 effect), and d) MMG400-MMCO and e) MMG-MMCO200 (ice sheet effect), in W/m².*

1.58 °C in SST across the transition is the addition of the decrease in SSTs of 1.95 °C due to the CO_2 dropdown (non-expanded ice sheet) and the increase in SSTs of 0.37 °C due to the Antarctic ice sheet expansion (CO_2 fixed at 200 ppmv). The study by Knorr and Lohmann (2014), also assessing the roles of the CO_2 decrease and the Antarctic ice sheet expansion across the MMCT,

supports this linearity. They report a decrease in global mean SATs of 3.7 °C in response to the CO_2 forcing, and an increase in global mean SATs of 0.7 °C in response to the Antarctic ice sheet forcing. In that study the effect of combining both forcings is a decrease in global mean SATs of 3.1 °C.

Another remarkable result in our experiments is the mixed pattern of warming and cooling of Southern Ocean surface waters across the MMCT induced by the expansion of the Antarctic ice sheet (Fig. 3.6.). This feature is also present in the studies by Knorr and Lohmann (2014) and Goldner et al. (2014), with the latter modeling the Eocene/Oligocene transition.

3.4.3. Cooling at depth across the MMCT

Our results show decreases in ocean water temperatures at depth of 1.5–2 °C at almost all depths and latitudes (Fig. 3.7.). Different studies have assessed cooling of deep waters across the MMCT using Mg/Ca ratios: Lear et al. (2010) reported a decrease in BWTs of ~ 2 °C between 16.7 and 12 Ma; Lear et al. (2000), a decrease of ~ 2 °C between 15 and 10 Ma; Shevenell et al. (2008), a decrease of ~ 2 ±2 °C at the interval 14.1-13.7 Ma, and Billups and Schrag (2002), a decrease of ~ 3 °C at 15–13 Ma. Our modeled values explain a larger part of the deep water cooling inferred from Mg/Ca studies (Figs. 3.7., 3.8.). The reason for the lower decrease in deep ocean temperatures in our experiments compared to proxy data estimates may lie in the small trends in the deep ocean temperatures present in our runs (see sect. 2.2.)

In our results the CO_2 cooling effect dominates the Antarctic ice sheet effect. The CO_2 decrease causes significant cooling practically everywhere, being this more pronounced in the upper cell of the MOC, compared to the lower cell (Fig. 3.7.). The effect of the Antarctic ice sheet expansion on ocean temperatures depends significantly on the depth. Cooling is dominant below ~ 1400 m, meanwhile above that level warming occurs (Fig. 3.7.).

In the Southern Ocean, cooling originates close to or at the surface and spreads to the bottom through water convection. Clear evidence of AABW formation during the MMCO and MMG is provided by the existence of a MOC deeper cell (Fig. 3.4.) and the steep isopycnals below ~ 60° S in the potential density field (Fig. 3.10.). Note that both the CO_2 decrease and Antarctic ice sheet expansion are responsible for the cooling of waters at the deeper cell of the MOC (Fig. 3.7.).

Furthermore, increases in potential density of 0.2–0.25 kg/m^3 for the waters attached to and at the bottom of the Antarctic shelf (Fig. 3.12.) suggest an increase in AABW formation across the MMCT. This increase in AABW formation would be caused by the CO_2 dropdown triggering salinity increases in the surroundings of Antarctica (Fig. 3.13.) through sea ice formation (Fig. 3.14.) and through changes in the evaporation/precipitation balance (Fig. 3.15.).

The MOC field, though, does not support uniform strengthening of the deeper cell of the MOC across the MMCT (Fig. 3.16.). Strengthening of the deeper cell of the MOC occurs below ~ 70° S (2–3 Sv), and also between 0–30° S, below ~ 3400 m (up to 7–8 Sv), but also weakening occurs, for example, between 55–65° S, below ~ 2000 m (up to 4–5 Sv). However, only the Eulerian MOC was available in this study, the eddy-induced MOC effect was dismissed. The study by Holbourn et al. (2013) suggests significant strengthening of the deeper cell of the Pacific MOC during the MMCT. Although a general strengthening tendency could not be inferred from our global MOC field, the potential density field averaged over Pacific longitudes would support the results by Holbourn et al. (2013) (Fig. 3.29.).

Ocean temperatures in the North Atlantic decrease more than 2 °C above 2500 m depth across the transition as a response to the atmospheric CO_2 dropdown (Fig. 3.17.). Cooling of the upper ocean in that area is transmitted to the depth through water convection at ~ 50–60° N as shown in the potential density and mean boreal winter mixed layer depth fields (Figs. 3.18., 3.19.). Water convection happens both during the MMCO and the MMG, although the convection area deepens across the transition. During the MMCO the mean boreal winter mixed layer reaches depths down

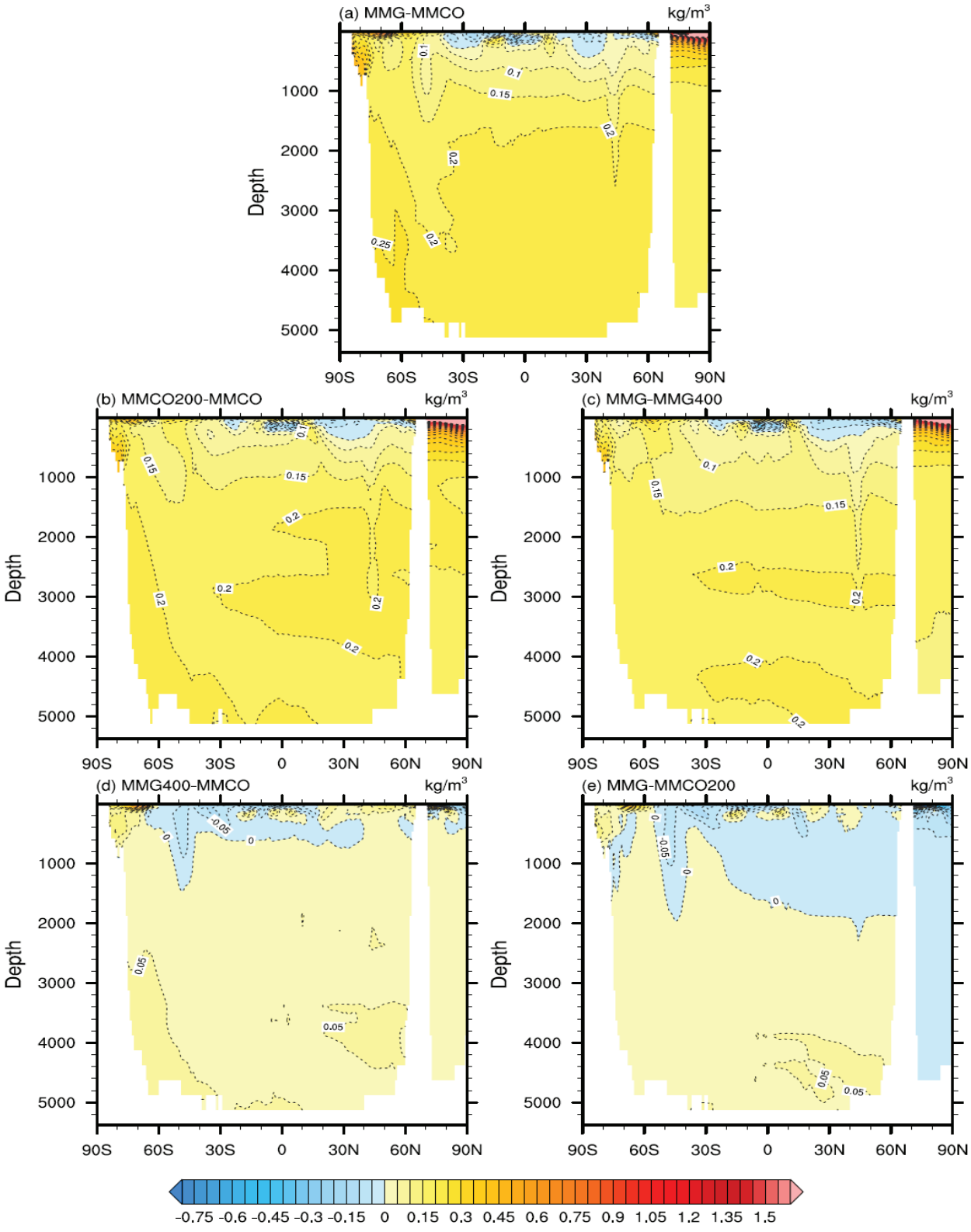

Figure 3.29. *Zonally averaged potential density differences for the Pacific: a) MMG-MMCO (MMCT), b) MMCO200-MMCO and c) MMG-MMG400 (CO_2 effect), and d) MMG400-MMCO and e) MMG-MMCO200 (ice sheet effect), in kg/m³. Note: potential density is averaged over the longitude interval 100° E to 259° E.*

to ~ 1600 m meanwhile at the MMG the convection area has expanded and the mean boreal winter mixed layer reaches down to ~ 1770 m (Fig. 3.19.). This moderate increase in convection in the North Atlantic is further supported by the MOC field (Figs. 3.4., 3.16.) and it is a consequence of the CO_2 decrease.

Convection of deep waters in the North Atlantic during the Middle Miocene is a matter of debate in the literature. Butzin et al. (2011) suggest that development of the North Atlantic convection cell would be linked to shallowing of the Panama seaway to ~ 250 m depth in the late Miocene. Von der Heydt and Dijkstra (2006) support the existence of a North Atlantic cell in the Late Oligocene and the Early Miocene. Hamon et al. (2013) describe a well-defined North Atlantic cell during the Middle Miocene, in agreement with the current study.

Our results point at the high salinities (> 35.7 g/kg at 60° N at ~ 500 m depth) (Fig. 3.21.) and the relatively cold upper ocean waters (Fig. 3.22.), as the causes of convection in the North Atlantic during the MMCO and MMG. The increase in convection across the MMCT is not linked to the salinity field but to a decrease in upper ocean temperatures (~ 2.5–3 °C, e.g., at ~ 171 m depth between 50–60° N).

3.4.4. Strengthening of near-surface winds in the Southern Hemisphere across the MMCT

Our results show important changes in the pattern of near-surface winds in the Southern Hemisphere across the MMCT (Fig. 3.25.). Significant strengthening of the polar easterlies is observed along the Antarctic coast. This strengthening is caused by an increase in the pressure gradient between the polar highs and the subpolar lows associated with the Antarctic topography rise across the MMCT (Fig. 3.26.). Besides, moderate strengthening of the westerlies is observed in the Southern Ocean at a global belt at ~ 50–60° S. This change is due to the increase in the pressure

gradient between subpolar lows and subtropical highs, induced by the Antarctic topography rise. Several studies support our results. The Eocene/Oligocene transition study by Goldner et al. (2014) shows important strengthening of the pressure gradient and surface winds around Antarctica as a result of the Antarctic ice sheet expansion (topography + albedo forcings). Knorr and Lohmann (2014) find important changes across the MMCT in the surface wind field around Antarctica, caused by the rise of the Antarctic topography (albedo is kept constant in that study). The study by Singh et al. (2016) suggests that flattening of the Antarctic topography causes deceleration of the easterlies south of 65° S and of the westerlies north of 60° S.

4. Modeling the Indonesian Throughflow during the MMCT

In this chapter of the thesis, we zoom into Southeast Asia to provide new insights into the ITF during the MMCT. The model topography/bathymetry based on the geographical reconstruction of Southeast Asia for 15 Ma by Hall (2012) (see sect. 2.2.4.3.) and the fine grid resolution employed in our ocean model configuration (see sect. 2.1.) are key factors in achieving our aims.

4.1. ITF volume transport during PI

The volume transport across the Indonesian gateway during the PI was computed by adding up the values of two sections: a) at longitude 114.13° E, with latitude spanning the interval 8.28–21.50° S; and b) from (107.38° E, 6.41° S) to (105.13° E, 5.61° S) (Fig. 4.1.). Our modeled value of -17.38 Sv is higher than the observational best estimate for present-day by Sprintall et al. (2009) (-15 Sv), although it falls within the uncertainty range suggested in that study (-10.7 to -18.7 Sv). The work

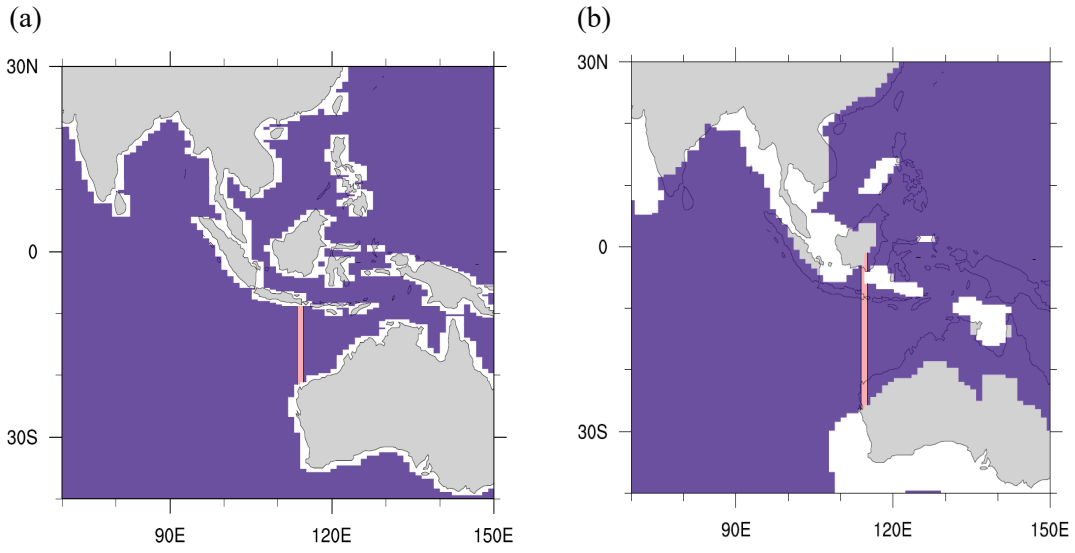

Figure 4.1. *(a) PI and (b) Middle Miocene (MMCO) land-sea masks for the Southeast Asian region. The meridional sections used for the volume transport calculations are shown in pink. Black lines indicate the present-day coastline.*

by Sprintall et al. (2009), a fruit of the International Nusantara Stratification and Transport (INSTANT) program, presents the first set of simultaneous volume transport measurements at the three ITF exit passages: Lombok, Timor and Ombai.

The bulk of the ITF flow occurs between 8–12° S, above 200 m depth, and it is characterized by westward velocities of up to 28–32 cm/s (Fig. 4.2.). The modeled ITF waters are mainly of North Pacific origin (Fig. 4.3.). The months of highest transport are between June and August, with the maximum ITF transport occurring in July (-22.21 Sv) (Fig. 4.4.). The ITF transport is lowest from November to February, with the minimum ITF transport occurring in December (-12.98 Sv) (Fig. 4.4.). Also the observational data from Sprintall et al. (2009) indicate an annual maximum in transport in July (-17.9 Sv). The annual minimum in those data, though, does not occur in December but in October and it is attributed to the existence of Kelvin waves originating from the Indian Ocean (Sprintall et al., 2009).

Our results indicate that the ITF transport seasonal variability is influenced by the Pacific Ocean circulation. During boreal summer, the cyclonic gyre below the North Pacific Gyre moves west from its position during boreal winter (Figs. 4.5., 4.6.), causing an increase in water transport through the Indonesian gateway. Furthermore local winds have an effect on the ITF volume transport. The northwest wind regime from December to February (Fig. 4.7.) hampers the flow through the Indonesian archipelago into the Indian Ocean.

The seasonal variability of ITF SSTs (Fig. 4.4.) was calculated by averaging over two sections, similar to volume transport. In the first section, longitude is fixed at 114.69° E and latitude spans the interval 8.68–21.69° S. In the second section, longitude is fixed at 105.69° E and latitude spans the interval 5.74–6.01° S. The annual maximum value is 29.32 °C and it occurs in March, the minimum value is 25.61°C and it occurs in September (Fig. 4.4.). This seasonal pattern responds to the annual cycle of solar insolation at the Equator (Schneider, 1996).

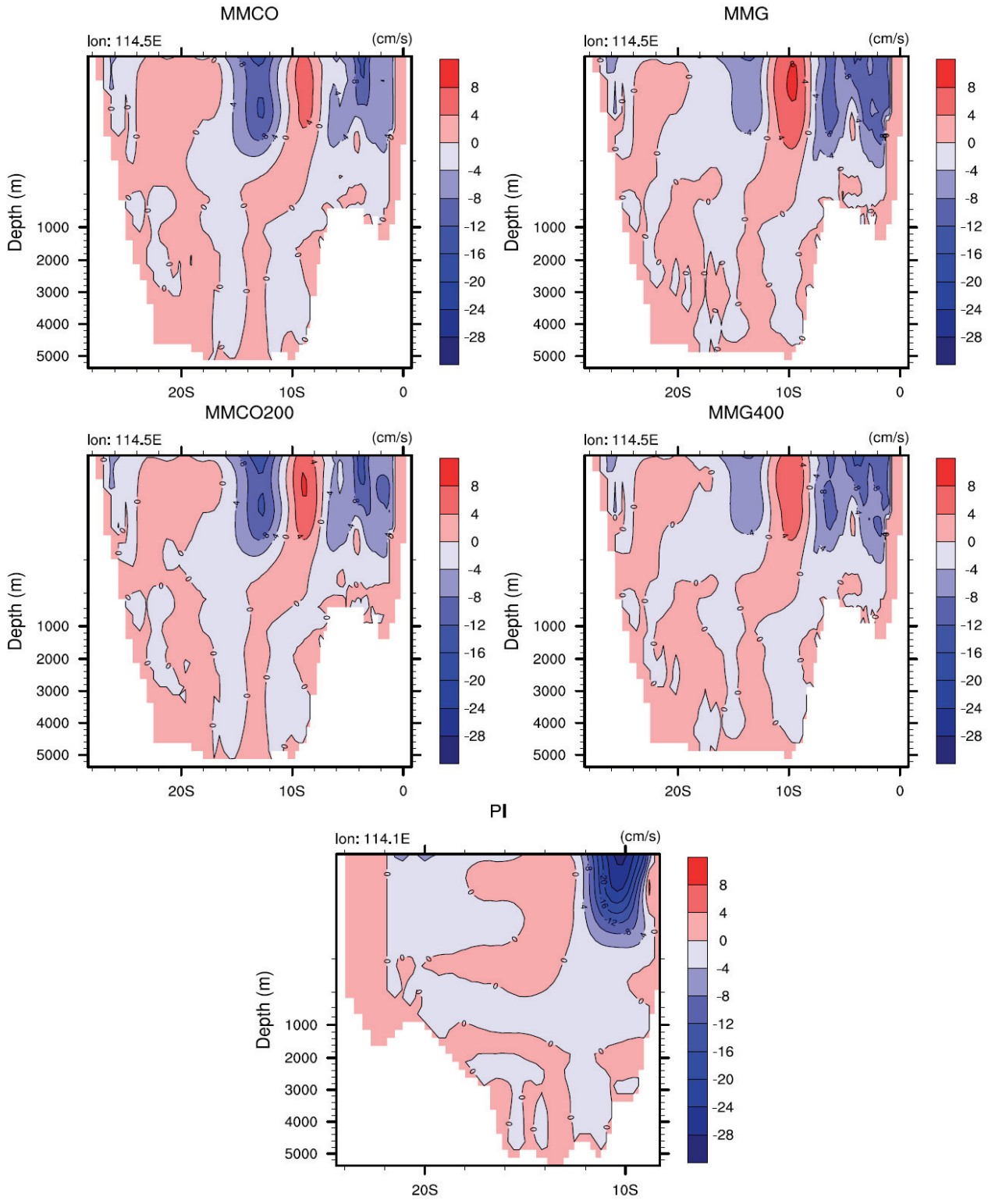

Figure 4.2. *Vertical profile of zonal velocity at the ITF gateway for MMCO, MMG, MMCO200, MMG400, and PI, in cm/s. Negative velocities denote westward currents.*

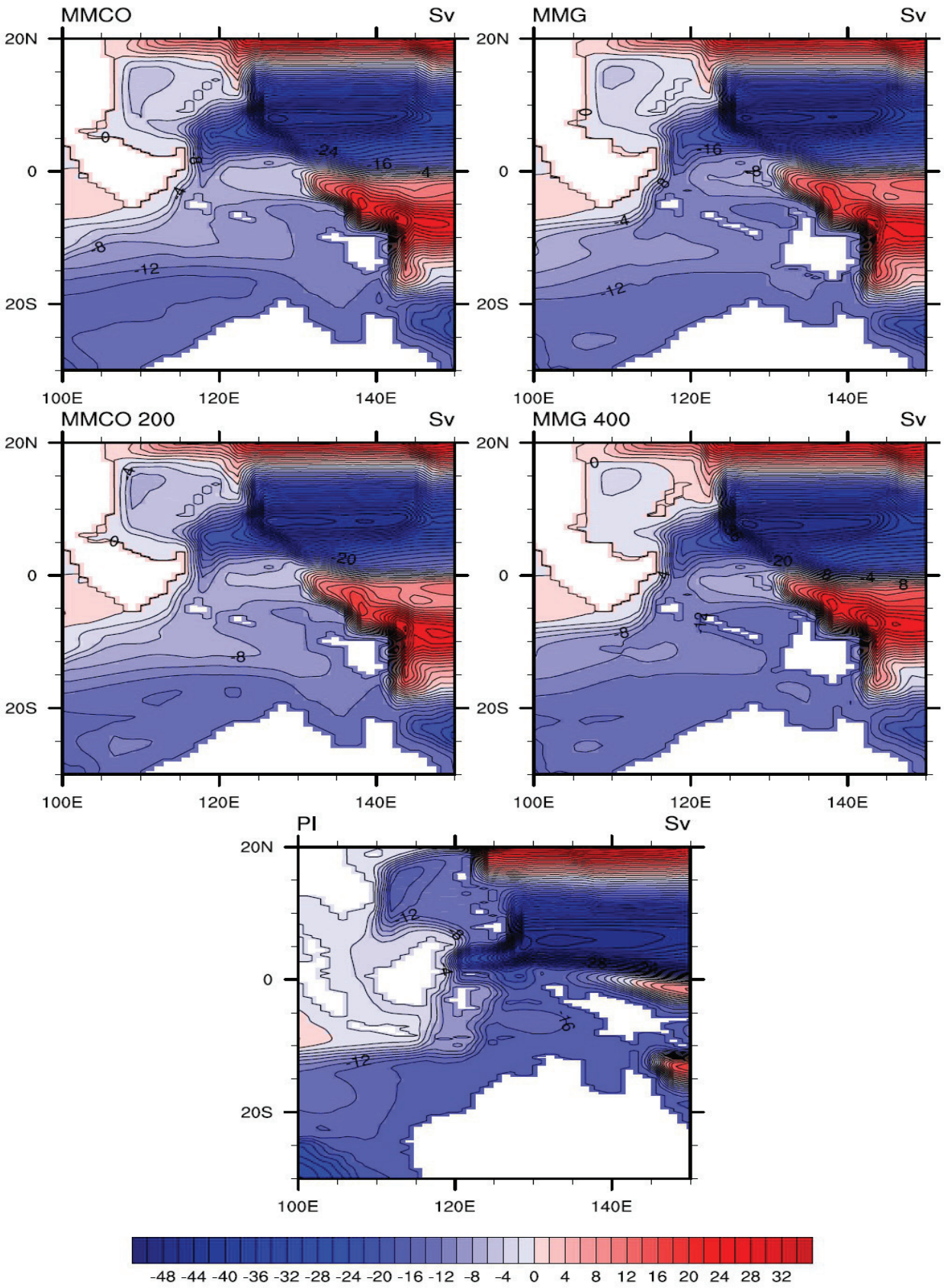

Figure 4.3. *Barotropic stream function at the Southeast Asian region for MMCO, MMG, MMCO200, MMG400, and PI, in Sv (annual mean).*

4.2. ITF volume transport during the MMCO

The volume transport through the Middle Miocene Indonesian gateway was calculated using the section described in Fig. 4.1., where longitude is fixed at 114.5° E and latitude spans the interval 1.00–26.34° S. A value of -13.30 Sv was obtained for the MMCO, of which -7.7 Sv flow through the western passage of Makassar Strait, and the rest through the eastern passages between Sulawesi and New Guinea (-3.3 Sv), and between New Guinea and northern Australia (-2.5 Sv) (Fig. 4.3.). During the Middle Miocene the Indonesian gateway was open to surface and intermediate waters as at the present-day (Kuhnt et al., 2004). This is consistent with our modeled value for the MMCO. Nevertheless, our modeled transport at MMCO is lower than at PI, since although the passage was wider at the MMCO, it was also shallower (Fig. 4.8.). However, uncertainties in the bathymetry for the Middle Miocene are high.

The bulk of the ITF outflow to the Indian Ocean for MMCO occurs in the upper 200 m of the vertical section, with westward velocities of up to 12–16 cm/s at both the western (1–6° S) and eastern (11–16° S) paths (Fig. 4.2.). The weak eastward current between 8–10° S shown in Fig. 4.2. is just a meander of the westward flow and it does not reach the Pacific Ocean as it can be derived from the barotropic stream function field (Fig. 4.3.).

During the MMCO, the volume transport across the Indonesian gateway is highest from July to October, with the maximum occurring in August (-25.39 Sv) (Figs. 4.4., 4.9.). The lowest transport values correspond to the months of December–March, with the minimum occurring in January (-5.15 Sv) (Figs. 4.4., 4.10.).

The cause for increased transport from July to October is the southeast wind regime over the Indonesian archipelago (Fig. 4.11.) which enhances flow of Pacific waters into the Indian Ocean through Ekman transport divergence. During those months, ITF waters originate both from the Pacific North Equatorial Current and the Pacific South Equatorial Current (Fig. 4.9., 4.6.), having

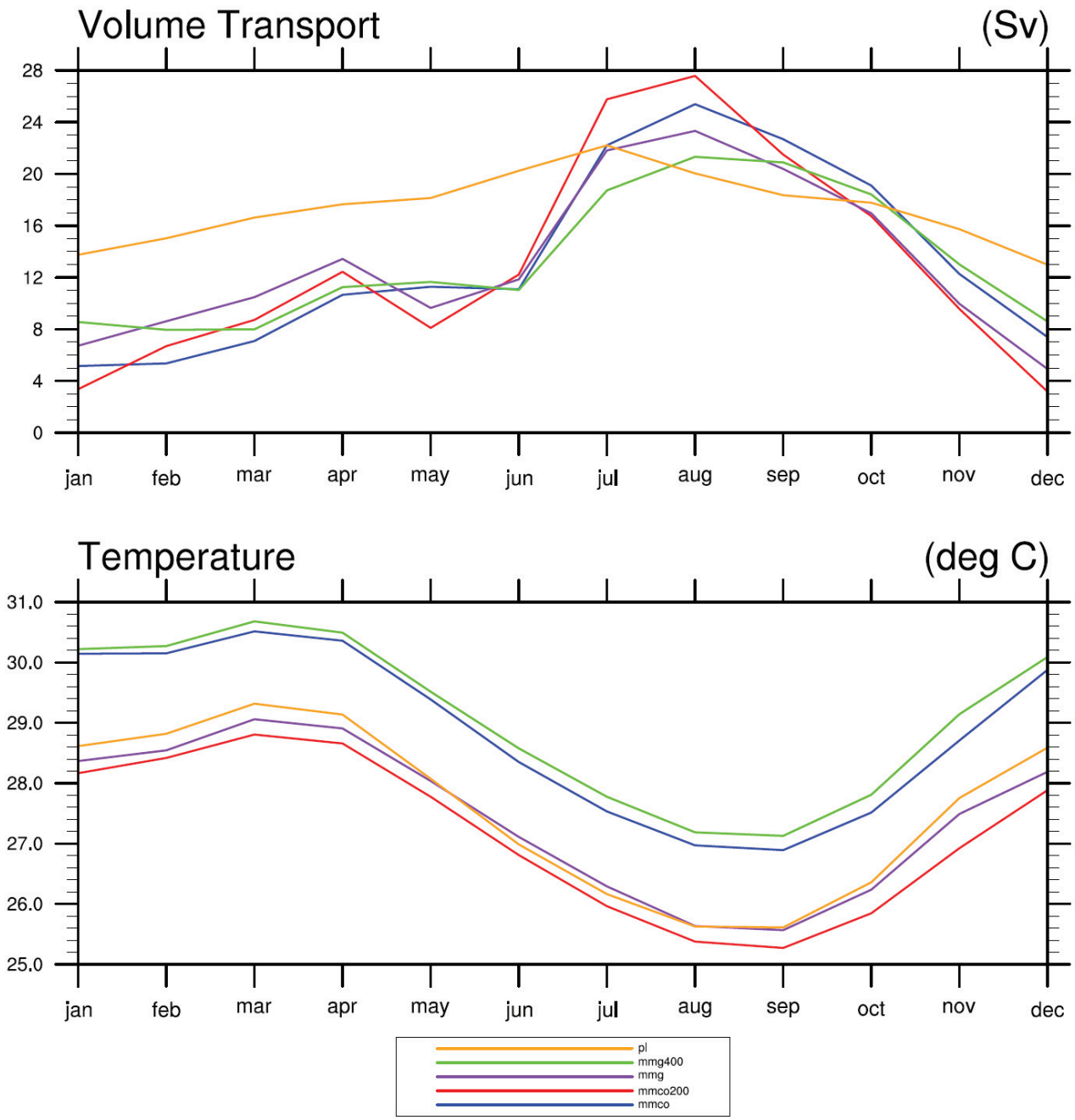

Figure 4.4. *Monthly variations of volume transport and sea surface temperature at the ITF gateway for MMCO, MMG, MMCO200, MMG400, and PI, in Sv and °C, respectively.*

thus both a South and a North Pacific component. Nevertheless, the South Pacific component is stronger than the North Pacific component, due again to the strong southeast winds present in the area, which favor the entrance of South Pacific waters into the Indonesian archipelago.

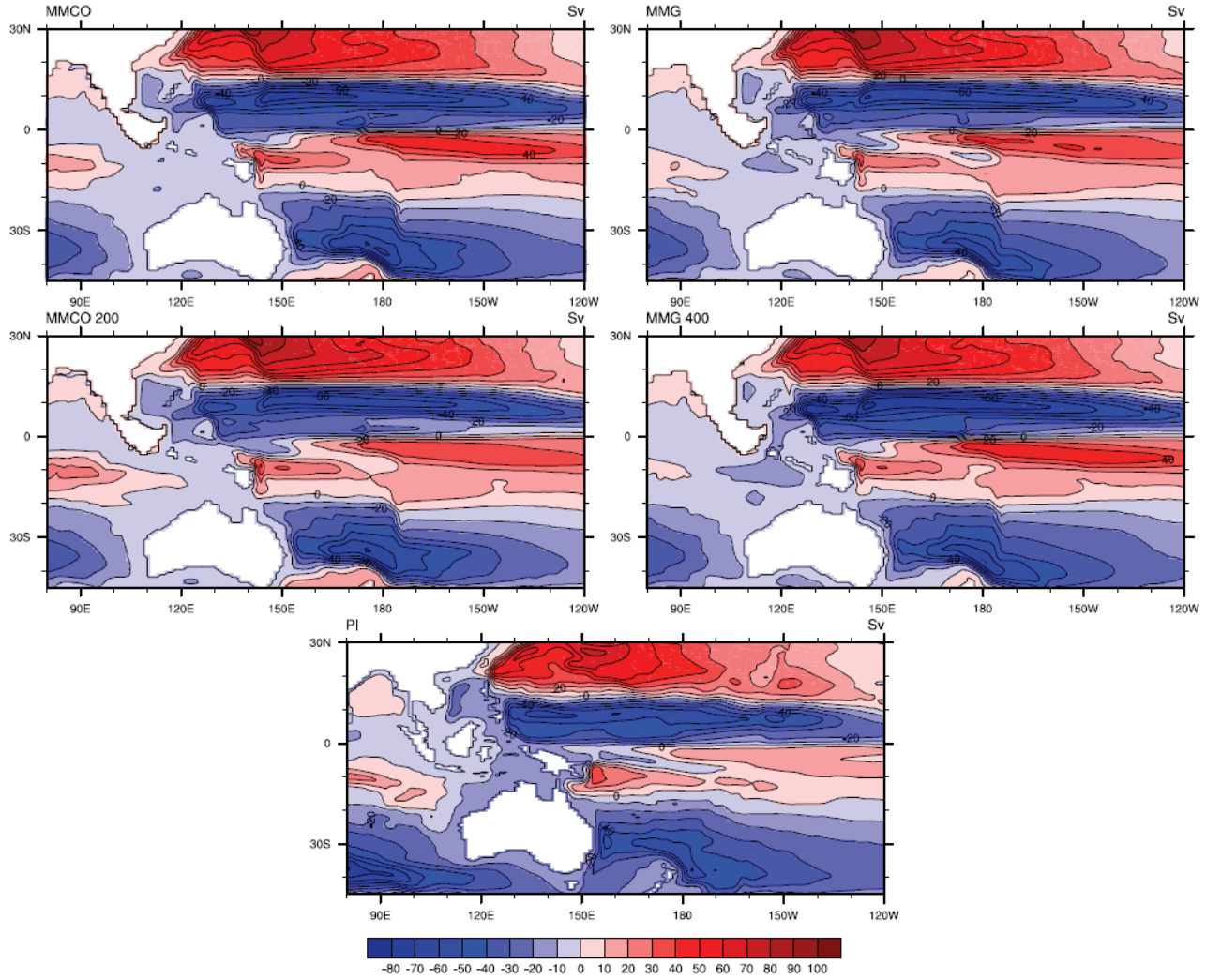

Figure 4.5. *Barotropic stream function in January for the Pacific for MMCO, MMG, MMCO200, MMG400, and PI, in Sv.*

During the months of lowest transport there is no (or very little) South Pacific component in the ITF (Fig. 4.10.). This fact is due to the lack of (or extremely weak) southeast winds over the area (Fig. 4.7.). The reason for reduced transport during those months is again the absence of southeast winds (Fig. 4.7.), which were enhancing the water flow into the Indian Ocean through increased Ekman transport divergence. Instead, the northwest winds present in the Indonesian area from December to February (Fig. 4.7.) partially block the flow into the Indian Ocean through the same Ekman transport mechanism.

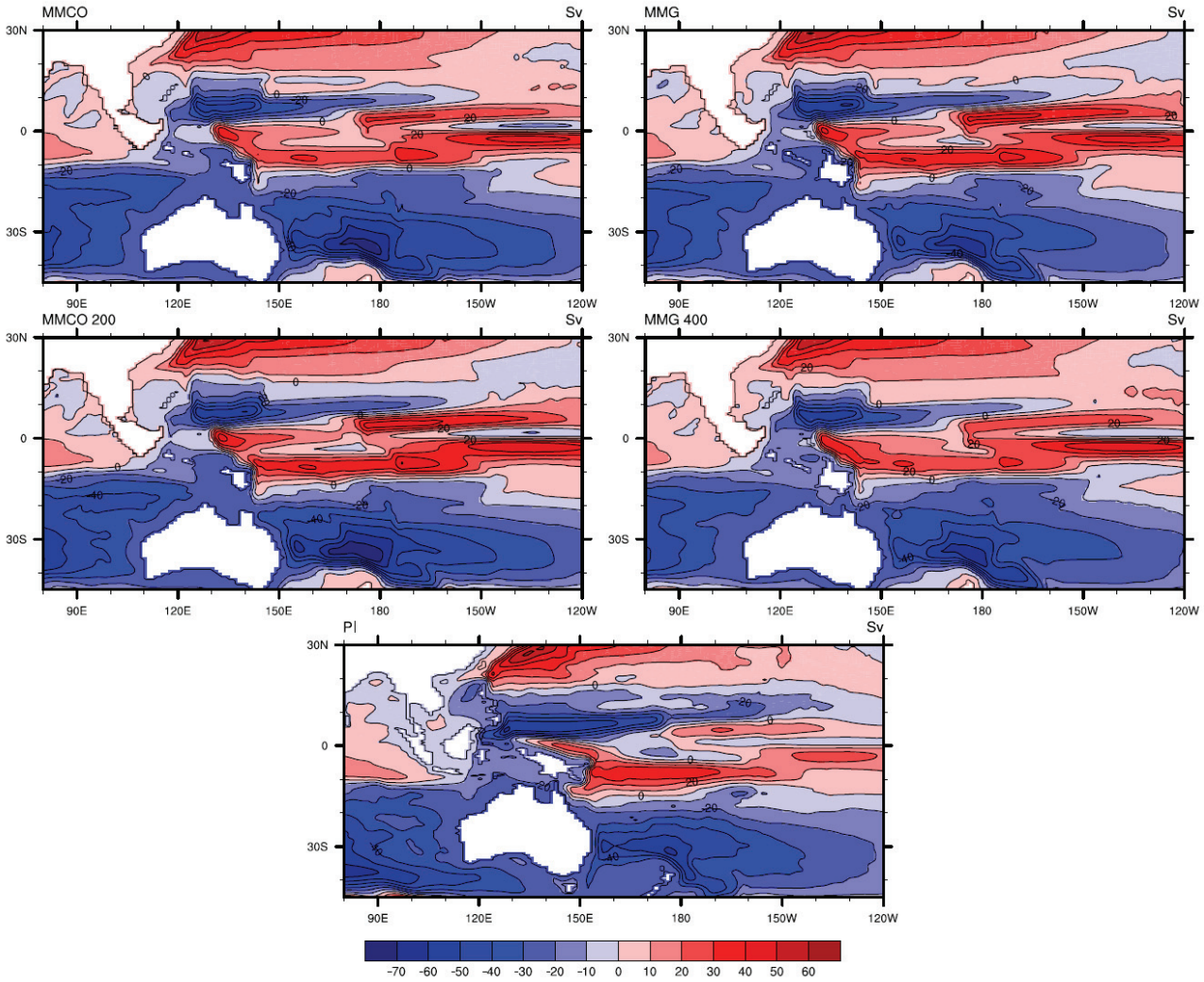

Figure 4.6. *Barotropic stream function in August for the Pacific for MMCO, MMG, MMCO200, MMG400, and PI, in Sv.*

Also monthly variations of ITF SSTs for MMCO were computed (Fig. 4.4.), using a similar section to the volume transport one, with longitude fixed at 115.06° E and latitude spanning the interval 28.05° S–0.63° N. Our results indicate a maximum in March, of 30.51 °C, and a minimum in September, of 26.89 °C which, as for the PI case, respond to the annual cycle of solar insolation at the Equator. The SSTs for MMCO are higher than for PI, mostly due to the higher atmospheric CO_2 concentrations during the MMCO (Fig. 4.4.).

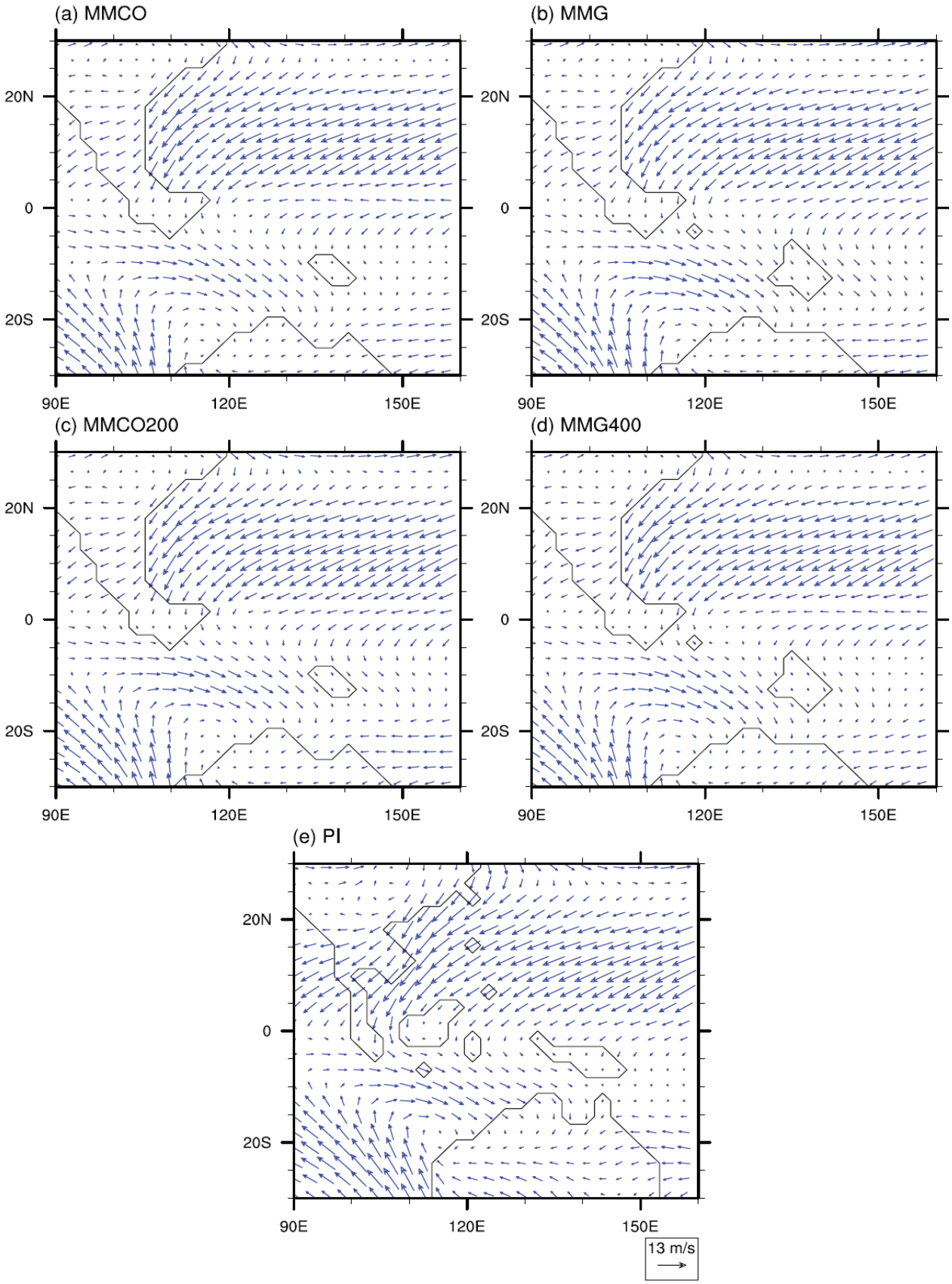

Figure 4.7. *Near-surface winds in January at the Southeast Asian region: a) MMCO, b) MMG, c) MMCO200, and d) MMG400, in m/s.*

4.3. Changes in the ITF transport across the MMCT

No substantial differences exist in the total volume transport through the Indonesian gateway before and after the MMCT (the modeled value for MMG is -13.18 Sv). After the MMCT, the months of highest transport are July–October and the maximum transport occurs in August (-23.33 Sv) (Figs. 4.4., 4.9.), as before the transition. The months of lowest transport are December–February and the minimum occurs in December (-4.92 Sv) (Fig. 4.4., 4.10.). As during the MMCO, the reason for increased volume transport from July–October are the strong southeast winds blowing over the Indonesian archipelago (Fig. 4.11.) causing enhanced flow to the Indian Ocean through Ekman transport divergence. From December to February, southeast winds weaken or reverse (Fig. 4.7.), causing a decrease in transport, as for the MMCO.

An interesting feature is the increase in transport across the MMCT through the western path (Makassar Strait), from -7.7 Sv at the MMCO to -10.7 Sv at the MMG (Fig. 4.3.), which is also visible in the vertical profile of zonal velocities (Fig. 4.2.), where the -(8–12) cm/s contour has gained terrain over the -(4–8) cm/s contour in the western path (1–7° S). This increase is not linked to any particular season or wind regime and the sensitivity analysis indicates that it is related to ice sheet forcing. On the contrary, the volume transport decreases in the eastern paths. Between Sulawesi and New Guinea, the volume transport decreases from -3.3 Sv at the MMCO to -1.3 Sv at the MMG. Similarly, between New Guinea and northern Australia, the volume transport decreases from -2.5 Sv to -1.3 Sv (Fig. 4.3.). This decrease in transport is also evident from Fig. 4.2., whereby westward velocities in the eastern path (12–16° S) reach values of only up to 8–12 cm/s. This decrease is related to the sea level dropdown across the MMCT (~ 43 m, see sect. 2.2.4.2.), significantly affecting the shallow topographic barriers of the eastern paths (Fig. 4.8.). Besides, a moderately weaker South Pacific Gyre after the MMCT (Figs. 4.5., 4.6.), might also reduce the intensity of the flow through the eastern path. The sensitivity runs indicate that these changes are

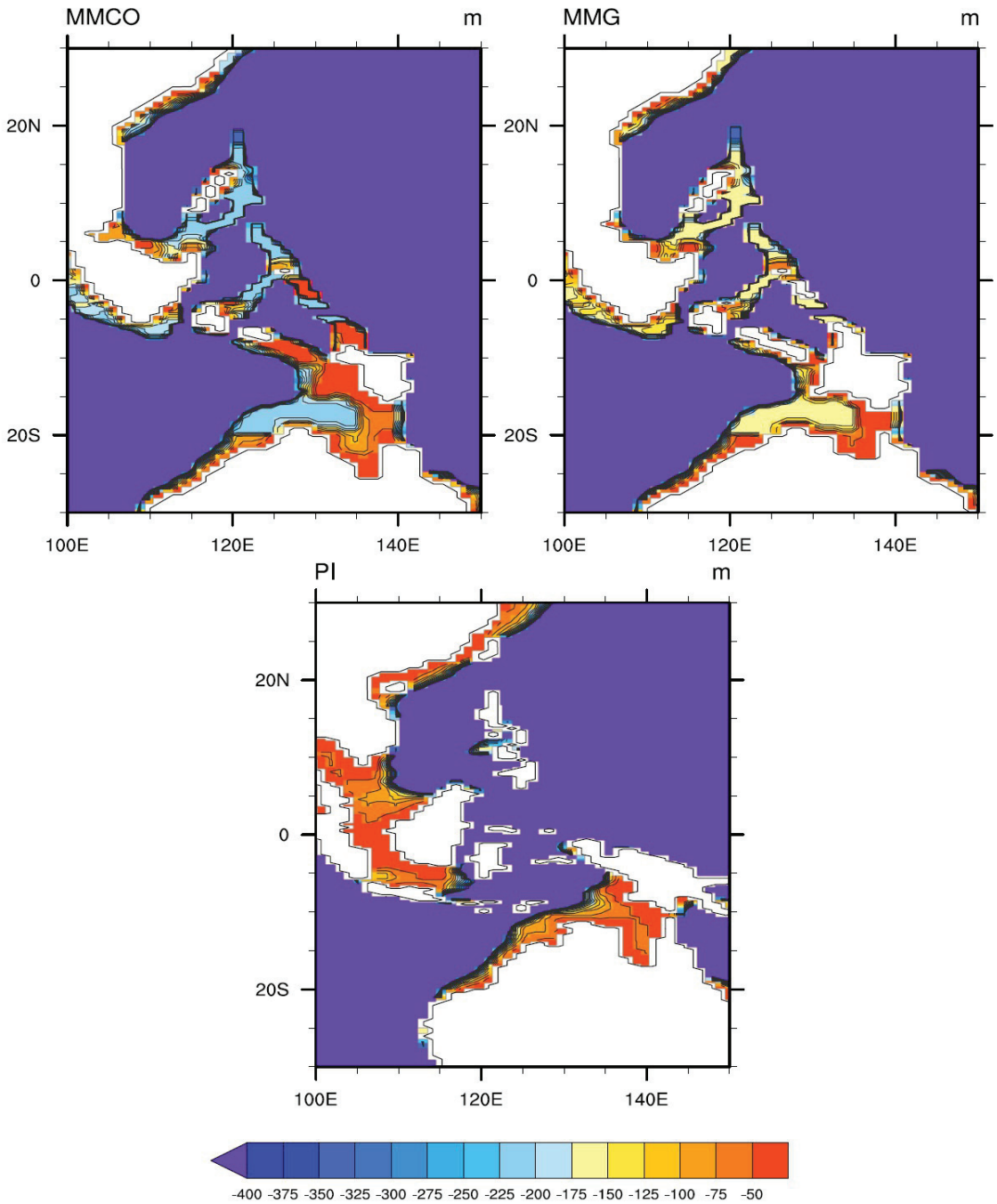

Figure 4.8. *Bathymetry of the Southeast Asian region for MMCO, MMG, and PI, in meters.*

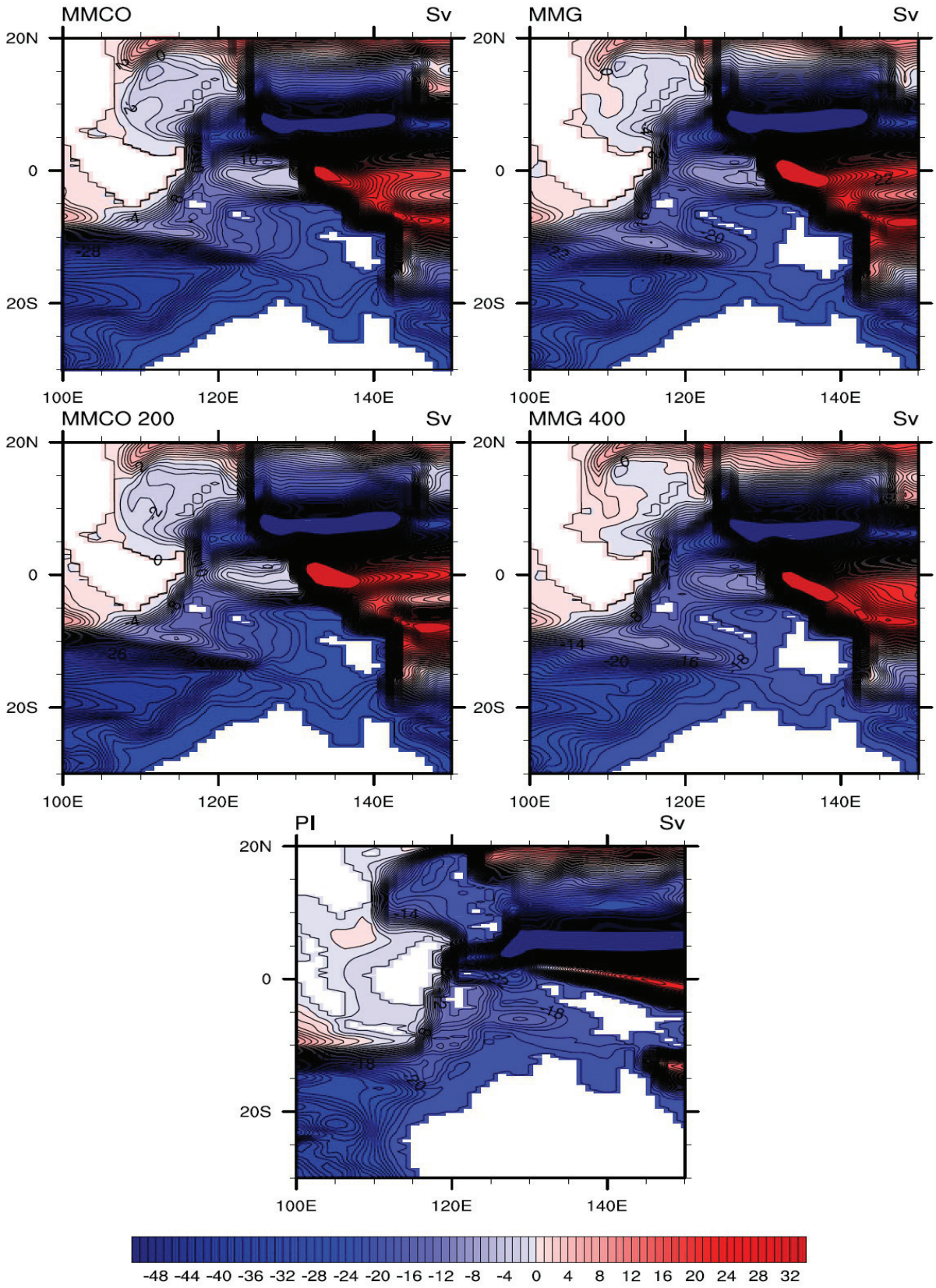

Figure 4.9. *Barotropic stream function in August at the Southeast Asian region for MMCO, MMG, MMCO200, MMG400, and PI, in Sv.*

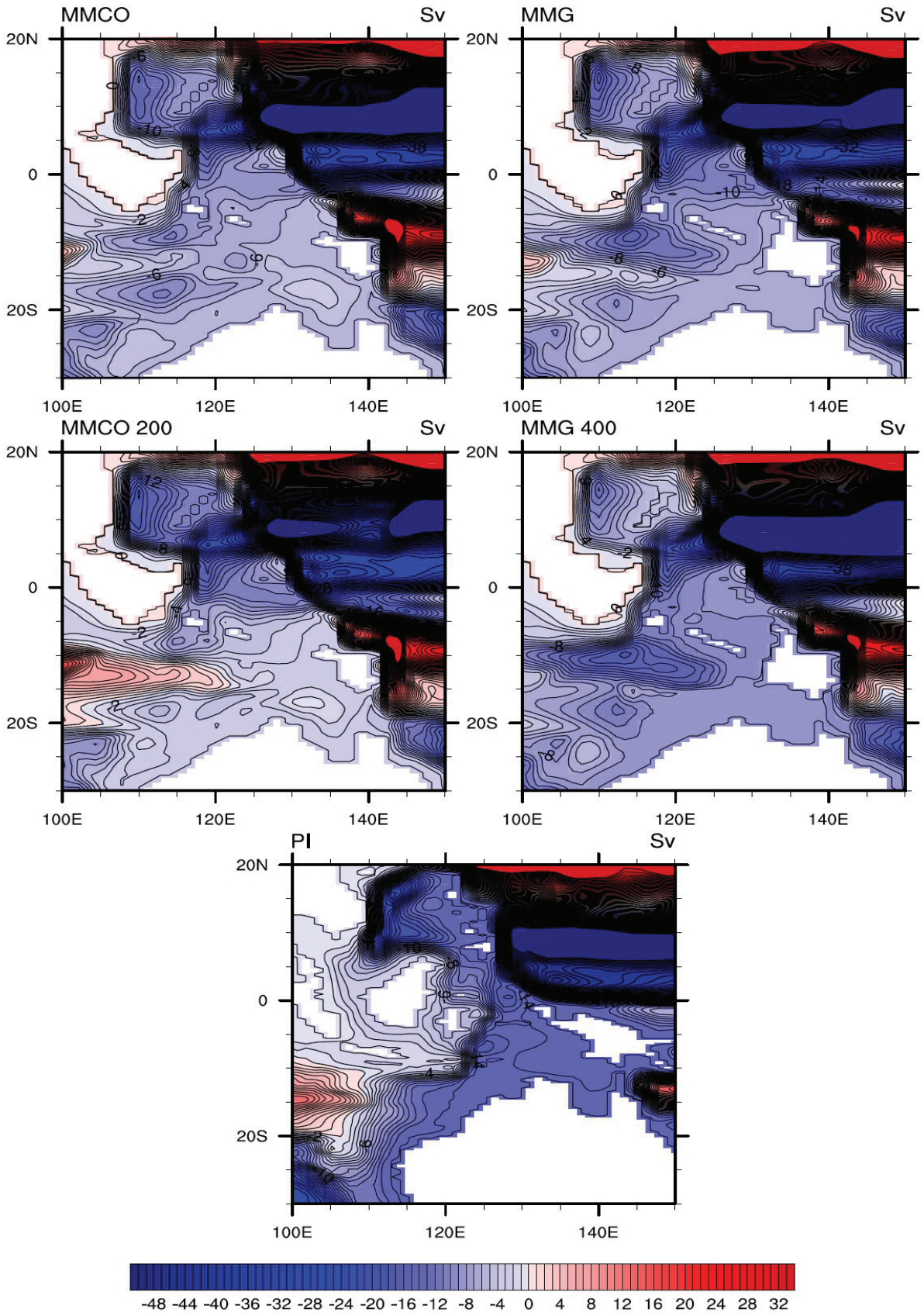

Figure 4.10. *Barotropic stream function in January at the Southeast Asian region for MMCO, MMG, MMCO200, MMG400, and PI, in Sv.*

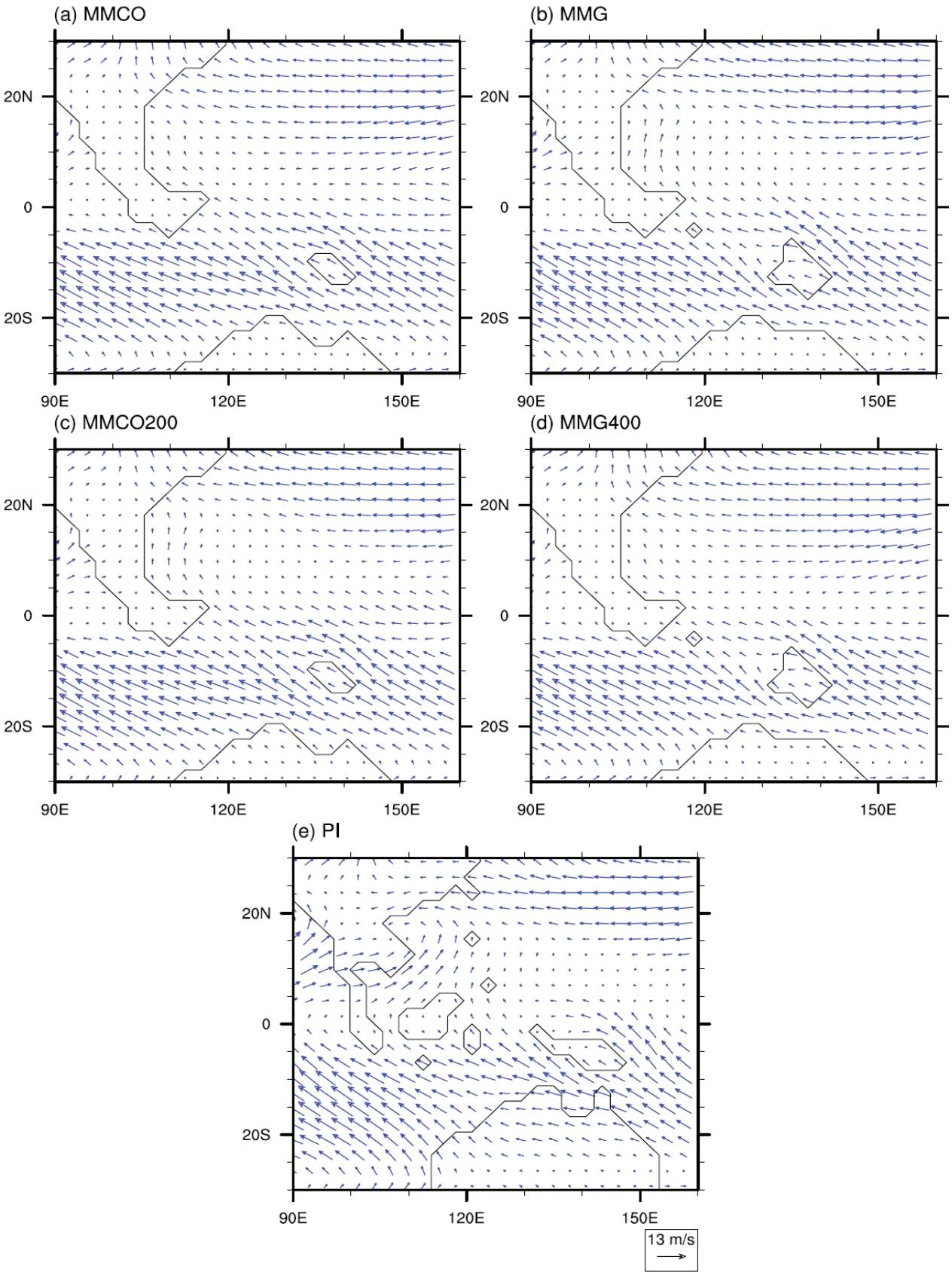

Figure 4.11. *Near-surface winds in August at the Southeast Asian region: a) MMCO, b) MMG, c) MMCO200, and d) MMG400, in m/s.*

caused by the Antarctic ice sheet forcing (Fig. 4.3.). Our monthly ITF SST values for MMG indicate a maximum in March of 29.06 °C and a minimum in September of 25.57 °C, with a seasonal cycle very similar to the PI case (Fig. 4.4.). Fossil data from a 10–13 million year old giant clam *Tridacna gigas* collected in Java suggest maximum and minimum SSTs values of 29.54 and 27.47 °C for that area (Warter et al., 2015, Batenburg et al., 2011). The maximum estimate is in good agreement with our maximum for the MMG; the minimum is though higher than our value.

4.4. Did the West Pacific Warm Pool exist during the MMCT?

The present-day WPWP constitutes the biggest warm water mass on Earth and it is usually defined by surface waters warmer than 28 °C (Yan et al., 1992). In order to explore whether a similar warm water mass existed during the Middle Miocene we calculated the mean SST values at the tropics for the different experiments. The warm colors in Fig. 4.12. correspond to the areas with SSTs warmer than the tropical mean for each experiment. Our results suggest that a similar structure to the present-day WPWP existed already at the Middle Miocene, with a similar position and extension.

4.5. Discussion

In this study a PI ITF volume transport of -17.38 Sv was modeled, a value which falls within the present-day uncertainty range suggested by Sprintall et al. (2009). The PI ITF waters are mainly of North Pacific origin. The months of highest transport are June–August, with the maximum occurring in July. Transport is lowest from November to February, with the absolute minimum occurring in December. During June–August, the cyclonic gyre under the North Pacific Gyre moves closer to the ITF region, intensifying the flow, meanwhile during the months of lowest transport this gyre is located further east. Besides, the northwest wind regime present over the Indonesian area

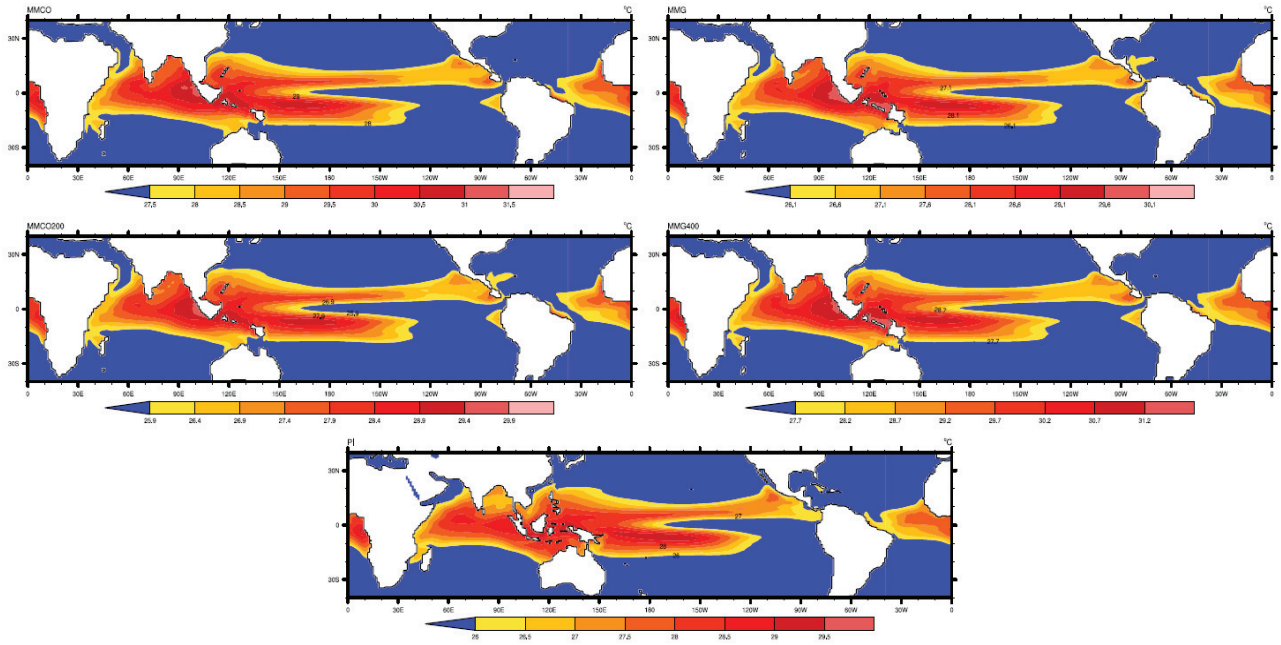

Figure 4.12. *Sea surface temperature for MMCO, MMG, MMCO200, MMG400, and PI, in °C. Warm colors indicate sea surface temperatures warmer than the tropical mean value for each experiment.*

from December to February partially blocks the flow into the Indian Ocean during those months.

For the MMCO, an ITF transport value of -13.30 Sv from the Pacific to the Indian Ocean was modeled. This estimate is consistent with a Middle Miocene Indonesian gateway open to surface and intermediate waters (Kuhnt et al., 2004), as at present-day. Our results do not support the existence of an eastward flow from the Indian to the Pacific Oceans through the Indonesian archipelago during the MMCO, in disagreement with the study by Gourlan et al. (2008) that suggests the existence of such a flow before ~ 14 Ma. Transport is highest from July to October, with the maximum occurring in August, and lowest from December to March, with the minimum occurring in January. During July–October, the region is affected by strong southeast winds, which enhance transport to the Indian Ocean through Ekman transport divergence. During those months, the ITF has both a North and a South Pacific component, although the South Pacific component is stronger due again to the influence of the southeast wind regime. During December–March,

northwest winds replace southeast winds over the region, hampering transport into the Indian Ocean through the same Ekman transport mechanism. Besides, those months, the absence of southeast winds removes the South Pacific component from the ITF.

Although no significant changes occur in the total volume transport across the Indonesian archipelago over the MMCT, changes in the waterpaths are observed. An increase in transport through the western path is modeled, which is related to the Antarctic ice sheet forcing; while flow decreases through the eastern paths, due to the sea level fall across the MMCT affecting the shallow topographic barriers of that area, and due to a weakening of the South Pacific Gyre.

Compared to PI, the Middle Miocene ITF has a stronger South Pacific component. Besides, the Middle Miocene estimates of volume transport are lower than during the PI, since although the passages were wider during the Middle Miocene, they were also shallower. Nevertheless, note that uncertainties in the Middle Miocene bathymetry are high. Finally, our results suggest that a similar structure to the present-day WPWP existed during the Middle Miocene, with a similar extension and position.

5. Conclusions and outlook

Our CCSM3 global analyses report a Middle Miocene climate warmer than PI, with mean global SSTs at the MMCO ~ 2.7 °C higher than PI. An interesting feature is the weaker ACC at the Middle Miocene, linked to the more southern position of Australia. Besides, the deep cell of the global MOC is stronger, and the upper cell weaker, and the Middle Miocene runs show decreased poleward ocean heat transport in the Northern Hemisphere and increased poleward ocean heat transport in the Southern Hemisphere.

During the MMCT, global mean SSTs cool down by 1.58 °C, due to the decrease in atmospheric CO_2. The atmosphere cools down as a consequence of the CO_2 dropdown. The ocean responds with a positive heat flux to the atmosphere, which leads to cooling of the upper ocean. The Antarctic ice sheet expansion, instead, has a very slight warming effect on mean global SSTs. The reason for this warming lies in the increased topography of Antarctica inducing decreased upwelling longwave flux at the top of the atmosphere over the Antarctic continent.

The regions presenting the most pronounced cooling of surface waters are the Southern Ocean and the northern North Pacific. Proxy evidence from the Southern Ocean reports a decrease in SSTs within our range of modeled values, suggesting that the combined effects of the CO_2 decrease and the Antarctic ice sheet expansion are sufficient to explain the cooling of surface waters reported at the MMCT.

Cooling of waters across the MMCT is not limited to the ocean surface. Ocean temperatures decrease between 1.5–2 °C at depth in most regions in our experiments, indicating that the combined effects of the CO_2 decrease and Antarctic ice sheet expansion at the MMCT can explain a larger part of the deep water cooling inferred from Mg/Ca studies (2–3 °C) (Billups and Schrag, 2002; Lear et al., 2000, 2010; Shevenell et al., 2008). The CO_2 decrease cools down the ocean

practically at all latitudes and depths and constitutes the first cause of cooling across the MMCT in our experiments.

The effect of the Antarctic ice sheet expansion on ocean temperatures depends significantly on the depth. Above ~ 1400 m depth (and at deeper levels in the Arctic Ocean) the Antarctic ice sheet expansion induces warming, while below ~ 1400 m depth it causes moderate cooling.

In the Southern Ocean, the CO_2 dropdown and the Antarctic ice sheet expansion cool down waters in the upper ocean. The cooling induced by both these two forcings is then transmitted to the ocean bottom through water convection and spread to the north as AABW. Besides, the potential density field suggests an intensification in AABW formation across the MMCT related to the salinity increase at the Antarctic coast triggered by the CO_2 forcing. This salinity increase is due to sea ice formation and to variations in the evaporation/precipitation balance. The MOC field, nevertheless, does not allow to conclude global strengthening of the deep cell across the MMCT. However, that field corresponds only to the Eulerian component of the MOC, a fact that could affect the results.

In the North Atlantic, important cooling of deep waters takes place across the MMCT. In that case, cooling is exclusively related to the CO_2 forcing. Upper ocean cooling is transmitted to deep levels through convection, which occurs both before and after the MMCT, although it intensifies across the MMCT. Convection is due to the high salinity levels of the North Atlantic and the relatively cold temperatures of the upper ocean in that area. The increase in convection across the MMCT is caused by a decrease in upper ocean temperatures and is not related to salinity changes.

Important changes in the regime of near-surface winds are observed in the Southern Hemisphere across the transition. The increased Antarctic topography causes an increase in the pressure gradient between the polar highs and subpolar lows, and between the subpolar lows and subtropical highs, which translates into strengthening of the easterlies along the Antarctic coast, and into moderate strengthening of the westerlies at 50–60° S.

Our CCSM3 analyses for the ITF area report an ITF volume transport of -13.3 Sv of water from the

Pacific to the Indian Oceans at the MMCO. Our results do not show evidence of any significant eastward flow, in contrast with the results from Gourlan et al. (2008), suggesting the existence of an eastward flow through the Indonesian archipelago from the Indian to the Pacific oceans (in addition to the westward flow), prior to ~ 14 Ma.

The modeled ITF volume transport values before and after the MMCT are almost identical. However, changes in the water-transport pathways are modeled: an increase in transport through the western path and a decrease in the eastern paths, caused by the sea level fall across the MMCT affecting the shallow barriers of the eastern paths and by a weakening of the South Pacific Gyre.

The Middle Miocene ITF has a stronger South Pacific component than the PI ITF and it transports less water, despite the wider passage, since this is also shallower. Nevertheless, uncertainties in the bathymetry are high. Finally, our results suggest the existence of a proto WPWP, with a similar extension to that of PI. The Middle Miocene ITF sub-annual variability appears strongly controlled by seasonal northwest and southeast winds as at the present-day.

As mentioned above, our results support the idea that deep water formation was occurring in the North Atlantic during the Middle Miocene and that this was strongly conditioned by the high salinity values of the Atlantic Ocean. Future studies should be aimed at investigating how the Tethys configuration contributes to the high salinity levels of the Atlantic and how those affect deep water formation in the North Atlantic. Furthermore, the role of Tethys waters as heat source in the Southern Ocean should be investigated. Moreover, a series of sensitivity studies testing the effects on ocean circulation across the MMCT of orbital configurations favorable to cold and warm conditions should be carried out. Additional scientific efforts could point at questioning the existence of an Australian-Indonesian monsoon system during the MMCT. Further research should be performed assessing the timing of development of the WPWP and its effect on atmospheric circulation.

The current study shows that a CO_2 dropdown in the range of the present-day variations might have

an important effect on global temperatures and ocean circulation. This fact should set a warning for potentially compelling effects of present-day climate change, although boundary-conditions for present-day differ significantly from those of the Middle Miocene. The larger extension of the present-day Antarctic ice sheet compared to that of the Middle Miocene might contribute to a higher degree of stability of the Antarctic ice sheet. Similarly, in the Northern Hemisphere, ice hysteresis associated with the Greenland ice sheet might partially delay climatic changes. Besides, the stronger ACC at present-day compared to the Middle Miocene might help isolate Antarctica from warming. On the other hand, the most concerning fact about present-day climate change are the high rates of atmospheric CO_2 change, unprecedented in proxy records. Although resolution of atmospheric CO_2 paleoproxy records is rather coarse, the main past climate transitions (including the MMCT) triggered by changes in atmospheric CO_2 concentrations were associated to ranges inferior to those expected if current CO_2 emissions are maintained.

Appendix A. CCSM3 setup for the Middle Miocene

Numerous adjustments needed to be applied to the CCSM3 default configuration in order to adapt it to the Middle Miocene period. These adjustments were carried out according to the NCAR CCSM3 setup guide for paleoruns by Rosenbloom et al. (2011), using the setup tools software package provided by NCAR. Below, a description of the model setup for the MMCO experiment is provided. The setup scripts for that experiment can be found in the CD attached to this thesis. The remaining Middle Miocene experiments were configured in the same way as the MMCO experiment, only the input data files (see A.1.) for the setup scripts differed from one experiment to the other.

A.1. Netcdf input data files for the setup tools package

The first step was the creation of the two netcdf files required as input files for the setup tools: a) a global topography/bathymetry file and b) a global vegetation file (both on regular lat/lon grids). The topography/bathymetry and vegetation files we employed, which were described in chapter 2, are available on PANGAEA – Data Publisher for Earth & Environmental Science at https://doi.pangaea.de/10.1594/PANGAEA.888504 under the names mmco_topo_bathy_v1_0.nc and mmco_veg_v1_0.nc.

A.2. Setup of the atmosphere component

The ncl script **ccsm_cami_create_ccsm3.ncl** provided in the NCAR setup tools package creates the initial condition file for the atmosphere. This script uses the global topography/bathymetry file to calculate surface pressure and surface geopotential. Initial temperature is based on a latitudinal

distribution for which the user needs to provide an estimate value at the equator (*TEQ*) and the pole (*TPOLE*), in °C. The following values were used in our experiment:

setenv TEQ 28.

setenv TPOLE -20.

A.3. Setup of the land component

Two important adjustments needed to be performed to the land model configuration to represent Middle Miocene conditions. The first one relates to vegetation and the second one to river routing.

The land model uses surface data containing information about plant functional types, soil color and texture, leaf/stem areas and heights, lakes and wetlands, glaciers and urban areas. These surface data are created by the **paleo_mkraw_sed.F90** fortran file provided in the setup tools package, which requires the global vegetation netcdf file, mmco_veg_v1_0.nc, as input. The vegetation data in the global vegetation file must be provided in the biome scheme of the Land Surface Model (LSM) (Bonan, 1996).

For a land/sea distribution different from present-day, the river paths, which are very important in terms of runoff to the ocean, must be modified. The river routing data are required to run the River Transport Model (RTM), a submodel within the land component, and can be created with the NCAR CCSM3 setup tools based on topography gradients. The code required for their creation is named **topo2rdirc_sed.F90** and it produces two different output files: fort.10 and fort.11 (ASCII format). Fort.10 contains the river routing data, meanwhile fort.11 contains the list of closed water paths (or loops) inside the fort.10 file. The fort.10 file needs to be manually and iteratively corrected until all loops are eliminated, otherwise salinity imbalances would be present in the model experiments at run time.

A.4. Setup of the ocean and sea ice components

As it was mentioned in the model description section (sect. 2.1.), a customized ocean grid was used instead of the default x1 dipole grid, in order to accommodate the changes in the bathymetry off West Antarctica. Our customized ocean grid is also a dipole grid with 384 points in latitude and 320 points in longitude, although extended to ~ 87° S. Additionally, also the ocean bathymetry file, named kmt file, needed to be recreated. The kmt file associates a depth level to each grid point. The creation of a new grid always requires the creation of a new kmt file since the kmt data are geographically referenced. Besides, the Middle Miocene global ocean bathymetry and coastline differ substantially from the present-day one, another reason why the default kmt file could not be used. Both the ocean grid and the kmt files are binary files created by the **mk_grid.csh** c-shell script through fortran code. The c-shell script and the fortran code are provided in the CCSM3 setup tools package. Below, the values of the main parameters in the **mk_grid.csh** c-shell script are provided:

set lonnp = -38.5 *# longitude of the ocean grid North Pole*

set latnp = 72.5 *# latitude of the ocean grid North Pole*

set lonsp = 1.1 *# longitude of the ocean grid South Pole*

set latsp = -90 *# latitude of the ocean grid South Pole*

set nlatn = 197 *# number of j grid lines in the Northern Hemisphere*

set nlats = 187 *# number of j grid lines in the Southern Hemisphere*

set nx = 320 *# number of i grid lines*

set nz = 40 *# number of vertical grid levels*

set vrtgrid = gx1v3_vert_grid *# ascii vertical grid input file*

set dyeq = 0.25 *# meridional grid spacing at the equator (in degrees)*

set dsig = 20 *# Gaussian e-folding scale at equator*

set jcon = 45 *# rows of constant meridional grid spacing at poles*

set popgrid = grid.mmco.pop.da *# name of the output binary grid file*

set kmtgrid = kmt.mmco.da *# name of the output binary kmt file*

Notes: 1) the ocean grid North Pole is located over Greenland and the ocean grid South Pole coincides with the geographic South Pole, 2) *nlatn* + *nlats* = 384 and represents the total number of j grid points, 3) the meridional grid spacing at the equator (*dyeq*) is set to 0.25°, 4) the Gaussian e-folding scale at the equator (*dsig*) is set to 20, 5) the number of rows of constant meridional grid spacing at the poles (*jcon*) to 45, and 6) the vertical grid employed (*vrtgrid*) is the default gx1v3 vertical grid.

After running the **mk_grid.csh** script, the kmt file, kmt.mmco.da, needed to be corrected. The model is not able to calculate fluxes over narrow passages. For this reason, narrow channels and bays in the kmt file needed to be either removed or widened manually.

A.5. Setup of the coupler component

The exchange of information between the different model components during run time is hampered by the different grids used by these model components. The mapping files indicate how the information must be transferred between different grids. Since a customized ocean grid was used in our Middle Miocene experiments, not the default ocean grid, the mapping files between the ocean and the atmosphere components needed to be recreated.

The atmosphere/ocean mapping files are created by the **mk_remap.csh** c-shell script provided in the model setup tools. This script uses the fortran code **myconvertPOPT.f90** and the SCRIP software package (version 1.4) (Jones, 1998). Some important input parameters that must be

provided within the script **mk_remap.csh** are described below:

```
set nx      = 320                    # number of longitude grid points in the ocean grid
set ny      = 384                    # number of latitude grid points in the ocean grid
set popgrid = grid.mmco.pop.da       # ocean grid file in binary format (created at point A.4)
set kmtgrid = kmt.mmco.da            # kmt file in binary format (created at point A.4)
set atmgridfile = T42_001005.nc      # default atmosphere grid (T42) in netcdf format
                                     # available from the setup tools package
```

The RTM, although being part of the land component, uses its own grid. Again, since a customized ocean grid was used in our Middle Miocene experiments, the mapping file of the river runoff fluxes to the ocean needed to be recreated. This can be done with the **mk_runoff_remap.csh** c-shell script, which uses the SCRIP software, as does **mk_remap.csh**. Below, the most important input parameters of this script are presented:

```
set ocngridfile = ocngridfile.nc          # this netcdf file is created by the script
                                          # mk_remap.csh
                                          # using information about the ocean grid
set lndgridfile = remap_grid_ll2.0deg_CLM.nc  # RTM grid available from the setup tools package
                                          # the 2°x 2° resolution was used.
```

Appendix B. Global vegetation distribution during the Middle Miocene

B.1. Europe

The most widespread biome in the middle latitudes of Europe during the Langhian was the *warm-temperate evergreen broadleaf and mixed forest* (*"warm mixed forest"*) (Pound et al., 2012). On the southern and eastern coast of Spain however, drier biomes such as *temperate xerophytic shrubland* (*"evergreen shrub land"/"deciduous shrub land"*) or *temperate deciduous broadleaf savanna* (*"deciduous shrub land"*) were present (Pound et al., 2012) (Fig. 2.5.). The vegetation patterns of the Serravallian were similar to those of the Langhian. However, some drying and/or cooling occurred. In east Europe, for example, the data by Pound et al. (2012) indicate the emergence of *temperate deciduous broadleaf savanna* (*"deciduous shrub land"*). These drier and/or cooler biomes developed during the Serravallian were neglected for simplification in the current reconstructions.
Evidence for the Middle Miocene European high northern latitudes (above 60° N) is missing in Pound et al. (2012). This region was painted with *mixed coniferous forest* (*"cool mixed forest"*) (Fig. 2.5.) in the current MMCO and MMG reconstructions based on Wolfe's (1985) Early Miocene data. We also filled the Alpine area with *mixed coniferous forest* (*"cool mixed forest"*) according to Wolfe (1985).

B.2. Asia

The Asian high northern latitudes were assigned *"cool mixed forest"* in the current MMCO and MMG reconstructions (Fig. 2.5.). Pound et al. (2012) suggest *cool-temperate mixed forest* (*"cool mixed forest"*) to have been the dominant biome in the eastern Asian high northern latitudes during the Middle Miocene. No data are provided for the western Asian high northern latitudes in Pound et al. (2012). Wolfe's (1985) reconstruction suggests two different vegetation patterns for the western Asian high northern latitudes during the Early Miocene, corresponding to north and south. For

simplification, only the northern pattern, consisting of *mixed coniferous forest* (*"cool mixed forest"*), was considered in the current reconstructions.

The western Asian middle latitudes were filled with *"warm mixed forest"* (Fig. 2.5.). Pound et al. (2012) propose a "south to north drying and cooling trend" for that region during the Middle Miocene, starting with *warm-temperate evergreen broadleaf and mixed forest* (*"warm mixed forest"*) in the southern part and ending with *temperate deciduous broadleaf savanna* (*"deciduous shrub land"*) in the northern part. For simplification, only the *warm-temperate evergreen broadleaf and mixed forest* (*"warm mixed forest"*) was considered in our current MMCO and MMG boundary conditions.

The Himalayas and the Tibetan Plateau were assigned *mixed coniferous forest* (*"cool mixed forest"*) based on Wolfe's (1985) reconstruction.

The eastern Asian middle latitudes were mainly populated by *warm-temperate evergreen broadleaf and mixed forest* (*"warm mixed forest"*) during the Middle Miocene (Pound et al., 2012) (Fig. 2.5.). Along the coast at ~ 32° N, there was a *tropical evergreen broadleaf forest* (*"tropical broadleaf evergreen forest"*), and west of 111° E a drier region containing biomes such as *temperate xerophytic shrubland* (*"evergreen shrub land"/"deciduous shrub land"*) (Pound et al., 2012). This drier region was dismissed for simplification in our MMCO and MMG reconstructions.

Tropical evergreen broadleaf forest (*"tropical broadleaf evergreen forest")* was the dominant biome in India and Southeast Asia during the Middle Miocene (Pound et al., 2012) (Fig. 2.5.).

B.3. Australia and New Zealand

Tropical evergreen broadleaf forest (*"tropical broadleaf evergreen forest")* was present in northeast Australia during the Middle Miocene (Pound et al., 2012) (Fig. 2.5.). Also in the east, but south of 28° S, *warm-temperate evergreen broadleaf and mixed forest* (*"warm mixed forest"*) was present (Pound et al., 2012).

In Pound et al. (2012) the description of Australia is limited to the east side. A line of *megathermal*

rain forest (*"tropical broadleaf evergreen forest"*) was assigned along the north coast in the current reconstructions based on Morley's (2011) Middle Miocene data.

Wolfe's (1985) Early Miocene reconstruction suggests the vegetation patterns of east Australia to be also representative for central Australia. Assuming this would still be valid during the Middle Miocene, the *"warm mixed forest"* assigned to east Australia in the current reconstructions, was extended to central Australia.

Wolfe's (1985) data further suggest similar vegetation patterns for west Australia and the southern coast of Spain during the Early Miocene. Assuming this analogy to be still valid during the Middle Miocene, west Australia was filled with "*evergreen shrub land"/"deciduous shrub land"*, which is the vegetation assigned to the southern coast of Spain in the current MMCO and MMG reconstructions.

Warm-temperate evergreen broadleaf and mixed forest (*"warm mixed forest"*) occupied New Zealand during the Middle Miocene (Pound et al., 2012) (Fig. 2.5.).

B.4. Antarctica

There is evidence for *low- and high-shrub tundra* and *prostrate dwarf-shrub tundra* (*"tundra"*) at the Antarctic margins during the Langhian (Pound et al., 2012). By the Serravallian, practically no vegetation was present on Antarctica (Pound et al., 2012). In the current MMCO and MMG reconstructions *"tundra"* was assigned to the ice-free regions, in consistence with the ice sheet geometries described above (Fig. 2.5.).

B.5. Africa and the Arabian Peninsula

Africa and the Arabian Peninsula have poor data coverage in Pound et al. (2012). Evidence from Pound et al. (2012) for the most northern part of Africa for the Middle Miocene is restricted to one site (in Tunisia), suggesting a *warm-temperate evergreen broadleaf and mixed forest* (*"warm mixed forest"*). That data site was dismissed in our current MMCO and MMG reconstructions, in view of

the inappropriateness to extrapolate data from only one site to the whole surrounding region. Instead, the most northern part of Africa was set to *"evergreen shrub land"/"deciduous shrub land"* (Fig. 2.5.). Wolfe's (1985) Early Miocene reconstruction suggests similar vegetation patterns for that region as for the southern coast of Spain. Assuming these two regions kept similar vegetation patterns also during the Middle Miocene, *"evergreen shrub land"/"deciduous shrub land"*, the vegetation assigned to the southern coast of Spain in the current MMCO and MMG reconstructions, was also assigned to the most northern part of Africa. Also a narrow belt of *megathermal rain forest* (*"tropical broadleaf evergreen forest"*) was set along the northwest coast, in agreement with Morley's (2011) Middle Miocene reconstruction.

Madagascar was assigned *megathermal rain forest* (*"tropical broadleaf evergreen forest"*), following Morley (2011). Also based on Morley's (2011) reconstruction, an area of *megathermal rain forest* (*"tropical broadleaf evergreen forest")* was defined along the south and southeast coast of southern Africa. Pound et al. (2012) suggest that drier tropical biomes, e.g. *tropical savanna* (*"savanna"*), were present close to the southern coast of southern Africa during the Middle Miocene. These drier biomes were dismissed for simplification in our MMCO and MMG boundary conditions.

Still in southern Africa, north of the *"tropical broadleaf evergreen forest"* line, a region of *"warm mixed forest"* was assigned. Wolfe (1985) suggests similar vegetation patterns for that region and for southeast Australia during the Early Miocene. Assuming those two regions kept similar vegetation patterns also during the Middle Miocene, *"warm mixed forest",* the biome set for southeast Australia in the current MMCO and MMG reconstructions, was also assigned to that region.

The remaining areas of Africa and the Arabian Peninsula were assigned *"tropical broadleaf evergreen forest"*, although we are aware that this is probably too broad for a characterization, as also drier tropical biomes were present. Wolfe (1985) suggests that *tropical rain forest* (*"tropical*

broadleaf evergreen forest") and other drier tropical biomes populated that region during the Early Miocene. Pound et al. (2012) show occurrence of *tropical evergreen broadleaf forest* (*"tropical broadleaf evergreen forest"*) in equatorial Africa during the Middle Miocene, although combined with drier tropical biomes like *tropical deciduous broadleaf forest and woodland* (*"tropical broadleaf deciduous forest"*) or *tropical savanna* (*"savanna"*). On the Arabian Peninsula, a single site indicates *tropical deciduous broadleaf forest and woodland* (*"tropical broadleaf deciduous forest"*) existed in that area during the Langhian (Pound et al., 2012). These drier tropical biomes were dismissed for simplification in our boundary conditions.

B.6. North America and Greenland

During the Middle Miocene, the western North American high latitudes were populated with *cool-temperate mixed forest* (*"cool mixed forest"*) (Pound et al., 2012) (Fig. 2.5.). Evidence for the eastern North American high latitudes is missing in Pound et al. (2012). Wolfe (1985) suggests two different patterns for the eastern North American high latitudes during the Early Miocene, at ~ 60° – 65° N and north of ~ 65° N, respectively. For simplification only the most northern pattern, *mixed coniferous forest* (*"cool mixed forest"*), was considered in the current MMCO and MMG reconstructions.

During the Langhian, *warm-temperate evergreen broadleaf and mixed forest* (*"warm mixed forest"*) was prevalent in the western North American middle latitudes above 40° N (Pound et al., 2012). South of 40° N a drier region existed, with biomes such as *temperate xerophytic shrubland* (*"evergreen shrub land"/"deciduous shrub land"*) (Pound et al., 2012) (Fig. 2.5.). During the Serravallian, the western North American middle latitudes became more heterogeneous in terms of vegetation, an amalgam of *warm-temperate evergreen broadleaf and mixed forest* (*"warm mixed forest"*) combined with other drier and/or cooler biomes (Pound et al., 2012). For simplification, the Langhian pattern was used in both MMCO and MMG reconstructions.

The Rocky Mountains were set to *mixed coniferous forest* (*"cool mixed forest"*) following Wolfe

(1985).

The central North American middle latitudes were assigned *"warm mixed forest"* in the current MMCO and MMG reconstructions based on Wolfe (1985). That region has scarce data coverage in Pound et al. (2012) (one Langhian site, two Serravallian sites). Wolfe (1985) suggests two different patterns for the central North American middle latitudes during the Early Miocene, corresponding to south and north. For the southern part, Wolfe (1985) suggests similar vegetation patterns as for southeast Australia (assigned *"warm mixed forest"* here), and for the northern part, similar vegetation patterns as for the European middle latitudes (assigned *"warm mixed forest"* here).

However, the central North American middle latitudes were not exclusively vegetated by *"warm mixed forest"* during the Middle Miocene. Wolfe (1985) suggests the presence of "at least some interfluve grassland" in areas such as Nebraska during the late Middle Miocene. Besides, Pound et al. (2012) show some evidence for the presence of *temperate grassland* (*"cool grassland"*) (Langhian) and *temperate deciduous broadleaf savanna* (*"deciduous shrub land"*) (Serravallian) in the central American middle latitudes during the Middle Miocene. These biomes were, however, dismissed for simplification in our current reconstructions.

The eastern North American middle latitudes were also assigned *"warm mixed forest"* in the current MMCO and MMG reconstructions. Pound et al. (2012) suggest *warm-temperate evergreen broadleaf and mixed forest* (*"warm mixed forest"*) existed in eastern North America between 29° N and 39° N, both during the Langhian and the Serravallian. However, outside that interval of latitude no data were available from Pound et al. (2012). Since Wolfe (1985) suggests similar vegetation patterns for the central and eastern North American middle latitudes during the Early Miocene, assuming this analogy would still be valid during the Middle Miocene, *"warm mixed forest"* was also applied to the east, north of 39° N and south of 29° N.

No Middle Miocene data were available for Greenland from Pound et al. (2012). North Greenland was filled with *mixed coniferous forest* (*"cool mixed forest"*) in our current reconstructions based on

Wolfe (1985). South Greenland was assigned *"warm mixed forest"*, given its similar latitudinal position and relative geographic proximity with Iceland, where *warm-temperate evergreen broadleaf and mixed forest* (*"warm mixed forest"*) existed during the Middle Miocene according to Pound et al. (2012).

B.7. Central America and south Mexico

Central America and southern Mexico were assigned *"tropical broadleaf evergreen forest"* (Fig. 2.5.). Morley (2011) suggests *megathermal rain forest* (*"tropical broadleaf evergreen forest"*) populated that region in the Middle Miocene. Pound et al. (2012) suggest that the *tropical evergreen broadleaf forest* (*"tropical broadleaf evergreen forest"*) coexisted with drier tropical biomes (Langhian) and with temperate biomes (Langhian and Serravallian), and proposes altitude as an explanation for the presence of temperate biomes in that region during the Middle Miocene. The drier tropical biomes and the temperate biomes were dismissed in our current MMCO and MMG reconstructions for simplification.

B.8. Northern South America

In northern South America, the northern half and the east were filled with *"tropical broadleaf evergreen forest"* in our reconstructions (Fig. 2.5.). Pound et al. (2012) suggest *tropical evergreen broadleaf forest* (*"tropical broadleaf evergreen forest"*) as the main biome in that region during the Langhian and Serravallian. Nevertheless, they also show evidence for some *tropical deciduous broadleaf forest and woodland* (*"tropical broadleaf deciduous forest"*) in that region during the Serravallian. Morley (2011) suggests the presence of *megathermal rain forest ("tropical broadleaf evergreen forest"*) and *monsoonal megathermal forest* (*"tropical broadleaf deciduous forest"*) in that region during the Middle Miocene. The "*tropical broadleaf deciduous forest"* was neglected for simplification in our boundary conditions.

No data were available from Pound et al. (2012) or Morley (2011) for the southwestern part of northern South America. Within that area, the Andes were assigned *"warm mixed forest"* and the rest *"tropical broadleaf evergreen forest"*. For the Early Miocene Andes, Wolfe (1985) suggests similar vegetation patterns as for the most southern part of southern South America. Since significant uplift of the Andes would have started only in the late Miocene (Ghosh et al., 2006), we considered reasonable to assume that these regions kept similar vegetation patterns also during the Middle Miocene. In this way, *"warm mixed forest"*, the biome set in our data for the most southern part of South America (see below), was also assigned to the Andes. Surrounding the Andes there is another area with non-tropical biomes in Wolfe's (1985) reconstruction, which was dismissed here for simplification. The rest of southwest northern South America is occupied by *tropical rain forest* and *paratropical rain forest* (*"tropical broadleaf evergreen forest"*) in Wolfe's (1985) reconstruction.

B.9. Southern South America

During the Middle Miocene, in the northwest of southern South America, there was a region covered by arid biomes such as *temperate xerophytic shrubland* (*"evergreen shrub land"/"deciduous shrub land"*) (Pound et al., 2012) (Fig. 2.5.).

In the northeast, along the coast, a narrow belt of *megathermal rain forest* (*"tropical broadleaf evergreen forest"*) was present according to Morley's (2011) Middle Miocene reconstruction.

No evidence from Pound et al. (2012) or Morley (2011) was available for the area between the arid region in the west and the *"tropical broadleaf evergreen forest"* in the east. East of the arid region, for the area corresponding to the Andes, Wolfe (1985) proposes similar vegetation patterns for the Early Miocene as for the most southern part of southern South America. Assuming these two areas kept similar vegetation patterns also during the Middle Miocene, *"warm mixed forest"*, the biome set in the current MMCO and MMG reconstructions for the most southern part of southern South

America (see below), was also assigned to that part of the Andes. For the region east of the Andes, for the Early Miocene, Wolfe (1985) proposes a vegetation pattern similar to that of southeast Australia. Assuming this analogy kept being valid also during the Middle Miocene, *"warm mixed forest"*, the biome set in the current Middle Miocene reconstructions for southeast Australia, was assigned to that region.

The south of southern South America was filled with *"warm mixed forest"* in our MMCO and MMG reconstructions (Fig. 2.5.). Pound et al. (2012) shows evidence for *warm-temperate evergreen broadleaf and mixed forest* (*"warm mixed forest"*) mixed with *temperate grassland* (*"cool grassland"*) south of 35° S, and again for *warm-temperate evergreen broadleaf and mixed forest* (*"warm mixed forest"*) at 55° S. The *temperate grassland* (*"cool grassland"*) south of 35° S was dismissed here for simplification.

Acknowledgements

This research was part of the Marie Curie Initial Training Network THROUGHFLOW, funded by the E.U. 7th Framework Programme on Research, Technological Development and Demonstration. The CCSM3 simulations were performed on the Cray XC30/40 supercomputer of the Norddeutscher Verbund für Hoch- und Höchstleistungsrechnen (HLRN).

First of all I would like to thank my supervisors Prof. Dr. Michael Schulz and Dr. Matthias Prange for their scientific guidance, constructive feedback, and encouragement throughout these years.

A special thanks goes to (A.) Gabriel Gaus (HLRN) for his assistance in the execution of the model runs and technical advice, with further acknowledge to Lars Nerger (HLRN). I am particularly grateful to Robert Hall, David Pollard, Matthew Pound, and Nicholas Herold for their contributions in the assemblage of Middle Miocene boundary conditions. I also want to acknowledge Lydie Dupont, Sandra Passchier and Matthew Huber for that. I am grateful to Gary Strand, Sam Levis, Esther Brady, Stephen Yeager, and very specially Nan Rosenbloom (NCAR) for their help in the Middle Miocene CCSM3 setup procedure. I would like to thank my geomodeling group colleagues, specially Thejna Tharammal (who additionally proof-read parts of my thesis), Ute Merkel, Rima Rachmayani, and Gerlinde Jung for their help regarding CCSM3 and/or the data analyses, and Andreas Manschke for the IT support. Thanks to Hanno Keil for his introduction to ArcGIS. Thanks to Alexandra-Jane Henrot and Petra Langebroek for their constructive reviews of my first manuscript. I am grateful to the THROUGHFLOW project network for the interdisciplinary exchange, to the Bremen International Graduate School for Marine Sciences GLOMAR for the useful courses that helped improving my skills, and for providing me with a thesis committee (formed by my supervisors and Ursula Röhl and Gerlinde Jung).

Finally I would like to thank my family, specially my parents (gràcies!), the sushi chicks, les floretes, la happy house, my neighbors Jose and Dolors, my friends from FME, Pep, my northern

friends Detlef, Carla, Eef, Hilla, Nico, Jonas, Mayo, Mira, Jan, Mariem, Will, Ute, Kaveh, Gesa, Simon, Lotte, Malin, Michel, Daniele, and Francesco, and all the others spread around the world (e.g. Gianluca B., Ingo, Guillem, Maria, Gianluca R.), for being there.

Bibliography

Batenburg, S. J., Reichart, G.-J, Jilbert, T., Janse, M., Wesselingh, F. P., and Renema, W.: Interannual climate variability in the Miocene: High resolution trace element and stable isotope ratios in giant clams, Palaeogeogr. Palaeocl. 306, 75–81, https://doi.org/10.1016/j.palaeo.2011.03.031, 2011.

Billups, K. and Schrag, D. P.: Paleotemperatures and ice volume of the past 27 Myr revisited with paired Mg/Ca and $^{18}O/^{16}O$ measurements on benthic foraminifera, Paleoceanography, 17, 1003, https://doi.org/10.1029/2000PA000567, 2002.

Billups, K. and Schrag, D. P.: Application of benthic foraminiferal Mg/Ca ratios to questions of Cenozoic climate change, Earth Planet. Sc. Lett., 209, 181–195, https://doi.org/10.1016/S0012-821X(03)00067-0, 2003.

Bonan, G. B.: A Land Surface Model (LSM Version 1.0) for Ecological, Hydrological, and Atmospheric Studies: Technical Description and User's Guide, NCAR Technical Note NCAR/TN–417+STR, National Center for Atmospheric Research, Boulder, Colorado, 1–150, https://doi.org/10.5065/D6DF6P5X, 1996.

Bonan, G. B., Levis, S., Kergoat, L., and Oleson, K.W.: Landscapes as patches of plant functional types: An integrating concept for climate and ecosystem models, Global Biogeochem. Cy., 16, 1021, https://doi.org/10.1029/2000GB001360, 2002.

Briegleb, B. P., Bitz, C. M., Hunke, E. C., Lipscomb, W. H., Holland, M., Schramm, J. L., and Moritz, R. E.: Scientific Description of the Sea Ice Component in the Community Climate System Model, Version 3, NCAR Technical Note NCAR/TN–463+STR, National Center for Atmospheric Research, Boulder, Colorado, https://doi.org/10.5065/D6HH6H1P, 2004.

Butzin, M., Lohmann, G., and Bickert, T.: Miocene ocean circulation inferred from marine carbon cycle modeling combined with benthic isotope records, Paleoceanography, 26, PA1203,

https://doi.org/10.1029/2009PA001901, 2011.

Cane, M. A. and Molnar, P.: Closing of the Indonesian seaway as a precursor to east African aridification around 3–4 million years ago, Nature, 411, 157–162, https://doi.org/10.1038/35075500, 2001.

Collins, W. D. and coauthors: Description of the NCAR Community Atmosphere Model (CAM 3.0), NCAR Technical Note NCAR/TN–464+STR, National Center for Atmospheric Research, Boulder, Colorado, 1–214, https://doi.org/10.5065/D63N21CH, 2004.

Collins, W. D., Bitz, C. M., Blackmon, M. L., Bonan, G. B., Bretherton, C.S., Carton, J. A., Chang, P., Doney, S. C., Hack, J. J., Henderson, T. B., Kiehl, J. T., Large, W. G., McKenna, D. S., Santer, B. D., and Smith, R. D.: The Community Climate System Model Version 3 (CCSM3), J. Climate, 19, 2122–2143, https://doi.org/10.1175/JCLI3761.1, 2006.

De Boer, B., Van De Wal, R. S. W., Bintanja, R., Lourens, L. J., and Tuenter, E.: Cenozoic global ice-volume and temperature simulations with 1-D ice-sheet models forced by benthic $\delta^{18}O$ records, Ann. Glaciol., 51, 23–33, https://doi.org/10.3189/172756410791392736, 2010.

DeConto, R. M., Pollard, D., Wilson, P. A., Paelike, H., Lear, C. H., and Pagani, M.: Thresholds for Cenozoic bipolar glaciation, Nature, 455, 652–656, https://doi.org/10.1038/nature07337, 2008.

Duque-Caro, H.: Neogene stratigraphy, paleoceanography and paleobiogeography in northwest South America and the evolution of the Panama seaway, Palaeogeogr. Palaeocl., 77, 203–234, https://doi.org/10.1016/0031-0182(90)90178-A, 1990.

Eagles, G. and Jokat, W.: Tectonic reconstructions for paleobathymetry in Drake Passage, Tectonophysics, 611, 28–50, http://dx.doi.org/10.1016/j.tecto.2013.11.021, 2014.

England, M. H., Hutchinson, D. K., Santoso, A., and Sijp, W. P.: Ice–Atmosphere Feedbacks Dominate the Response of the Climate System to Drake Passage Closure, J. Climate, 30, 5775–5790, https://doi.org/10.1175/JCLI-D-15-0554.1, 2017.

Fairbanks, R. G. and Matthews, R. K.: The marine oxygen isotope record in Pleistocene coral, Barbados, West Indies, Quat. Res., 10, 181–196, https://doi.org/10.1016/0033-5894(78)90100-X, 1978.

Flower, B. P. and Kennett, J. P.: The middle Miocene climatic transition: East Antarctic ice sheet development, deep ocean circulation and global carbon cycling, Palaeogeogr. Palaeocl., 108, 537–555, https://doi.org/10.1016/0031-0182(94)90251-8, 1994.

Foster, G. L., Lear, C. H., and Rae, J. W. B.: The evolution of pCO_2, ice volume and climate during the middle Miocene, Earth Planet. Sc. Lett., 341–344, 243–254, https://doi.org/10.1016/j.epsl.2012.06.007, 2012.

Gallagher, S. J., Wallace, M. W., Li, C. L., Kina, B., Bye, J. T., Akimoto, K., and Torii, M.: Neogene history of the West Pacific Warm Pool, Kuroshio and Leeuwin currents, Paleoceanography, 24, PA1206, https://doi.org/10.1029/2008PA001660, 2009.

Gasson, E., DeConto, R. M., Pollard, D., and Levy, R. H.: Dynamic Antarctic ice sheet during the early to mid-Miocene, P. Natl. Acad. Sci. USA, 113, 3459–3464, https://doi.org/10.1073/pnas.1516130113, 2016.

Ghosh, P., Garzione, C. N., and Eiler, J. M.: Rapid Uplift of the Altiplano Revealed Through ^{13}C–^{18}O Bonds in Paleosol Carbonates, Science, 311, 511–515, https://doi.org/10.1126/science.1119365, 2006.

Goldner, A., Herold, N., and Huber, M.: Antarctic glaciation caused ocean circulation changes at the Eocene–Oligocene transition, Nature, 511, 574–577, https://doi.org/10.1038/nature13597, 2014.

Gordon, A. L.: Oceanography of the Indonesian seas and their throughflow, Oceanography, 18, 14–27, https://doi.org/10.5670/oceanog.2005.01, 2005.

Gordon, A. L., Giulivi, C. F., and Ilahude, A. G.: Deep topographic barriers within the Indonesian seas, Deep-Sea Res. Pt. II, 50, 2205–2228, https://doi.org/10.1016/S0967-

0645(03)00053-5, 2003a.

Gordon, A. L., Susanto, R. D., and Vranes, K.: Cool Indonesian throughflow as a consequence of restricted surface layer flow, Nature, 425, 824–828, https://doi.org/10.1038/nature02038, 2003b.

Gourlan, A. T., Meynadier, L., and Allègre, C. J.: Tectonically driven changes in the Indian Ocean circulation over the last 25 Ma: Neodymium isotope evidence, Earth and Planetary Science Letters, 267, 353–364, https://doi.org/10.1016/j.epsl.2007.11.054, 2008.

Greenop, R., Foster, G. L., Wilson, P. A., and Lear, C. H.: Middle Miocene climate instability associated with high-amplitude CO_2 variability, Paleoceanography, 29, 845–853, https://doi.org/10.1002/2014PA002653, 2014.

Groeneveld, J., Henderiks, J., Renema, W., McHugh, C. M., De Vleeschouwer, D., Christensen, B. A., Fulthorpe, C. S., Reuning, L., Gallagher, S. J., Bogus, K., Auer, G., Ishiwa, T., and Expedition 356 Scientists: Australian shelf sediments reveal shifts in Miocene Southern Hemisphere westerlies, Sci. Adv., 3, 1–9, https://doi.org/10.1126/sciadv.1602567, 2017.

Hall, R: Sundaland and Wallacea: geology, plate tectonics and palaeogeography, in: Biotic Evolution and Environmental Change in Southeast Asia, edited by: Gower, D. J., Richardson, J. E., Rosen, B. R., Rueber, L., and Williams, S. T., Cambridge University Press, 32–78, 2012.

Hamon, N., Sepulchre, P., Lefebvre, V., and Ramstein, G.: The role of eastern Tethys seaway closure in the Middle Miocene Climatic Transition (ca. 14 Ma), Clim. Past, 9, 2687–2702, https://doi.org/10.5194/cp-9-2687-2013, 2013.

Haq, B. U., Hardenbol, J., and Vail, P. R.: Chronology of Fluctuating Sea Levels Since the Triassic, Science, 235, 1156–1167, https://doi.org/10.1126/science.235.4793.1156, 1987.

Henrot, A.-J., Utescher, T., Erdei, B., Dury, M., Hamon, N., Ramstein, G., Krapp, M., Herold, N., Goldner, A., Favre, E., Munhoven, G., and François, L.: Middle Miocene climate and vegetation models and their validation with proxy data, Palaeogeogr. Palaeocl., 467, 95–119,

https://doi.org/10.1016/j.palaeo.2016.05.026, 2017.

Herold, N., Seton, M., Müller, R. D., You, Y., and Huber, M.: Middle Miocene tectonic boundary conditions for use in climate models, Geochem. Geophy. Geosy., 9, Q10009, https://doi.org/10.1029/2008GC002046, 2008.

Herold, N., Müller, R., and Seton, M.: Comparing early to middle Miocene terrestrial climate simulations with geological data, Geosphere, 6, 952–961, https://doi.org/10.1130/GES00544.1, 2010.

Herold, N., Huber, M., and Müller, R. D.: Modeling the miocene climatic optimum. Part I: Land and atmosphere, J. Climate, 24, 6353–6372, https://doi.org/10.1175/2011JCLI4035.1, 2011.

Herold, N., Huber, M., Müller, R. D., and Seton, M.: Modeling the Miocene climatic optimum: Ocean circulation, Paleoceanography, 27, PA1209, https://doi.org/10.1029/2010PA002041, 2012.

Holbourn, A., Kuhnt, W., Schulz, M., and Erlenkeuser, H.: Impacts of orbital forcing and atmospheric carbon dioxide on Miocene ice-sheet expansion, Nature, 438, 483–487, https://doi.org/10.1038/nature04123, 2005.

Holbourn, A., Kuhnt, W., Schulz, M., Flores, J. A., and Andersen, N.: Orbitally-paced climate evolution during the middle Miocene “Monterey” carbon-isotope excursion, Earth Planet. Sc. Lett., 261, 534–550, https://doi.org/10.1016/j.epsl.2007.07.026, 2007.

Holbourn, A., Kuhnt, W., Regenberg, M., Schulz, M., Mix, A., and Andersen, N.: Does Antarctic glaciation force migration of the tropical rain belt?, Geology, 38, 783–786, https://doi.org/10.1130/G31043.1, 2010.

Holbourn, A., Kuhnt, W., Frank, M., and Haley B. A.: Changes in Pacific Ocean circulation following the Miocene onset of permanent Antarctic ice cover, Earth and Planetary Science Letters, 365, 38–50, https://doi.org/10.1016/j.epsl.2013.01.020, 2013.

John, C. M., Karner, G. D., Browning, E., Leckie, R. M., Mateo, Z., Carson, B., and Lowery,

C.: Timing and magnitude of Miocene eustasy derived from the mixed siliciclastic-carbonate stratigraphic record of the northeastern Australian margin, Earth Planet. Sc. Lett., 304, 455–467, https://doi.org/10.1016/j.epsl.2011.02.013, 2011.

Jones, P. W.: A user's guide for SCRIP: A spherical coordinate remapping and interpolation package version 1.4, Technical report, Los Alamos National Laboratory, Los Alamos, NM, 1998.

Jung, G., Prange, M., and Schulz, M.: Influence of topography on tropical African vegetation coverage, Clim. Dynam., 46, 2535–2549, https://doi.org/10.1007/s00382-015-2716-9, 2016.

Kaplan, J. O.: Geophysical Applications of Vegetation Modeling, Ph.D. thesis, Lund University, Lund, 128 pp., 2001.

Kennett, J. P., Keller, G., and Srinivasan, M. S.: Miocene planktonic foraminiferal biogeography and paleoceanographic development of the Indo-Pacific region, in: The Miocene Ocean: Paleoceanography and Biogeography, edited by: Kennett, J. P., Geol. Soc. Am. Mem., 163, 197–236, https://doi.org/10.1130/MEM163-p197, 1985.

Kiehl, J. T., Shields, C. A., Hack, J. J., and Collins, W. D.: The Climate Sensitivity of the Community Climate System Model Version 3 (CCSM3), J. Climate, 19, 2584–2596, https://doi.org/10.1175/JCLI3747.1, 2006.

Knorr, G. and Lohmann, G.: Climate warming during Antarctic ice sheet expansion at the Middle Miocene transition, Nat. Geosci., 7, 376–381, https://doi.org/10.1038/ngeo2119, 2014.

Knorr, G., Butzin, M., Micheels, A., and Lohmann, G.: A warm Miocene climate at low atmospheric CO_2 levels, Geophys. Res. Lett., 38, L20701, https://doi.org/10.1029/2011GL048873, 2011.

Kominz, M. A., Browning, J. V., Miller, K. G., Sugarman, P. J., Mizintseva, S., and Scotese, C. R.: Late Cretaceous to Miocene sea-level estimates from the New Jersey and Delaware coastal plain coreholes: An error analysis, Basin Res., 20, 211–226, https://doi.org/10.1111/j.1365-

2117.2008.00354.x, 2008.

Krapp, M. and Jungclaus, J. H.: The Middle Miocene climate as modelled in an atmosphere–ocean–biosphere model, Clim. Past, 7, 1169–1188, https://doi.org/10.5194/cp-7-1169-2011, 2011.

Kuhnt, W., Holbourn, A., Hall, R., Zuvela, M., and Kaese, R.: Neogene history of the Indonesian Throughflow, in: Continent-Ocean Interactions Within East Asia Marginal Seas, edited by: Clift, P., Kuhnt, W., Wang, P., and Hayes, D., Geoph. Monog. Series, 149, 299–320, https://doi.org/10.1029/149GM16, 2004.

Kürschner, W. M., Kvacek, Z., and Dilcher, D. L.: The impact of Miocene atmospheric carbon dioxide fluctuations on climate and the evolution of terrestrial ecosystems, P. Natl. Acad. Sci. USA, 105, 449–453, https://doi.org/10.1073/pnas.0708588105, 2008.

Langebroek, P. M., Paul, A., and Schulz, M.: Antarctic ice-sheet response to atmospheric CO_2 and insolation in the Middle Miocene, Clim. Past, 5, 633–646, https://doi.org/10.5194/cp-5-633-2009, 2009.

Langebroek, P. M., Paul, A., and Schulz, M.: Simulating the sea level imprint on marine oxygen isotope records during the middle Miocene using an ice sheet-climate model, Paleoceanography, 25, PA4203, https://doi.org/10.1029/2008PA001704, 2010.

Laskar, J., Robutel, P., Joutel, F., Gastineau, M., Correia, A. C. M., and Levrard, B.: A long term numerical solution for the insolation quantities of the Earth, Astron. Astrophys., 428, 261–285, https://doi.org/10.1051/0004-6361:20041335, 2004.

Lear, C. H., Elderfield, H., and Wilson, P. A.: Cenozoic Deep-Sea Temperatures and Global Ice Volumes from Mg/Ca in Benthic Foraminiferal Calcite, Science, 287, 269–272, https://doi.org/10.1126/science.287.5451.269, 2000.

Lear, C. H., Mawbey, E. M., and Rosenthal, Y.: Cenozoic benthic foraminiferal Mg/Ca and Li/Ca records: Toward unlocking temperatures and saturation states, Paleoceanography, 25, PA4125, https://doi.org/10.1029/2009PA001880, 2010.

Le Brocq, A. M., Payne, A. J., and Vieli, A.: An improved Antarctic dataset for high resolution numerical ice sheet models (ALBMAP v1), Earth Syst. Sci. Data, 2, 247–260, https://doi.org/10.5194/essd-2-247-2010, 2010.

Levy, R., Harwood, D., Florindo, F., Sangiorgi, F., Tripati, R., von Eynatten, H., Gasson, E., Kuhn, G., Tripati, A., DeConto, R., Fielding, C., Field, B., Golledge, N., McKay, R., Naish, T., Olney, M., Pollard, D., Schouten, S., Talarico, F., Warny, S., Willmott, V., Acton, G., Panter, K., Paulsen, T., Taviani, M., and SMS Science Team: Antarctic ice sheet sensitivity to atmospheric CO_2 variations in the early to mid-Miocene, P. Natl. Acad. Sci. USA, 113, 3453–3458, https://doi.org/10.1073/pnas.1516030113, 2016.

Lewis, A. R., Marchant, D. R., Ashworth, A. C., Hemming, S. R., and Machlus, M. L.: Major middle Miocene global climate change: Evidence from East Antarctica and the Transantarctic Mountains, GSA Bulletin, 119, 1449–1461, https://doi.org/10.1130/B26134.1, 2007.

Lo, L., Shen, C.-C., Wei, K.-Y., Burr, G. S., Mii, H.-S., Chen, M.-T., Lee, S.-Y., and Tsai, M.-C.: Millennial meridional dynamics of the Indo-Pacific Warm Pool during the last termination, Clim. Past, 10, 2253–2261, https://doi.org/10.5194/cp-10-2253-2014, 2014.

Miller, K. G., Fairbanks, R. G., and Mountain, G. S.: Tertiary oxygen isotope synthesis, sea level history, and continental margin erosion, Paleoceanography, 2, 1–19, https://doi.org/10.1029/PA002i001p00001, 1987.

Montes, C., Cardona, A., McFadden, R., Moron, S. E., Silva, C. A., Restrepo-Moreno, S., Ramirez, D. A., Hoyos, N., Wilson, J., Farris, D., Bayona, G. A., Jaramillo, C. A., Valencia, V., Bryan, J., and Flores, J. A.: Evidence for middle Eocene and younger land emergence in central Panama: Implications for Isthmus closure, GSA Bulletin, 124, 780–799, https://doi.org/10.1130/B30528.1, 2012.

Morley, R. J.: Cretaceous and Tertiary climate change and the past distribution of megathermal rainforests, in: Tropical Rainforest Responses to Climatic Change, edited by: Bush,

M., Flenley, J., and Gosling, W., Springer Praxis Books, Berlin, Heidelberg, 1–34, 2011.

Oerlemans, J.: Correcting the Cenozoic $\delta^{18}O$ deep-sea temperature record for Antarctic ice volume, Palaeogeogr. Palaeocl., 208, 195–205, https://doi.org/10.1016/j.palaeo.2004.03.004, 2004.

Oleson, K. W. and coauthors: Technical Description of the Community Land Model (CLM), NCAR Technical Note NCAR/TN–461+STR, National Center for Atmospheric Research, Boulder, Colorado, 1–174, https://doi.org/10.5065/D6N877R0, 2004.

Otto-Bliesner, B. L., Tomas, R., Brady, E. C., Ammann, C., Kothavala, Z., and Clauzet, G.: Climate sensitivity of moderate and low resolution versions of CCSM3 to preindustrial forcings, J. Climate, 19, 2567–2583, https://doi.org/10.1175/JCLI3754.1, 2006.

Pagani, M., Zachos, J. C., Freeman, K. H., Tipple, B., and Bohaty, S.: Marked Decline in Atmospheric Carbon Dioxide Concentrations During the Paleogene, Science, 309, 600–603, https://doi.org/10.1126/science.1110063, 2005.

Pearson, P. N. and Palmer, M. R.: Atmospheric carbon dioxide concentrations over the past 60 million years, Nature, 406, 695–699, https://doi.org/10.1038/35021000, 2000.

Pollard, D.: A retrospective look at coupled ice sheet–climate modeling, Clim. Change, 100, 173–194, https://doi.org/10.1007/s10584-010-9830-9, 2010.

Pollard, D. and DeConto, R. M.: Description of a hybrid ice sheet-shelf model, and application to Antarctica, Geosci. Model Dev., 5, 1273–1295, https://doi.org/10.5194/gmd-5-1273-2012, 2012.

Pound, M. J., Haywood, A. M., Salzmann, U., and Riding, J. B.: Global vegetation dynamics and latitudinal temperature gradients during the Mid to Late Miocene (15.97–5.33Ma), Earth-Sci. Rev., 112, 1–22, https://doi.org/10.1016/j.earscirev.2012.02.005, 2012.

Ramstein, G., Fluteau, F., Besse, J., and Joussaume, S.: Effect of orogeny, plate motion and land-sea distribution on Eurasian climate change over the past 30 million years, Nature, 386, 788–795, https://doi.org/10.1038/386788a0, 1997.

Retallack, G. J.: Refining a pedogenic-carbonate CO_2 paleobarometer to quantify a middle Miocene greenhouse spike, Palaeogeogr. Palaeocl., 281, 57–65, https://doi.org/10.1016/j.palaeo.2009.07.011, 2009.

Rögl, F.: Mediterranean and Paratethys. Facts and hypotheses of an Oligocene to Miocene paleogeography (short overview), Geol. Carpath., 50, 339–349, 1999.

Rosenbloom, N., Shields, C., Brady, E., Levis, S., and Yeager, S.: Using CCSM3 for Paleoclimate Applications, NCAR Technical Note NCAR/TN–483+STR, National Center for Atmospheric Research, Boulder, Colorado, 1–81, https://doi.org/10.5065/D69S1P09, 2011.

Santodomingo, N., Renema, W., and Johnson, K. G.: Understanding the murky history of the Coral Triangle: Miocene corals and reef habitats in East Kalimantan (Indonesia), Coral Reefs, 35, 765–781, https://doi.org/10.1007/s00338-016-1427-y, 2016.

Schneider, E. K.: A note on the annual cycle of sea surface temperature at the equator, COLA Report 36, 18 pp, 1996.

Shevenell, A. E., Kennett, J. P., and Lea, D. W.: Middle Miocene Southern Ocean Cooling and Antarctic Cryosphere Expansion, Science, 305, 1766–1770, https://doi.org/10.1126/science.1100061, 2004.

Shevenell, A. E., Kennett, J. P., and Lea, D. W.: Middle Miocene ice sheet dynamics, deep-sea temperatures, and carbon cycling: A Southern Ocean perspective, Geochem. Geophy. Geosy., 9, Q02006, https://doi.org/10.1029/2007GC001736, 2008.

Singh, H. K. A., Bitz, C. M., and Frierson, D. M. W.: The global climate response to lowering surface orography of Antarctica and the importance of atmosphere–ocean coupling, J. Climate, 29, 4137–4153, https://doi.org/10.1175/JCLI-D-15-0442.1, 2016.

Smith, R. and Gent, P.: Reference Manual for the Parallel Ocean Program (POP), Ocean Component of the Community Climate System Model (CCSM2.0 and 3.0), Technical Report LAUR-02-2484, Los Alamos National Laboratory, Los Alamos, NM, 2004.

Sprintall, J. and Révelard, A.: The Indonesian throughflow response to Indo–Pacific climate variability, J. Geophys. Res. Oceans, 119, 1161–1175, https://doi.org/10.1002/2013JC009533, 2014.

Sprintall, J., Wijffels, S. E., Molcard, R., and Jaya, I.: Direct estimates of the Indonesian Throughflow entering the Indian Ocean: 2004–2006, Journal of Geophysical Research, 114, C07001, https://doi.org/10.1029/2008JC005257, 2009.

Thiede, J., Jessen, C., Knutz, P., Kuijpers, A., Mikkelsen, N., Nørgaard-Pedersen, N., and Spielhagen, R. F.: Millions of Years of Greenland Ice Sheet History Recorded in Ocean Sediments, Polarforschung, 80, 141–159, 2011.

Tong, J. A., You, Y., Müller, R. D., and Seton, M.: Climate model sensitivity to atmospheric CO_2 concentrations for the middle Miocene, Global Planet. Change, 67, 129–140, https://doi.org/10.1016/j.gloplacha.2009.02.001, 2009.

Tripati, A. K., Roberts, C. D., and Eagle, R. A.: Coupling of CO_2 and Ice Sheet Stability Over Major Climate Transitions of the Last 20 Million Years, Science, 326, 1394–1397, https://doi.org/10.1126/science.1178296, 2009.

Vaughan, D. G., Comiso, J. C., Allison, I., Carrasco, J., Kaser, G., Kwok, R., Mote, P., Murray, T., Paul, F., Ren, J., Rignot, E., Solomina, O., Steffen, K., and Zhang, T.: Observations: Cryosphere, in: Climate Change 2013: The Physical Science Basis, Contribution of Working Group I to the Fifth Assessment Report of the Intergovernmental Panel on Climate Change, edited by: Stocker, T. F., Qin, D., Plattner, G. K., Tignor, M., Allen, S. K., Boschung, J., Nauels, A., Xia, Y., Bex, V., and Midgley, P. M., Cambridge University Press, Cambridge, UK, New York, NY, USA, 317–382, 2013.

von der Heydt, A. and Dijkstra, H. A.: Effect of ocean gateways on the global ocean circulation in the late Oligocene and early Miocene, Paleoceanography, 21, PA1011, https://doi.org/10.1029/2005PA001149, 2006.

Warter, V., Müller, W., Wesselingh, F. P., Todd, J. A., and Renema, W.: Late Miocene

seasonal to subdecadal climate variability in the Indo-west Pacific (East Kalimantan, Indonesia) preserved in giant clams, Palaios, 30, 66–82, https://doi.org/10.2110/palo.2013.061, 2015.

Wolfe, J. A.: Temperature parameters of humid to mesic forests of Eastern Asia and relation to forests of other regions of the Northern Hemisphere and Australasia, U.S. Geological Survey professional paper, 1106, 1–37, 1979.

Wolfe, J. A.: Distribution of major vegetational types during the Tertiary, in: The carbon cycle and atmospheric CO_2: natural variations Archean to present, edited by: Sundquist, E. T. and Broecker, W. S., American Geophysical Union Monograph, 32, 357–375, https://doi.org/10.1029/GM032p0357, 1985.

Wong, E. W. and Minnett, P. J.: The response of the ocean thermal skin layer to variations in incident infrared radiation, Journal of Geophysical Research: Oceans, 123, 2475–2493, https://doi.org/10.1002/2017JC013351, 2018.

Yan, X.-H., Ho, C.-R., Zheng, Q., and Klemas, V.: Temperature and Size Variabilities of the Western Pacific Warm Pool, Science, 258, 1643–1645, https://doi.org/10.1126/science.258.5088.1643, 1992.

You, Y., Huber, M., Müller, R. D., Poulsen, C. J., and Ribbe, J.: Simulation of the middle miocene climate optimum, Geophys. Res. Lett., 36, L04702, https://doi.org/10.1029/2008GL036571, 2009.

Zachos, J., Pagani, M., Sloan, L., Thomas, E., and Billups, K.: Trends, Rhythms, and Aberrations in Global Climate 65 Ma to Present, Science, 292, 686–693, https://doi.org/10.1126/science.1059412, 2001.

Zachos, J. C., Dickens, G. R., and Zeebe, R. E.: An early Cenozoic perspective on greenhouse warming and carbon-cycle dynamics, Nature, 451, 279–283, https://doi.org/10.1038/nature06588, 2008.

Zhang, Y. G., Pagani, M., Liu, Z., Bohaty, S. M., and DeConto, R.: A 40-million-year history

of atmospheric CO_2, Philos. T. Roy. Soc. A, 371, 20130096, https://doi.org/10.1098/rsta.2013.0096, 2013.